Changes and function of the sympathetic nervous system in the skeleton during aging

By

Yuantee Zhu

Dissertation

Submitted to the faculty of the Graduate

School of Vanderbilt University in partial

fulfilment of the requirements for the

degree of

DOCTOR OF PHILOSOPHY

In

Pharmacology

September 30th, 2019

Nashville, Tennessee

Approved by:

Dr. Florent Elefteriou, Ph.D., Mentor

Dr. Carrie Jones, Ph.D.

Dr. Kevin Niswender, M.D., Ph.D.

Dr. Jonathan Schoenecker, M.D., Ph.D.

Dr. Danny Winder, Ph.D.

Dr. Joey Barnett, Ph.D., Chair

Table of Contents

Table of Figures

List of Tables

List of Abbreviations

BMD – Bone mineral density

BMU – Basic multicellular unit (of bone remodeling)

BMSC – Bone marrow stromal cells

βAR – β1 and/or β2 adrenergic receptors (excluding the β3AR)

β2AR – β2 adrenergic receptor, encoded by the *Adrb2* gene

COMT – Catechol-O-methyltransferase, encoded by the *Comt* gene

CNS – Central nervous system

Dbh – Dopamine β-hyroxylase, encoded by the *Dbh* gene

DEXA – Dual energy X-ray absorbitometry

DHPG – Dihydroxyphenylglycol

GnRH – Gonadotrophin-releasing hormone

IML - Intermediolateral nucleus of the spinal cord

Epi – Epinephrine (AKA adrenaline)

ICV – intracerebroventricular

IGF1 – insulin-like growth factor 1

IL-6 – Interleukin 6, encoded by the *Il6* gene

L-DOPA – L-dihydroxyphenylalanine

MAO – monoamine oxidase

NE – Norepinephrine (AKA noradrenaline)

NET – Norepinephrine transporter; AKA SLC6A2, encoded by the *Slc6a2* (*Net*) gene

NPY – neuropeptide Y

OB – osteoblast

Ocy - osteocyte

OCT1/2 – Organic cation transporter 1/2, AKA SLC22A1/2, encoded by the *Slc22a1/2* genes, respectively

OCT3 – Organic cation transporter 3, AKA extraneuronal monoamine transporter/EMT, AKA SLC22A3, encoded by the *Slc22a3* gene

PSNS – Parasympathetic nervous system

RANKL – Receptor activator of NF-κB ligand

VIP – Vasoactive intestinal peptide

VMH – Ventromedial hypothalamus

SNS – Sympathetic nervous system

TH – Tyrosine hydroxylase, encoded by the *Th* gene

Chapter 1. Background and Introduction

The skeleton is a vital organ in vertebrates that facilitates locomotion and protection for soft organs. In higher terrestrial organisms such as mammals, it allows rigid posturing, protects the site of hematopoiesis, and serves as a reservoir for calcium and phosphate homeostasis. Due to these structural roles, the integrity of the skeleton needs to be maintained throughout both life and adaptations to the environment. At its core, this homeostatic structural maintenance is achieved through a process called bone remodeling, which is a balanced action between bone-forming osteoblasts and bone-resorbing osteoclasts. Recent advances in medicine and animal models revealed this organ to also be involved in additional physiological processes, including energy metabolism[1–3], behavior[4–7], reproduction[8,9], and to be the source of hormones[10,11]. As an endocrine organ, the skeleton can also serve as both the target and the source of endocrine and neuronal signals that integrate its functions with other tissues and organs. Furthermore, paracrine interactions exist between bone cells, the skeletal matrix, and cells from other systems within the bone microenvironment. These endo/neuro/paracrine interactions have an impact on the skeleton, as well as other organ systems. In particular, the sympathetic nervous system (SNS), a branch of the peripheral autonomic nervous system, has been demonstrated to be involved in skeletal physiology and pathologies. Briefly, SNS activation releases the neurotransmitter norepinephrine, which acts on osteoblastic β2 adrenergic receptors and leads to bone loss via RANKL-mediated osteoclastogenesis. Osteoblastic β2AR signaling also inhibits pre-osteoblast differentiation into mature osteoblasts[12] (**Fig. 1.1**). However, the understanding of how this neuronal control of bone metabolism occurs is incomplete, and is the focus of this thesis. This introductory chapter will present the background knowledge of skeletal physiology and its known interactions with the SNS, and frame the unknown areas in the field.

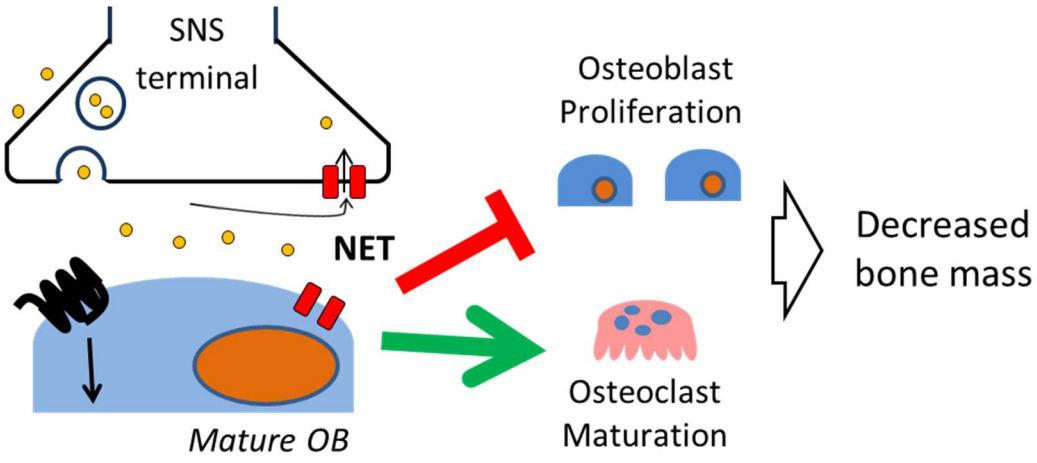

Figure 1.1 – Paradigm of sympathetic nervous system action on bone
Sympathetic nervous system (SNS) activation leads to release of the neurotransmitter norepinephrine (NE), which acts on osteoblastic β2 adrenergic receptors (β2AR), which lead to production of the pro-osteoclastogenic RANKL and inhibits osteoblast proliferation. These effects lead to increase bone resorption and decreased bone formation, resulting on bone loss.

Skeletal physiology and the bone remodeling process

The physiologic bone remodeling process

The skeleton is subject to multiple environmental and physiological stresses, such as mechanical strain or mineral resorption, on a daily basis. Mechanical strain causes microfractures, whether through small sub-fracture external impacts, tension forces caused by muscles, or by passive weight bearing, and are repaired by a dynamic process called bone remodeling. These strains cause microfractures that are sensed by matrix-embedded osteocytes[13], which release the chemokine RANKL into the bone microenvironment in response. This osteocyte-osteoclast coupling in turn stimulates pre-osteoclasts to differentiation mature multinucleated osteoclasts. These bone-resorbing osteoclasts adhere to the bone surface and resorb the bone matrix and mineral around the microfracture. Then, pre-osteoblasts are recruited to the resorption pit, differentiate into bone matrix-forming osteoblasts that deposit Type I

collagen matrix (termed osteoid), and eventually mineralize the freshly made organic matrix with calcium phosphate crystals (hydroxyapatite). Finally, after completing the bone formation function, the post-mitotic osteoblasts either undergo apoptosis, become quiescent bone lining cells, or become embedded inside the bone matrix they secreted to become osteocytes.

The homeostatic balance between bone formation and resorption preserves the structural integrity of bone and maintains bone mass. At a steady state, there are multiple sites in the body that are simultaneously undergoing this process, and it is believed the adult human skeleton replaces itself every 10 years[14]. The complex process of bone remodeling is integral for skeletal homeostasis and integrity. In addition to the paracrine signals between osteoblast and osteoclasts, other systemic endocrine and neuronal factors also influence this homeostatic balance. However, unlike other functions under central homeostatic control such as heart rate, fat mass, or mineral balance, a central integrator of afferent and efferent signals to regulate bone mass has not been identified. Although, extensive evidence exists of the central nervous system exerting control of bone mass, and will be covered in further detail below. Finally, perturbations to bone metabolism may tip the formation-resorption balance in favor towards one direction, and result in bone metabolic diseases.

Osteoporosis, a disease in bone fragility

Osteoporosis is a bone metabolic disease of skeletal fragility that affects an estimated 10 million Americans[15]. Its prevalence is highest in the aged population, affecting 25% of people over the age of 50[15], and an estimated half of all post-menopausal women[16,17]. It is a silent disease without any associated pain or other symptoms until a pathological fracture occurs. These fractures present with their own morbidity and mortality, with a 5-year mortality rate of a hip fracture being 20%[18]. The wide prevalence of osteoporosis combined with the consequences of an osteoporotic fracture make both the treatment and prevention of osteoporosis a national health issue.

The etiology of the disease is either decreased bone mineral density (BMD), impaired bone microarchitecture, or both. In the general population, accumulation of bone mass throughout development and puberty leads to peak bone mass, which is occurs between 25-30 years of age[16], and steadily declines throughout age. The determinants of peak bone mass are largely genetic, although factor such as diet, physical activity, and medication during childhood and adolescence may impact this value[19]. The peak bone density achieved in young adulthood represents a reserve of bone mass that is protective of the gradual bone loss through life. Conversely, many factors can increase the rate of bone loss: diseases of other organs such as malabsorption, renal dysfunction, COPD, chronic rheumatologic diseases, and malignancy[11,17,20]; iatrogenic such as chronic glucocorticoid use; or skeletal unloading such as prolonged bedrest or space flight[21]. Therefore, screening of at-risk populations for low bone mass is an important part of osteoporosis management.

Osteoporosis, or the less severe osteopenia, can be diagnosed based on measurements of bone mass via dual energy X-ray absorbitometry (DEXA) scans, or by evidence of pathological fractures not attributable to high-energy trauma[18,22]. The former is a quantitative measurement of bone density, and compares it to the patient population, with 2.5 standard deviations below the population mean being sufficient for a diagnosis for osteoporosis. On the other hand, a patient presenting with a pathologic fracture that would not otherwise occur in individuals with healthy skeletal structure such as at the distal wrist or femoral head, or vertebral compressions are diagnostic of osteoporosis[18]. It is thus important to identify at-risk individuals, reduce or treat other factors that increase bone loss, and treat osteoporosis before the decreased bone mass leads to a pathologic fracture.

The treatments of osteoporosis aim to prevent further bone loss through a multi-faceted approach. Adequate mineral balance can be targeted through vitamin D and calcium supplementation[17]; maintaining bone density and quality can be achieved through weight-bearing exercise; underlying pathologies can be directly treated, such as selective estrogen receptor modulators for post-menopausal

estrogen deficiency[23]; and the bone remodeling process can be directly targeted pharmacologically. There are two major drug groups on the market were designed to specifically affect bone remodeling: anti-resorptives and bone anabolic drugs, both defined by their function. Anti-resorptives target osteoclasts but achieve this through several mechanisms: preventing RANKL-mediated osteoclastogenesis with the biologic drugs like denosumab[24], inhibiting osteoclast function with the bisphosphonate drug class, or inhibiting the bone-catabolizing osteoclast protease Cathepsin K with Odanacatib[25]. On the other hand, bone anabolic agents aim to promote osteoblastic bone formation by direct stimulation of osteoblast differentiation with Teriparatide[26], or blocking the osteoblasts inhibitor sclerostin via biologic drugs such as romosozumab[27,28]. However, these drugs have significant side effects that limit their efficacy, necessitating the development of new drugs to treat osteoporosis.

Differences in human versus murine bone physiology

Mice have been used for decades as a model organism for bone biology. However, the bone remodeling process differs between human and animals in the gross anatomy of the skeleton, the microanatomy of bone tissues, the rate of bone metabolism, and the microarchitecture of bone remodeling process.

On the gross anatomical scale, the difference in posture between humans and mice leads to different loading of bones in these two species. This is most significant in the vertebrae, which are subject to compressive forces in humans. On the microscopic scale, mice bone architecture differs greatly from humans. A microscopic bone structure called osteons around a central Haversian canal, which are intracortical vessels that permeate the bone, are present in larger animals but do not exist in mice[8,29,30]. These osteons are form during the bone remodeling process, where osteoclasts resorb existing osteons in bone, and osteoblasts form new concentric circular osteons in the resorption pit. This vessel system provides nutrition to the organ beyond the capacity of simple diffusion, and is also an

ultrastructure of bone integrity based on oblique osteons[31]. Bone resorption is also different in humans compared to mice. In mice, the bone remodeling process involving osteoblasts and osteoclasts occurs in an open bone microenvironment. However, human bone remodeling occurs within a microscopic structure called the basic multicellular unit (BMU), which represents the foci of bone remodeling. Once the bone remodeling process is initiated by osteocytes in higher mammals such as humans, bone lining cells - inert cells from the osteoblast lineage – expand to form a canopy that merges with blood vessels. This canopy isolates the focal bone resorption and formation to the local area[32], and prevents paracrine pro-osteoclastogenic factors from diffusing away to cause ectopic bone remodeling.

The basal metabolic rate in mice is much higher than humans. This is evident in basal energy expenditure, heart rate, and also extends to skeletal homeostasis. Bone turnover in mice is much higher than that in humans, and conditions that elicit changes in bone mass are more rapidly evident in murine models than human patients[29,33]. Finally, the commonly used C57BL6 mouse strain has among the lowest natural bone mass of among laboratory mice[34,35], which decreases the sensitivity of this strain to bone loss. However, the ubiquity of this strain in genetic and pharmacologic studies necessitates its continued use in order to properly compare results with previous findings. Taken together, these multiple differences between murine and human physiology makes translating animal model findings to human physiology non-trivial, and necessitates independent confirmation of many studies in humans.

Bone formation in other bone physiologies

Two additional processes exist where bone remodeling is involved, although with slight variation: bone growth during development until the end of puberty, and fracture healing. A full background of physiologic mechanisms and pathologies that influence either bone growth or fracture healing are beyond the scope of this thesis. However, a brief overview of the process is provided. Bone growth can be further subdivided into growth of long bones via a growth plate through a process called

endochondral ossification, and of flat bones via direct conversion of cartilage via a process called intramembranous ossification. However, it should be mentioned that fracture healing approximately recapitulates some of the processes seen though bone development[36,37].

Endochondral ossification involves chondrocytes (the resident cells of cartilage) from the resting zone of the epiphyseal growth plate undergoing proliferative and hypertrophic differentiation changes, and depositing hyaline cartilage matrix comprised of hydrated proteoglycans. These hypertrophic chondrocytes create a widening hypertrophic zone within the epiphyseal cartilage, which becomes the basis of the primary ossification center. This epiphyseal widening is the ultimate source of the lengthening of the long bones, as well as vertebrae. The end distal end of the growth plate, the cartilage matrix is calcified, and hypertrophic chondrocyte death leads to recruitment of osteoblast and osteoclasts, which resorb and replace the calcified cartilage with calcified bone. This process of osteoblast/clast restructuring of cartilage is termed bone modeling, and is distinct from the bone remodeling process occurring exclusively in bone. Depletion of the reservoir of resting chondrocytes throughout bone growth leads to the disappearance of the cartilaginous growth plate – commonly termed “closing” of the growth plate observed at the end of puberty – and defines the end of endochondral ossification and the lengthening of long bones[38,39]. During fracture callus healing, a hematoma forms from traumatic tissue damage, which triggers the inflammation cascade. Afterwards, stem cells from the adjacent tissues migrate into the hematoma, and differentiate into chondrocytes to form the cartilaginous soft callus. Afterwards, endochondral ossification occurs where osteoblasts/osteoclasts replace the hyaline cartilage with bone tissues[37].

Intramembranous ossification occurs in flat bones such as those of the cranium and mandible, and involves the deposition of bone matrix by osteoblasts without cartilage. Developmentally, ossification centers form at the location of future bones, and act as the nidus of bone apposition. Osteoblasts then deposit immature organic osteoid and mineralize the matrix. Embedded osteoblasts

become osteocytes, and a population of mesenchymal stem cells remain on the surface to form the periosteum, and can differentiate into osteoblasts for continued intramembranous bone growth[38]. This process is also responsible for appositional growth of the bone diaphysis midshaft, where periosteum directly deposits bone on the outside of the cortex, thereby increasing the width of the bone without the need for a cartilage scaffold.

Bone cell physiology and function

There are three major bone cells involved in skeletal physiology, specifically with regards to bone remodeling: bone forming osteoblasts, bone resorbing osteoclasts, and bone residing osteocytes. The term *osteoblast* is used as describing cells of the bone-forming lineage of mesenchymal stem cells. The terminology used in this thesis will be precise to avoid confusion:

- Osteoblasts refer specifically to bone-surface cells that deposit and mineralize Type I collagen organic matrix and mineralized.
- Osteocytes refer specifically to *in vivo* matrix-embedded terminally differentiated osteoblasts.
- Bone marrow stromal cells (BMSCs) are *in vitro* multipotent cells isolated from the bone marrow defined by their adherence to tissue culture plastic (see Materials and Methods), and are able to differentiate into osteoblast-like cells.

Terms referring to *in vitro* osteoblast cultures in this thesis are descriptive, e.g. osteoblastic/osteocytic, osteoblast/osteocyte-like, or osteoblast-lineage. While properties and markers of differentiated BMSCs, primary osteoblasts (e.g. calvarial osteoblasts), or osteoblastic cell lines are consistent with the known *in vivo* biology, many differences still exist. Furthermore, isolated *in vitro* cell populations are not in the multi-cell lineage bone microenvironment that exists in the whole organ. Thus, extrapolating *in vitro* findings to be equal to *in vivo* may not be appropriate.

Osteoclasts in bone metabolism

Osteoclasts are bone resorbing cells derived from the macrophage-monocyte lineage. Similar to macrophages that "clean up" their resident tissue of debris, osteoclasts "clean up" damaged tissue (micro-fractured bone) in the bone microenvironment.

The differentiation pathway of osteoclasts starts with macrophage-monocyte precursors, which differentiated into monocytes, then pre-osteoclasts. The cells are in circulation, and are drawn to a site of needed resorption by the chemokine RANKL and MCSF, which also trigger the differentiation and fusion of mononucleated osteoclasts to the functional multinucleated cell. The mature osteoclast basolateral surface attaches onto the underlying bon surface via integrins, forms a ruffled border that isolates the resorption area - termed sealing zone. These cells then acidify the sealing zone, and enzymes such as Cathepsin K and matrix metalloproteases are secreted to degrade the bone mineral and matrix[32]. The physiologic needs for osteoclast bone resorption are multiple. They are necessary to maintain skeletal integrity by absorbing bone microfractures, allowing proper repair through bone remodeling. Although bone resorption leads to bone loss, loss of osteoclast function may paradoxically *lead* to skeletal fragility via decreased bone quality[16,40], highlighting the need for bone remodeling to maintain skeletal integrity. This paradoxical mechanism is partially due to osteoclast-osteoblast coupling (which is distinct and opposite from the classic RANKL-mediated osteoblast-osteoclast coupling), in which osteoclasts influence osteoblasts through by either liberating matrix-embedded growth factors or secreting their own pro-osteoblastic molecules[41]. Furthermore, bone resorption also liberates calcium for mineral homeostasis – a process triggered by osteoblasts/osteocytes but ultimately mediated by osteoclasts. However, in the context of bone loss and prevention of osteoporosis, preventing excess bone resorption by osteoclasts is still a priority.

Osteoblast lineage differentiation and development

Osteoblasts arise from the mesenchymal lineage. Mesenchymal stem cells (MSCs) are multipotent cells defined by their multipotent ability to differentiate into the osteoblast, chondrocyte, adipocyte, myocyte, but not hematopoietic lineages[42]. In many tissues, resident MSCs called stromal cells are present in the tissue, and are capable of proliferating and differentiating into connective tissue cells in response to injury for tissue repair (e.g. bone remodeling or fracture repair). Mesenchymal stem cells begin differentiation into osteochondral progenitors under the control of the "master switch" Runx2[43], and are committed to the osteoblastic linage after expression of the transcription factor *Osx* in pre-osteoblasts[44,45]. These cells are capable of proliferation and differentiation into fully functional osteoblasts, which express the genes *Col1a1* and *Bsp* encoding structural proteins Type I collagen and bone sialoprotein, respectively. These early osteoblasts also express *Alp*, which encodes alkaline phosphatase responsible for bone matrix mineralization, and are capable of further proliferation. Later during differentiation, these cells express the mature osteoblast marker *Ocn* encoding the bone matrix protein osteocalcin[46]. Finally, these post-mitotic mature osteoblasts are subject to three fates: undergo apoptosis, become quiescent bone lining cells on bone surfaces, or remain embedded within the bone matrix as osteocytes. In the terminally differentiated osteocytes, expression of the osteocytic marker sclerostin encoded by the *Sost* gene acts to inhibit osteoblast differentiation[47,48] – thereby influencing both arms of the bone remodeling process.

Both perivascular smooth muscle cells[42,49] and periosteal cells [50]are capable of being the source of new osteoblasts. It is likely that both cell types are responsible for differentiating into the bone forming cells, but in response to different stimuli and at different locations. Perivascular smooth muscle cells – AKA pericytes – can by characterized by several markers such as smooth muscle actin (α-SMA), platelet-derived growth factor receptor β (PDGFRβ), annexin A5 (Anxa5), neural/glial antigen 2 (NG2), or the homeodomain transcription factor Msx1. None of these markers are defining for all MSC

populations, and none are restricted to purely MSCs (e.g. NG2 is also a glial marker)[42]. Thus, these pericytes are defined by their location, marker expression, and function. It is believed that experimentally isolated BMSCs used to study osteoblast differentiation are pericytes, and stromal stem cells isolated from other tissues (i.e. muscle[51,52] and adipose[53]) are also pericytes. In addition to being the source of MSCs in the bone marrow, pericytes have also been demonstrated to control the perivascular niche by facilitating interactions between the endothelium and hematopoietic cells[54,55]. This function is particularly important for the bone marrow, where hematopoietic cell egress is critical for immune function as well as autoimmune diseases[56–58].

The periosteum is another source of osteo/chondrogenic cells, although they do not possess the multipotent potential to differentiate into adipocytes or myocytes. The periosteum is the outer membrane surrounding bones. It is a highly vascularized structure, is densely innervated by sensory neurons, and serves as the site of attachment of tendons[59]. The periosteum is comprised of two layers – the thick fibrous outer layer and an inner cambium layer capable of osteogenesis[50], and its located offers clues into its function. It is capable of forming bone through appositional growth, as cambial cells can differentiation into osteoblasts. It is also critical for providing chondrocyte and osteoblast progenitors during fracture healing[50]. However, during normal bone homeostasis the periosteal side of the cortex is not actively undergoing bone remodeling, unlike in trabecular woven bone surfaces in the medullary cavity. Thus, it is believed that the periosteum contributes little to the pathogenesis of osteoporosis.

Embryologically, the osteoblast lineage arises from the mesoderm. The axial skeleton develops from parallel segmented structures called somites formed on both sides of the neural tube along the dorsal part of the developing embryo. These structures give rise to the axial skeleton, including the vertebrae, ribs, and the occipital bone. The appendicular long bones are formed from the mesenchymal condensation, which are pre-cartilage mesenchymal cells that form in the limb bud. These cells form the cartilage matrix of the primitive long bone, give rise to the growth plate, and are replaced by bony

tissues via the process of endochondral ossification. The exception to the mesodermal origin of bone are the pharyngeal arches, which arise from neural crest cells of the neuroectoderm give rise to facial (maxillary) and jaw (mandibular) bones.

Osteocyte signaling and function in bone remodeling

Osteocytes were previously thought to be quiescent cells that held little to no role in bone physiology. However, the past decade of advances has shown the osteocyte to be the central cell in regulation bone metabolism[13,60,61]. These cells are terminally differentiated post-mitotic osteoblasts that become embedded in lacunae in compact and cancellous bone. Through this transition, cuboidal osteoblasts become polygonal osteocytes with a large reduction of cytoplasmic volume and organelles (due to the decreased synthesis requirements) within bone lacunae, and with many dendritic processes. The long dendrite-like processes that extend throughout the bone, connecting them with other osteocytes and to cells in the surface microenvironment, facilitating both a sensory and an instructive signaling role in bone. As previously mentioned, osteocytes sense microfractures in the bone stroma and release the pro-osteoclastogenic chemokine RANKL[13], which then initiates the bone remodeling process. They also express and release the anti-osteoblastic protein sclerostin, which inhibits the Wnt pathway in osteoblasts and leads to overall decreased bone formation[47]. In addition to their now-classical role as the regulator for bone remodeling, osteocytes are also capable of mechanosensation. They sense mechanical stress on the skeleton and produce extracellular signaling molecules such as bone morphogenic proteins (BMPs), nitric oxide, or prostaglandin E2 (PGE2), which can also lead to bone remodeling[11,61]. Unlike transient osteoblasts and osteoclasts, the osteocytes are the resident cells of skeletal matrix, comprise 90% of the cellularity of the tissue[61].

In addition to their central role in bone remodeling, osteocytes also play dynamic roles in mineral homeostasis. They express and secrete FGF23, which acts on kidneys to increase phosphate

urinary elimination and alter vitamin D metabolism[62,63], and can be modulated according to the body's mineral needs. They also modulate systemic calcium concentrations, which are important for proper homeostasis and very sensitive to perturbations. Parathyroid hormone (PTH), which can act on the kidney to retain calcium from excretion, also acts on osteocytes to acutely replenish systemic calcium through stimulation osteoclast-mediated resorption[64]. Additionally, lactation and nursing present a large drain in maternal calcium, and maternal calcium homeostasis is partially mediated by osteocyte PTH/PTHrP hormonal signaling[60,65]. Finally, there is also evidence suggesting osteocytes directly resorb peri-lacunar bone[66].

Osteocytes are not only capable of signaling to osteoblasts and osteoclasts in the bone marrow, but are also capable of communication between each other via their dendritic processes. Membrane protein complexes called gap junctions are expressed in osteocytes[67], and are able to diffuse dye to adjacent cells. Gap junctions connect the cytoplasm of adjacent cells, and allow the transmission of cytoplasmic contents such as secondary messenger molecules or electric signals between these cells[68–70]. Deletion of the gene encoding the gap junction protein Connexin 43 (*Gja1*) in the osteoblast lineage in mice leads to a limited bone remodeling response to mechanical loading[69,71], suggesting that connexin-mediated inter-osteocytic communication is important for proper bone homeostasis.

Given the multiple known roles that osteocytes in have in mineral homeostasis and bone remodeling, these would be the appropriate cell in the bone microenvironment to regulate other skeletal homeostatic processes.

Osteoblasts and osteocytes as endocrine cells

In the previous section, osteoblasts have been presented as the bone matrix forming and mineralizing cell in the bone microenvironment; as the "bone formation end-point" of bone homeostasis. However, recent advances in bone biology also identify osteoblast lineage cells as the

source of endocrine signals. As mentioned before, osteocytes synthesize and secrete FGF23 into circulation, which acts as a systemic modulator of phosphate and vitamin D levels[63]. Osteoblast-lineage cells also secrete osteocalcin (Ocn), which was classically believed to be a bone stromal protein, though its role in skeletal homeostasis was not well understood. Genetic deletion of the osteocalcin gene had little effect on bone mass, but surprisingly had deficient glucose homeostasis metabolic syndrome-like phenotype, and decreased male fertility via decrease testosterone[8,72,73].

There is significant cross-talk between osteoblasts and other connective tissues as well. It is classically known that muscles influence bone by exerting mechanical strain, and unloading simply from disuse leads to both muscle wasting and bone loss. However, myocytes also produce and secrete muscle-specific chemokines termed "myokines," including IGF-1, IL-6 and LIF/SDF1[74], that are capable of acting on osteoblasts and may be endocrine mediators of bone loss during conditions such as bedrest. Furthermore, osteoblasts also produce pro-angiogenic factors such as VEGF that influence angiogenesis *in vivo*. While the osteoblast-endothelial interactions are largely restricted to the bone marrow, these findings further the concept that osteoblasts and osteocytes serve functions beyond bone remodeling.

Overview: Sympathetic nervous system physiology

The autonomic nervous system is a branch of the efferent peripheral nervous system comprised of the sympathetic (SNS) and the parasympathetic nervous systems (PSNS). These two divisions control unconscious bodily functions, are intricately involved in body homeostatic systems involving the brain, and are distinct from the somatic nervous system involved in "conscious" sensation and motor control. In general, the SNS is involved in "fight or flight" responses such as increased blood flow to muscles, increased cardiac output, pupil dilation; while the PSNS is involved in "rest and digest" or "feed and breed" responses such as salivation, digestion, and sexual arousal. While these two branches are

roughly considered to act in opposition to each other, their functions in multiple organ systems is understandably more complex.

Anatomical structure of the sympathetic nervous system

The sympathetic nervous system acts on almost all major organ systems. The cell bodies of SNS nerves are located in the paraspinal sympathetic ganglia, which span the entire length of the vertebral column. The sympathetic pre-ganglionic nerves travel superiorly and inferiorly between ganglia, making each individual ganglion redundant. The origin of central SNS pre-ganglionic innervation is via the spinal nerves, and arises from autonomic motor neuron cell bodies in the intermediolateral nucleus (IML) of the spine, located along the length of the lateral thoracic spinal cord (T1-L2). All pre-ganglionic fibers are cholinergic, and release the neurotransmitter acetylcholine to activate nicotinic acetylcholine receptor situated on ganglionic sympathetic cell bodies. These post-ganglionic afferent sympathetic fibers from these cells are mostly noradrenergic (releasing norepinephrine, NE) unmyelinated Type C nerve fibers, and course and synapse close to the target organ of action. The only two exceptions to this peripheral nerve organization are the adrenal glands, in which the pre-ganglionic cholinergic fibers synapse directly onto the neuroendocrine adrenal medullary cells to release epinephrine (Epi); and eccrine thermoregulatory sweat glands, in which post-ganglionic fibers are cholinergic[75,76].

Physiologic catecholamine synthesis and release

Both Epi and NE belong to the biogenic amine molecule class called catecholamines, which also includes the CNS neurotransmitter dopamine. Catecholamines are synthesized by catecholaminergic neurons from the amino acid L-tyrosine by the cytoplasmic enzyme tyrosine hydroxylase, which produces the precursor molecule L-dihydroxyphenylalanine (L-DOPA). The enzyme Aromatic L-amino

acid decarboxylase then converts L-DOPA to dopamine. Cytoplasmic dopamine is pumped into vesicles via vesicular monoamine transporters (VMATs), it is converted to NE by the enzyme Dopamine β-hydroxylase (Dbh), and remains in synaptic vesicles until release. Finally, vesicular NE can be converted to Epi in the adrenal medulla by Phenylethanolamine N-methyltransferase[76]. The hydroxylation of tyrosine to L-DOPA is the rate-limiting step of catecholamine biosynthesis[77], and the expression of TH is commonly used as a marker for catecholaminergic neurons such as those in the SNS[76].

The release of NE and Epi is tightly controlled at both the neuron level and SNS terminal level. Upon activation of sympathetic neurons by pre-ganglionic neurons, a generated action potential propagates to the SNS nerve terminals, which leads to depolarization of the nerve terminal membrane. This causes Ca^{2+} influx via the voltage-gated N-type calcium channel, which activates synaptic fusion molecules syntaxin, synaptobrevin, and SNAP-25 to cause vesicle fusion with the plasma membrane and release of neurotransmitters via diffusion. In sympathetic neuron terminals located close to the target tissue, NE diffuses out of the vesicles into the extracellular space, and binds onto adrenergic receptors to mediate target cell action[76].

Adrenergic receptor pharmacology

NE, Epi, and other adrenergic ligands act on adrenergic receptors to elicit their function. The receptor subclasses (β, α1, and α2) were historically initially named based on their secondary messengers: stimulating cyclic AMP (cAMP), phospholipase C (PLC), or inhibiting cAMP, respectively. These receptors are Class A rhodopsin-like seven transmembrane G-protein coupled receptors that act via heterotrimeric G-proteins. Receptor activation triggers the receptors to facilitate an exchange of Gα-bound GDP for GTP, thereby activating the Gα-subunit, causing it to dissociate from the Gβγ complex trigger. The membrane-bound G-protein subunits then act on downstream effector proteins such as Gαs activating or Gαi inhibiting adenylate cyclase, or Gαq activating phospholipase C (PLC), leading to the

production of secondary messenger molecules cAMP, IP_3, or DAG. These intracellular molecules then diffuse through the cytoplasm or along the plasma membrane onto effector molecules, and elicit a wide variety of cellular responses. After activation, the adrenergic receptors can be deactivated through ligand dissociation, or by receptor phosphorylation leading to receptor deactivation[76]. The physiologic consequence of ligand binding depends on the receptor and cell type, and a general overview of all adrenergic receptors and their signaling is given below (**Table 1.1**), however many details on adrenergic receptor signaling exists that are beyond the scope of this thesis.

Table 1.1 Adrenergic receptors signaling

Receptor	Gene	G-protein coupling; 2° messenger
β1-AR	*Adrb1*	Gαs; AC→cAMP→PKA
β2-AR	*Adrb2*	Gαs; AC→cAMP→PKA
β3-AR	*Adrb3*	Gαs; AC→cAMP→PKA
α1a-AR	*Adra1a*	Gαq; PLC→IP3+DAG
α1b-AR	*Adra1b*	Gαq; PLC→IP3+DAG
α1d-AR	*Adra1d*	Gαq; PLC→IP3+DAG
α2a-AR	*Adra2a*	Gαi/o; ↓cAMP
α2b-AR	*Adra2b*	Gαi/o; ↓cAMP
α2c-AR	*Adra2c*	Gαi/o; ↓cAMP

Catecholamine metabolism

After catecholamines are released into the extracellular environment to elicit their function on target cells, signaling is terminated by reducing the extracellular ligand concentration either by passive diffusion of the ligand away from the target cell, active uptake of the ligand out of the extracellular environment, or pre-synaptic auto-receptors terminating vesicular ligand release. Diffusion of the neurotransmitter out away from the site of action decreases the concentration of the ligand on the tissue, and allows it to enter circulation to be cleared by either renal or hepatic elimination. Active uptake by transmembrane pumps located on either the neuron or target tissues can rapidly eliminate neurotransmitter from the extracellular environment[78]. Finally, pre-synaptic auto-receptors, such as the

α2c-AR, can bind NE and cause the sympathetic nerve terminal to stop the additional release of neurotransmitter. It is likely a combination of these three mechanisms, along with adrenergic receptor deactivation on target cells, contribute to the termination of adrenergic signaling.

Active uptake is a dynamic process that can occur via either low- or high-affinity mechanisms. The organic cation transporters (OCTs) are of the solute carrier 22A (SLC22A) class of transmembrane proteins. OCT1, OCT2, and OCT3 are capable of transporting organic cations including catecholamines from extracellular to intracellular compartments. These OCTs are expressed in many tissues, are promiscuous to multiple targets, and also maintain the blood-brain barrier by unidirectionally transporter out drugs and endogenous molecules from the brain. However, their low affinity and specificity for catecholamines implies both slower mass clearance of neurotransmitter from tissues, but their more ubiquitous expression leads to a higher clearance capacity[79,80].

A high-affinity mechanism of NE/Epi clearance exists via the norepinephrine transporter (NET, AKA SLC6A2), a transmembrane pump that is capable of transporting even low concentrations of NE, Epi, and dopamine out of the extracellular environment. This transporter is of the SLC6A Na^+/monoamine antiporter family, which includes biogenic amine transporters such as the dopamine, serotonin, and GABA transporters[81,82]. dependent on extracellular Na^+ concentrations, is reversed by cocaine/amphetamines, and selectively blocked by reboxetine and desipramine. Due to its tissue-limited tissue expression, its overall tissue transport capacity is limited. Expression of NET was classically understood to be limited to adrenergic neuron terminals[76]. However, studies from the Elefteriou lab has found NET to surprisingly also be expressed and functional on osteoblasts, with a possible role for NET in bone physiology[83].

Once catecholamines are transported into the intracellular environment, they are subject to four possible fates: continued transporter through the basolateral membrane into the circulation or urine, repackaging, metabolism by methylation, or metabolism by mitochondrial oxidation. Continued

basolateral membrane transport is a common mechanism in cells of the blood-brain barrier and renal glomerulus, and facilitates clearance from sensitive compartments[76]. As a matter of fact, NE spillover is often detected in both circulation and in the urine. In cells naturally capable of releasing catecholamines such as sympathetic nerve terminals, vesicular uptake via VMATs can repackage these molecules for future re-release, and lessen the synthetic burden of these neuronal cells for continuous neurotransmitter synthesis. Finally, NE or Epi can be metabolized by the catabolic enzymes Catechol-O-methyltransferase (COMT) or monoamine oxidases (MAOs). COMT is primarily expressed in the liver, although brain expression is limited to several regions[84,85]. It functions to methylate the catecholamines into metanephrines, which both invalidates their biochemical function as well as improve their solubility for excretion. Monoamine oxidase are mitochondrial proteins that exists in two isoforms, MAO-A and MAO-B, which are expressed differentially across the CAN and peripheral non-neuronal tissues[86,87]. They function to deaminate biogenic amine molecules such as NE and Epi via oxidation into aldehyde intermediates, which are further reduced via aldehyde reductase into metabolites such as dihydroxyphenylglycol (DHPG)[76].

Impact of sympathetic nervous system on bone

Multiple experiments in mice and humans suggest that the sympathetic nervous system regulates skeletal homeostasis[6,88,89]. Sympathetic nerve fibers indeed were shown to innervate skeletal tissues[90–93], and osteoblasts express receptors for norepinephrine (NE), the neurotransmitter released by these sympathetic nerves, with the β2-adrenergic receptor (β2AR) being the predominant receptor expressed in this lineage[88]. The current model of how peripheral sympathetic nerves impact bone remodeling includes the release of NE, which acts on osteoblastic β2AR to activate PKA to phosphorylate the transcription factor ATF4[89], which promotes *Rankl* expression and RANKL-mediated activation of osteoclasts[88,89]. Furthermore, β2AR stimulation has also been shown to directly inhibit osteoblast

proliferation via cyclin D1 and *Clock* genes[89,94–98]. This model is derived from genetic mouse models as well as pharmacological approaches targeting mainly post-synaptic βARs. Few studies exist that address pre-junctional sympathetic nerves, although one study of mice lacking *Foxo1* in *Dbh*-positive pre-synaptic noradrenergic neurons have low sympathetic outflow coinciding with high bone mass, supporting the role of endogenous NE in controlling bone remodeling[99]. However, there are multiple other adrenergic receptors, neurotransmitters, and CNS mechanisms implicated in this model that complicate the understanding of the mechanisms of SNS action on bone.

Hypothalamic control of bone metabolism

The study of central hypothalamic control of bone metabolism arose from studies of the *ob/ob* and *db/db* mice[12,88,100,101]. These mice were originally studied because of their hyperphagic obese phenotype, and were discovered to be deficient in the genes encoding leptin and the leptin receptor, respectively. Leptin is an adipose-derived hormone that serves as a signal to the CNS of energy status (e.g. fat stores). Low leptin in *ob/ob* mice, or inability to sense leptin via an absent receptor in *db/db* mice, led to an aberrant signal to the hypothalamus that the body energy homeostasis was low, and resulted in increased feeding. Surprisingly, these animals were also found to have high bone mass despite have gonadal dysfunction[12,101]. Confirmation of the central mechanism of leptin on bone mass was confirmed via direct intracerebroventricular (ICV) delivery of leptin to the third ventricle of the brain in leptin-deficient mice, which corrected the high bone mass phenotype[101].

While the hypothalamic control of bone physiology was demonstrated, the afferent mechanism was still uncertain. Parabiosis experiments joining the peripheral circulation of two *ob/ob* animals – one treated with ICV leptin – demonstrated the downstream mediator of leptin causing bone loss was not hormonal. Furthermore, overexpression of the hormone in bone did not correct the high bone mass from global leptin deficiency - confirming that leptin's effect was not peripheral[12,88]. Rather, it was

known that leptin mediates increased peripheral energy expenditure via the SNS, and that *ob/ob* mice had decreased sympathetic outflow[100102]. Indeed, global genetic deletion of *Dbh*, a key enzyme in catecholamine synthesis, corrected the high bone mass in *ob/ob* mice, suggesting that leptin-mediated bone loss occurs via the sympathetic nervous system[12,88]. Further studies showed that leptin acts via its receptor on brainstem serotoninergic neurons, and that serotonin pathways into the ventromedial nucleus of the hypothalamus (VMH) was responsible for leptin's actions. Deletion of the brain-specific serotonin synthesis enzyme tryptophan hydroxylase 2 (*Tph2*$^{-/-}$) produced mice that had low bone mass, high basal metabolic rate, and high SNS outflow[103], phenocopying the bone and sympathetic phenotype of the o*b/ob* mice. More recent studies have supported this serotonin-mediated mechanism by demonstrating that serotonin reuptake inhibitors cause bone loss in mice via the SNS[104]. Interestingly, in *ob/ob* and *db/db* mice with deficient leptin signaling, bone loss was observed in the appendicular long bones, but not the axial vertebrae[105,106]. Meanwhile, the *Tph2*$^{-/-}$ mice had low bone mass in all bones[103]. The leptin-deficient mice also had increased marrow adiposity, which is a well-documented phenotype of energy homeostasis imbalance[100]. It is possible that the additional unknown mechanisms such as the possible action of leptin on mesenchymal stem cells[106] may account for this differential phenotype between the axial and appendicular skeleton.

Pituitary hormones, under the control of the hypothalamus, are also known to influence bone mass in pathways independent of the SNS. Hypothalamic gonadotrophin-releasing hormone (GnRH), which influences luteinizing hormone (LH) and follicular stimulating hormone (FSH), can also alter levels of testosterone or ovarian hormones like estrogen [19], which can in turn influence bone mass. Two hypothalamic hormones involved in lactation, have direct effects on bone turnover. Prolactin is shown to promote bone loss in rats independent of gonadal function[107]. Meanwhile, oxytocin has a direct dual mechanism of an anabolic effect on osteoblasts, and inhibitory effect on osteoclasts[108,109]. Finally, there is also evidence of the orexin/hypocretin system, which controls wakefulness, appetite, and reward, also

controls bone metabolism[110]. The orexin 1 receptor (OX1R) and its ligand orexin was found to be expressed in MSCs, osteoblasts, and adipocytes in mouse tibiae; whereas orexin, OX1R, and the Orexin 2 receptor (OX2R) were expressed in the brain. Deletion of OX1R results in bone gain, while deletion of OX2R and both receptors leads to bone loss. The authors of the study concluded that the orexin system and its receptors elicit opposite roles in the central versus periphery, with a dominant central hypothalamic mechanism promoting bone mass gain.

Taken together, there are many mechanisms through which the hypothalamus can control bone metabolism. These findings all further the understanding that bone does not purely serve as structural function, but is also an endocrine organ.

Adrenergic receptors in bone biology

The central mechanism of SNS action on bone via the β2AR on osteoblasts. Chronic stimulation of βARs with the non-selective agonist isoproterenol (ISO) or the β2-selective agonist clenbuterol leads to bone loss[88,111,112]. Similarly, pharmacologic blockade with the non-selective βAR antagonist propranolol protects from bone loss, but only in conditions of increased bone turnover such as estrogen deficiency[88,113,114], further supporting the bone-catabolic effect of the β(2)AR. However, several further contradictory experiments on βARs confound these results. In a mouse hindlimb suspension model of disuse osteoporosis, treatment with the β1AR agonist dobutamine protected unloading-induced bone loss [115,116]. Furthermore, mice lacking all three βARs (β1, β2, and β3) have increase bone mass and decreased resorption[117], similar to the global $\beta2AR^{-/-}$ mice[12]. However, this triple knockout mouse was obese, and lost bone upon ovariectomy and during aging[117], in contrast with the $\beta2AR^{-/-}$ mice which protected from ovariectomy-induced bone loss and gained bone mass during aging[12,88]. Finally, mice with β1AR deletion has low bone mass that did not improve with increased compression loading to simulate exercise, which was in contrast with mice with β2AR deletion[118]. These results suggest that

βARs have pleotropic have functions in bone. The β1AR$^{-/-}$ mice had decrease serum insulin-like growth factor 1 (IGF1), which is important for bone growth and may account for the differential phenotype[119]. The osteoblast-specific β2AR deletion was sufficient to protect bone from ISO-induced bone loss, strongly supporting the cell-specific function of this receptor[89].The global constitutive nature of the multiple-βAR deletion experiments [113,117,118]makes interpretation difficult. However, a well-known function of the β1AR is the positive chronotropic and inotropic effects on cardiac output. Furthermore, hindlimb suspension models may not emulate only the unloading – as seen in prolonged bedrest – but also the hemodynamic redistribution of blood – similar to spaceflight [21,120]. It is thus possible that deletion of the β1AR added an additional mechanism of bone loss that is distinct from the direct action of SNS on osteoblasts.

The presynaptic autoinhibitory αARs present a way to investigate how modulation of upstream SNS, as opposed to downstream osteoblast signaling, affects skeletal physiology. Global genetic deletion of both α2A- and α2C-ARs resulted in mice with the expected elevated serum NE, putatively due to defects in autoregulation of SNS terminal NE release. However, female mice of this genotype had *increased* bone mass, in direct contrast with the elevated sympathetic tone[121]. Deletion of the α2C-AR in mice showed the expected elevated SNS tone and low bone mass in the appendicular skeleton, but high bone mass in the axial skeleton[122], similar to the differential bone phenotype seen in *ob/ob* mice[101]. While the βAR and αAR sets of genetic deletion studies yield valuable information on the effects of these genes on bone biology, the global constitutive nature of these studies makes precise interpretation difficult. It is necessary to pursue evidence that support mechanisms of cell- and tissue-specific functions of SNS action in bone.

Bone biology during aging

The pathophysiologic process of aging is a combination of degenerative, depleting, and accumulative factors that result in organ dysfunction. In the skeleton, these factors are also present and result in senile (age-related) osteoporosis. Once the skeleton achieved maturity at peak bone mass, around 25-30 years old, bone is lost at a steady 0.5% per year in both genders[17], independent of other factors. The increased skeletal fragility leads to increased fracture risk, which predisposes the aging population to increased mortality associated with fractures[18]. Currently, the treatments for osteoporosis target just the bone remodeling pathways, either by anabolic agents or anti-resorptives. However, these do not address the underlying mechanisms of senile osteoporosis. Thus, it is important to both better identify, understand, and diagnose the pathophysiologic mechanisms underlying age-related bone loss.

Bone cellular changes with age

The maintenance of integrity of any organ is directly related to the regenerative capacity of the tissue and cells. For the skeleton, the bone-forming osteoblasts serve to rebuild bone, and bone-resorbing osteoclasts clear structurally damaged tissue. These cells derive from a pool of mesenchymal or hematopoietic stem cells which are depleted with age, leading to overall decreased bone turnover and skeletal fragility[123]. Another proposed mechanism involves reactive oxygen species, which causes oxidative damage, accumulating in the skeleton and bone cells throughout the lifespan[123]. Mice deficient in the antioxidative gene *Sod1* have decreased bone mass that exacerbates with age, and phenotypically resemble wild-type naturally-aged animals such as increased cortical porosity, low bone turnover, and age-related changes in collagen cross-linking[123,124]. Osteocytes, which are terminally differentiated cells that are critical for initiating and regulating bone remodeling, are necessary to maintain skeletal integrity. As the skeleton ages, osteocytes continually undergo apoptosis [125] leading to empty lacunae

the cortex of aged animals[125]. Coupled with the decreased osteoblast genesis potential, the depletion of the resident homeostatic cell may be etiologic to bone loss.

Gaps in knowledge of SNS-bone interactions

Despite the abundant data available on sympathetic nervous system actions on bone biology, there are still large gaps in understanding. A large number of key genetic and pharmacologic studies have demonstrated the role of certain receptors, ligands, or other proteins in skeletal homeostasis. However, only a small proportion of these provide the tissue- or cell-level resolution of these mechanisms. Thus, interpretation of results from global genetic animal models or systemic experiments is made difficult by possible confounding mechanisms that may be independent on bone.

Previous results showed that osteoblasts only express the β2AR[88], and stimulation of the receptor leads inhibition of osteoblast proliferation via cell-autonomous circadian genes *Per* and *Cry*[95], and stimulating RANKL production to promote osteoclast differentiation[88]. These two actions cannot occur within the same cell, as the anti-proliferative action of NE relates to pre-osteoblasts, whereas osteocyte-derived RANKL plays a predominant role in bone remodeling[13]. Thus, it is not known whether adrenergic receptor expression changes during the osteoblast differentiation cycle, and whether this mechanism may account for the pleiotropic effect of adrenergic stimulation on osteoblasts during different stages of differentiation. Furthermore, the norepinephrine transporter has been shown to be important for proper bone mass *in vivo*[83]. It is proposed that osteocytes, the resident cells that comprised the majority of bone stroma, are important for NE regulation via NET. However, the function and expression of NET throughout BMSC differentiation is not known. In chapter 2, we hypothesize that mature osteoblasts express both the β2AR and NET, and that their acute function can be demonstrated *in vitro* (**Fig. 1.2A**). Furthermore, while chronic studies demonstrate gene expression in response to SNS signaling[88,126], and extracellular NE levels are changed with NET inhibition[83], it does not preclude possible

intermediate mechanisms that may act on the chronic scale. Thus, we hypothesize acute adrenergic stimulation and [^{3}H]-NE uptake is observable *in vivo* (**Fig. 1.2B**). These results will help validate that the molecular mechanisms of uptake and signaling proposed using chronic studies are true for acute *in vitro* and *in vivo* systems.

Age-related bone loss is a multifactorial disease with no single cause. In other organ systems, basal SNS tone increases with age[127,128]. In Chapter 3, as SNS activity can lead to bone loss, we hypothesize that the skeleton in older animals has increased basal levels of the NE. Furthermore, we also hypothesize that this increase occurs in parallel with decreased NET expression and function (**Fig. 1.3**). This leads to the possibility that decreased uptake is a cause for the elevated NE, and a potential mechanism for age-related bone loss.

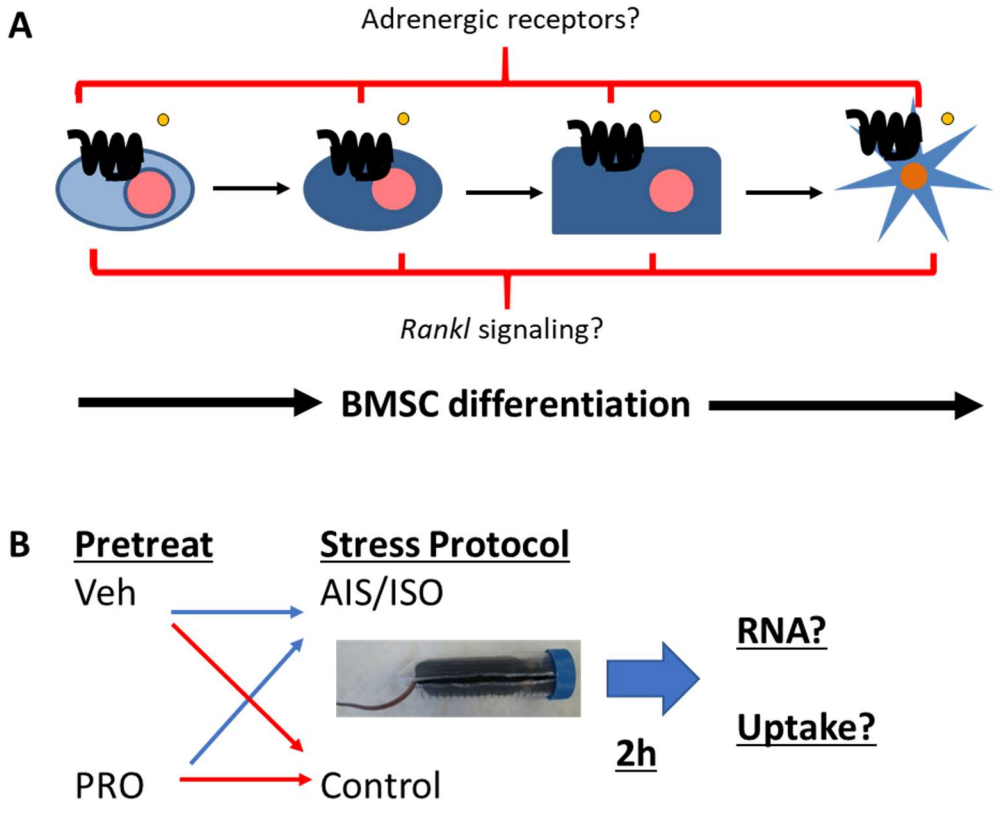

Figure 1.2 – Gaps in knowledge: acute adrenergic pharmacology

(**A**) What is the adrenergic receptor expression, ISO/NE-mediated gene expression, and acute [^{3}H]-NE uptake in differentiated BMSCs *in vivo?*
(**B**) Does bone signal via adrenergic receptors in response to ISO/NE stimulation, and acutely uptake [^{3}H]-NE *in vivo?*

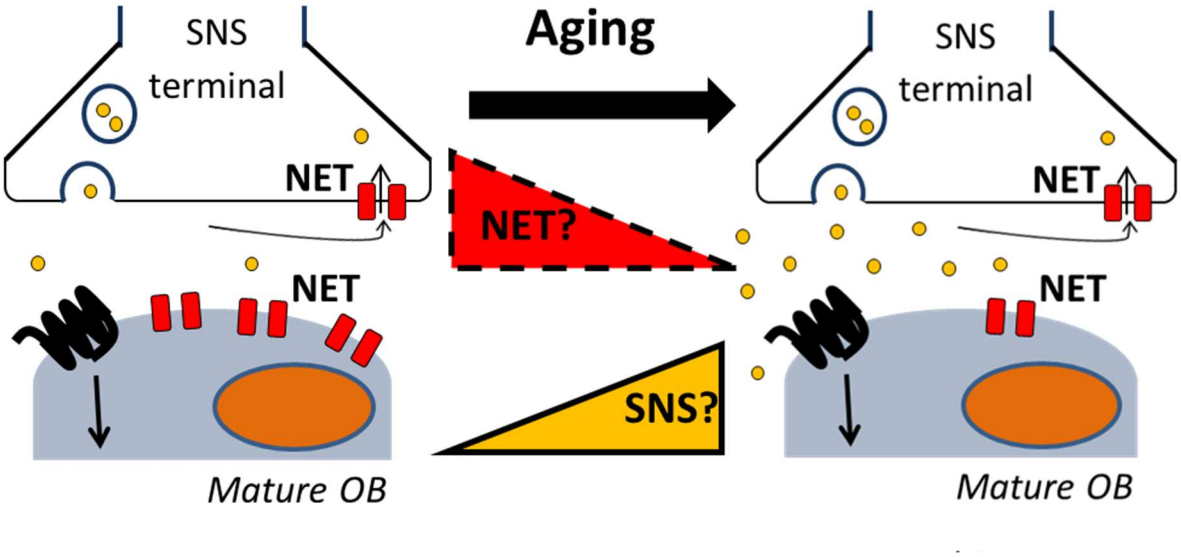

Figure 1.3 – Gaps in knowledge: skeletal sympathetic changes with age
Does NET expression and function decrease, and basal SNS activity increase in mice with age?

Finally, the proposed mechanism of SNS action is via sympathetic release of NE onto osteoblasts. The direct SNS-osteoblast interactions have yet to be visualized. As NET has been shown to be expressed and functional in mature differentiated osteoblast *in vitro*, we also hypothesize that osteocytes express NET *in vivo* (**Fig. 1.4A**). Furthermore, the previous genetic deletion models do not preclude the possibility that mature osteoblasts/osteocytes are the true target of SNS action. If this is true, we would also expect SNS innervation to be in close proximity of its site of action – i.e. bone lining osteoblasts or matrix-embedded osteocytes (**Fig. 1.4B**). These results will provide a better visual understanding of the cellular architecture of the SNS in bone.

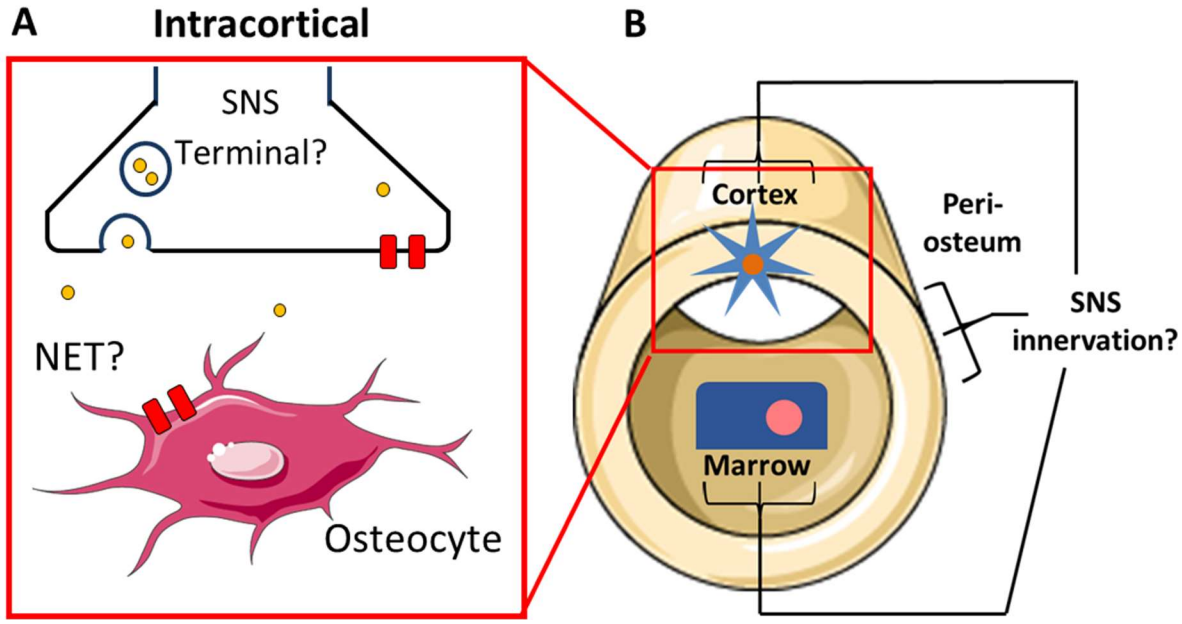

Figure 1.4 – Gaps in knowledge: innervation of bone by the SNS
(**A**) Do matrix-embedded osteocytes express NET *in situ*?
(**B**) Do SNS fibers innervated the bone cortex in close approximation to osteocytes?

Chapter 2. Acute Function of SNS in Bone

Introduction

Adrenergic pharmacology of osteoblast during differentiation

The current paradigm of sympathetic nervous system (SNS) action on skeletal metabolism involves activation of the β2-adrenergic receptor (β2AR) on osteoblast to cause the expression of osteoclastogenic genes such as *Rankl* and *Il6*, leading to bone loss[89]. The mechanisms of interaction were elucidated using genetic mouse models, chronic pharmacologic treatments, or chronic stress protocols, and have been instrumental in demonstrating the necessity of components in the SNS-bone axis. In parallel, acute cellular mechanisms of sympathetic or sympathomimetic action were elucidated using osteoblast-like cell lines [12,112,129]and primary osteoblasts. A genetic mouse model with osteoblast-lineage specific deletion of β2AR *in vivo*, with the floxed *Adrb2* allele inactivated by expression of Cre recombinase under the *Coll(2.3kb)* osteoblast-specific promoter, showed that the osteoblastic b2AR was sufficient for increased bone mass[89]. However, other *in vivo* genetic mouse models of *Rankl* deletion in specific stages of osteoblast differentiation showed that specifically osteocytes, not osteoblasts, are phenotypically important for the promotion of osteoclast differentiation[13]. In addition to the target cell of SNS action in bone, uncertainty also exists of which adrenergic receptor is expressed and active in osteoblasts. Several observations report multiple adrenergic receptors are expressed and functional on osteoblast-like cell lines[130]. Gene expression for several adrenergic receptors was detected in whole mouse bones[118], though this was attributed to possible other cell types in bone (e.g. adipocyte, endothelium, hematogenous, etc.). While the end result of SNS action on bone biology is well-described across these studies, the precise cellular timing and mechanisms – which adrenergic receptor are expressed in osteoblasts, and how this expression changes during differentiation – is not entirely clear.

Therefore, it is important to determine the adrenergic receptor expression profile and the adrenergic agonist response throughout the stages of osteoblast differentiation.

Coupling rapid SNS signaling to slow action of bone biology

Many tools are available to study adrenergic receptor physiology, such as a variety of available pharmacologic ligands, signaling pathways, and physiologic mechanisms to target. Similarly, when interpreting experiments involving sympathetic nervous system modulation *in vivo*, the targeted and potential systemic off-target mechanisms vary greatly depending on the adrenergic receptor. Sympathetic nervous system physiology is best understood on the order of seconds: nerve terminal neurotransmitter release, diffusion, binding on cognate receptors on target cells, and the resulting signaling cascade. Bone metabolic processes occur much slower: osteoblast-coupling, bone formation and resorption, and cell differentiation. The majority of previous studies on the role of SNS function in bone highlight the result of constitutive genetic [88,89,118,131,132]or chronic pharmacologic treatments [6,12,111,115,133–137] on bone mass. However, whether acute *in vivo* stimulation results in these skeletal responses is unknown.

Identifying the neurochemical function of NET in bone

Further elucidation of the role of SNS in normal physiology and skeletal pathologies is hindered by our limited understanding of both its physiology and its neurochemical function in the skeleton. We have previously reported that the norepinephrine transporter (NET), a pump that uptakes NE from the extracellular environment, plays an important role in the regulation of bone remodeling[83], as global *Net* deletion results in low bone mass in mice. Although lack of NE reuptake by SNS terminals in bone would be expected to cause bone loss via increased NE spillover to the bone microenvironment, this low bone mass phenotype was unexpectedly accompanied by low skeletal NE content, which according to the

above model should promote bone gain. Investigating this contradictory result led us to show that NET is expressed not only in skeletal presynaptic neurons, but also in osteoblast-lineage cells, and to demonstrate specific *Net* expression and NE uptake in differentiated osteoblasts *in vitro*[83]. This work led us to hypothesize that NET has an extraneuronal role in bone to locally limit the action of NE on the skeleton, thereby buffering the catabolic function of the SNS on this organ. However, due to the global and constitutive nature of the model, it is difficult to conclude the mechanistic function of NET in bone.

During the course of our preliminary studies, we also found that endogenous sympathetic activation by daily restrain stress, which releases the neurotransmitter NE, is not sufficient to lead to decreased bone mass. On the other hand, chronic treatment of mice with isoproterenol (ISO), a non-selective βAR agonist insensitive to NET reuptake, does cause bone loss via increased bone resorption. These data suggest that the skeleton is protected by NET from the deleterious effects of NE on bone remodeling. This notion is further supported by the observation that mice with global genetic deletion of NET (Net KO) have low bone mass, despite decreased markers of sympathetic outflow (commonly associated with bone gain) compared to WT mice. Thus, the paradigm of NE released by sympathetic nerves directly acting on osteoblasts to reduce bone mass is incomplete, and our preliminary data suggest the existence of a homeostatic regulatory mechanism controlling the action of the SNS on bone. In that regard, the *in vivo* regulation and function of NET in the bone microenvironment and the putative mechanisms through which NET attenuates the deleterious effect of excess SNS activity on bone remodeling remain to be determined. However, the constitutive and ubiquitous nature of the global *Net* knockout animal model limits further elucidation of these mechanism(s).

As NET is expressed in both sympathetic neurons and mature osteoblasts it is unknown in which cell lineage NET deletion is mechanistically responsible for the low bone mass phenotype seen in global Net KO mice. Classically, NET located on sympathetic synaptic terminals acts to limit the magnitude and duration of NE on target tissues through reuptake. However, the few reports studying noradrenergic

nerve terminal density in bone suggests it is relatively low compared to osteocytes. These cells indeed compose approximately 90% of the cellularity in the bone matrix[61] and are thus postulated to account for the majority of NE clearance in bone. Therefore, to support claims that skeletal NET indeed serves as a catabolic sink for NE in bone, it is necessary to demonstrate that bone tissues are capable of specific NE uptake *in vivo*, and that this is mediated through the norepinephrine transporter.

This chapter will present data on acute SNS signaling and regulation *in vitro* and *in vivo*. This will be accomplished by first identifying the putative target of SNS action in the osteoblast lineage and *in vivo*, as well as demonstrated acute NE uptake in cell cultures *in vitro* and in tissues *in vivo*. These results will establish the pharmacologic basic and cellular target of SNS action the osteoblast lineage. They will also define the acute function of specific neurotransmitter uptake in pure *in vitro* cell populations and in bone tissues *in vivo*, and allow future investigation into the consequences of chronic SNS action in the setting of bone biology.

Results

Primary BMSCs express the functional β2AR during differentiation

To better understand and interpret experiments involving SNS and bone, it is important to identify the adrenergic receptor expression profile in osteoblasts through differentiation. To accomplish this, we measured by qRT-PCR the expression of all 9 adrenergic receptors in primary bone marrow stromal cells (BMSCs), differentiated in osteogenic medium for 2, 14, and 28 days. Either N1E-115 murine neuroblastoma cells (N1E), or tissue lysate of brainstem (Br) or intrascapular brown adipose tissue (BAT) were use as positive controls. Ovary tissue lysate (Ov) was used as negative control and lower limits of detection (dotted gray line). Only *Abrb2*, encoding the β2AR, was significantly expressed in BMSCs throughout differentiation (**Fig. 2.1A**), showing expression as early as 2 days into *in vitro*

osteogenic induction, and persisting until at least 28 days. Acute 2h stimulation of differentiated BMSCs with the pharmacologic non-selective βAR agonists Isoproterenol (ISO), or the endogenous sympathetic neurotransmitter norepinephrine (NE), elicited expression of *Rankl* (**Fig 2.1B**) and *Il6* (**Fig. S2.1B**). This expression response was only in 14- and 28-day, and not in 2-day differentiated cells. This gene expression response was also inhibited by pre-treatment with the non-selective βAR antagonist propranolol (PRO). These results show that primary BMSCs express the β2AR, and not other adrenergic receptors, throughout differentiation. Furthermore, these cells express osteoclastogenic genes in response to adrenergic agonism.

Differentiated primary BMSCs express functional NET

In pre-synaptic neurons, NET reuptake serves a dual role: it limits synaptic NE signaling, and recycles NE for subsequent repackaging and re-release. In osteoblasts, *Net* expression increases during differentiation in parallel to the osteoblastic marker *Ocn* and mature osteoblast/osteocyte marker *Sost* (**Fig. 2.2A**). NET protein expression was detectable by Western Blot as early as 7-days post-differentiation, with the highest amount in 28-day differentiated BMSCs (**Fig. 2.2B**). Expression of NE catabolic enzymes, including catechol-O-methyltransferase (*Comt*) and the peripheral isoform of monoamine oxidase (*Maoa*) was also detected throughout *in vitro* differentiation and in bone cortical tissues (enriched in osteoblast/cutes) by qRT-PCR. However, osteoblasts and cortical bone tissues did not express genes encoding enzymes for catecholamine synthesis, tyrosine hydroxylase (*Th*) and dopamine-β-hydroxylase (*Dbh*); or vesicular repackaging, vesicular monoamine transporters 1 and 2 (*Vmat1/2*) (**Fig. 2.2C**). These results suggest that mature osteoblasts/osteocytes possess the capability as extraneuronal sites of NE uptake and catabolism.

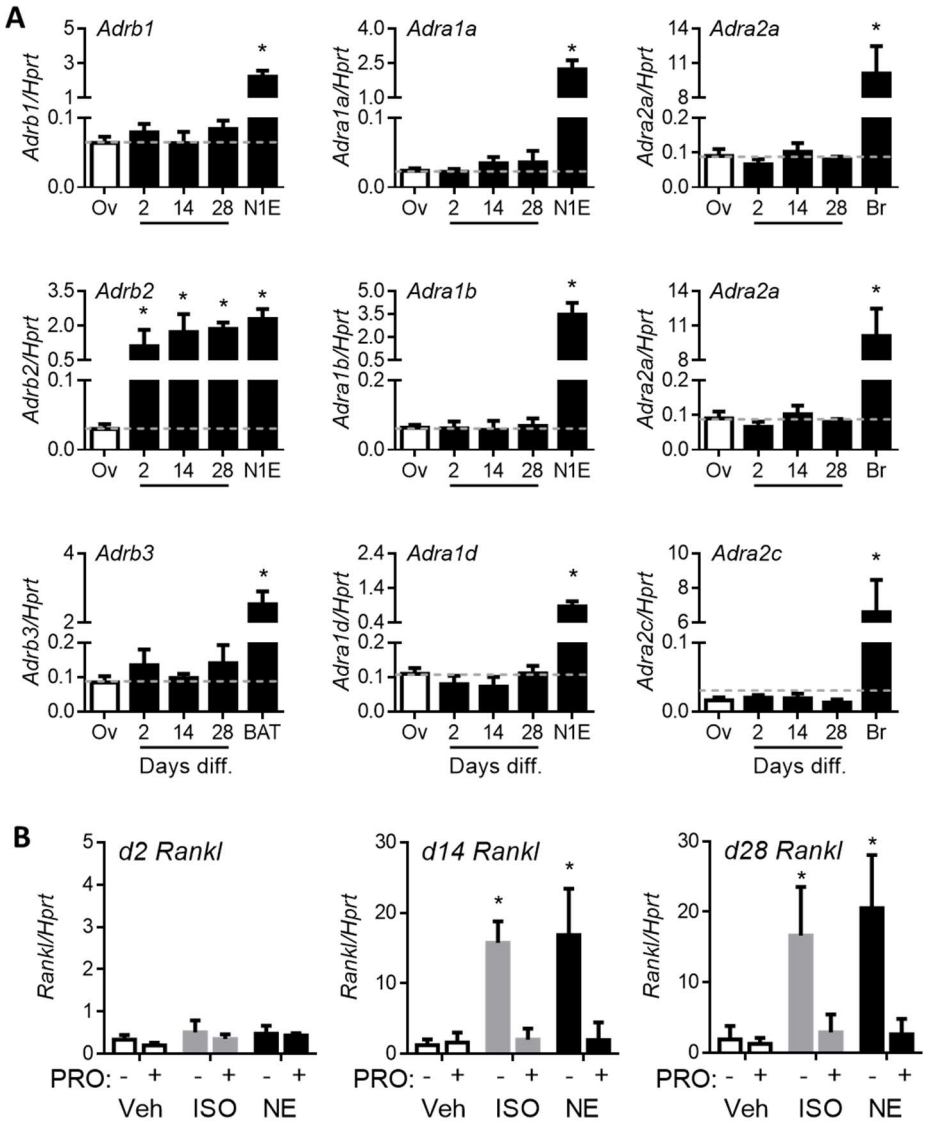

Figure 2.1 – Adrenergic receptor expression and response to acute agonist stimulation during BMSC differentiation

(**A**) Expression of genes encoding adrenergic receptors in primary BMSCs differentiated in osteogenic medium for indicated number of days, normalized to reference gene *Hprt*. Negative control from ovary tissues (Ov, dotted gray line) and positive expression controls from murine neuroblastoma cell line N1E-115 (N1E), brown adipose tissue (BAT), or brainstem (Br) normalized to reference gene *Hprt* (n = 4 per group).

(**B**) Differentiated BMSCs gene expression of *Rankl*, pretreated with isoproterenol (ISO, 1 uM), after 2h treatment with vehicle (Veh), isoproterenol (ISO, 1 uM), or norepinephrine (NE, 1 uM) (n = 4 per time point treatment).

All results are shown as mean +/- SD. Statistical analysis by one-way ANOVA, post-hoc Dunnett's statistical test for significance vs dH2O control (**A**); or by two-way ANOVA, post-hoc Dunnett's statistical test for significance vs ISO Veh control of each differentiation timepoint (**B**); * $p<0.05$.

In addition to NET, other transmembrane transporters exist that are capable of monoamine uptake. The Organic Cation Transporters 1 and 2 (OCT1/2), and Extraneuronal Monoamine Transporter (EMT) are high-capacity, low-affinity transporters that are promiscuous for other molecules aside from monoamines such as NE[79,80,138]. Differentiated BMSCs express genes encoding these transporters (**Fig. 2.3A**), suggesting the capacity of these cells to uptake NE via mechanisms besides NET. However, given the high affinity and specificity of NET to NE, we hypothesized that NET was the major uptake mechanism in osteoblast *in vitro*. To address this, we measured the acute uptake of the tritiated radioligand [^{3}H]-NE in BMSCs at different stages of differentiation. To determine specificity to NET-mediated uptake, we pre-treated cells with either reboxetine (Reb, a NET blocker) or Vehicle. Osteoblasts had significantly more uptake of [^{3}H]-NE after 14 and 28 days of differentiation than compared to 2-day (**Fig. 2.3B**). These results are consistent with the RNA and protein expression data on NET expression increasing during differentiation. However, only BMSCs differentiated for 28-days showed specific uptake that was inhibited by reboxetine pretreatment, indicating that reboxetine-insensitive mechanisms may account for the uptake in these cells. Taken together, these results suggest that late-stage *in vitro* differentiated BMSCs express NET, and are capable of specific NE uptake.

Acute *in vivo* adrenergic signaling in bone

Studies of *in vitro* differentiated BMSCs allow specific interrogation into osteoblast-lineage cell expression and function with relation to adrenergic signaling molecules. However, whether these *in vitro* results translate to murine bone physiology *in vivo* needs to be demonstrated. We therefore asked whether acute adrenergic stimulation *in vivo* can elicit gene expression response similar to BMSCs. To achieve this, we treated animals for 3h with either isoproterenol (ISO, 3 mg/kg body weight, i.p.), saline vehicle, or subject the animals to a 3h acute immobilization stress (AIS) protocol designed to elicit endogenous SNS release as a part of the natural "fight or flight" stress response[6,139], and measured gene

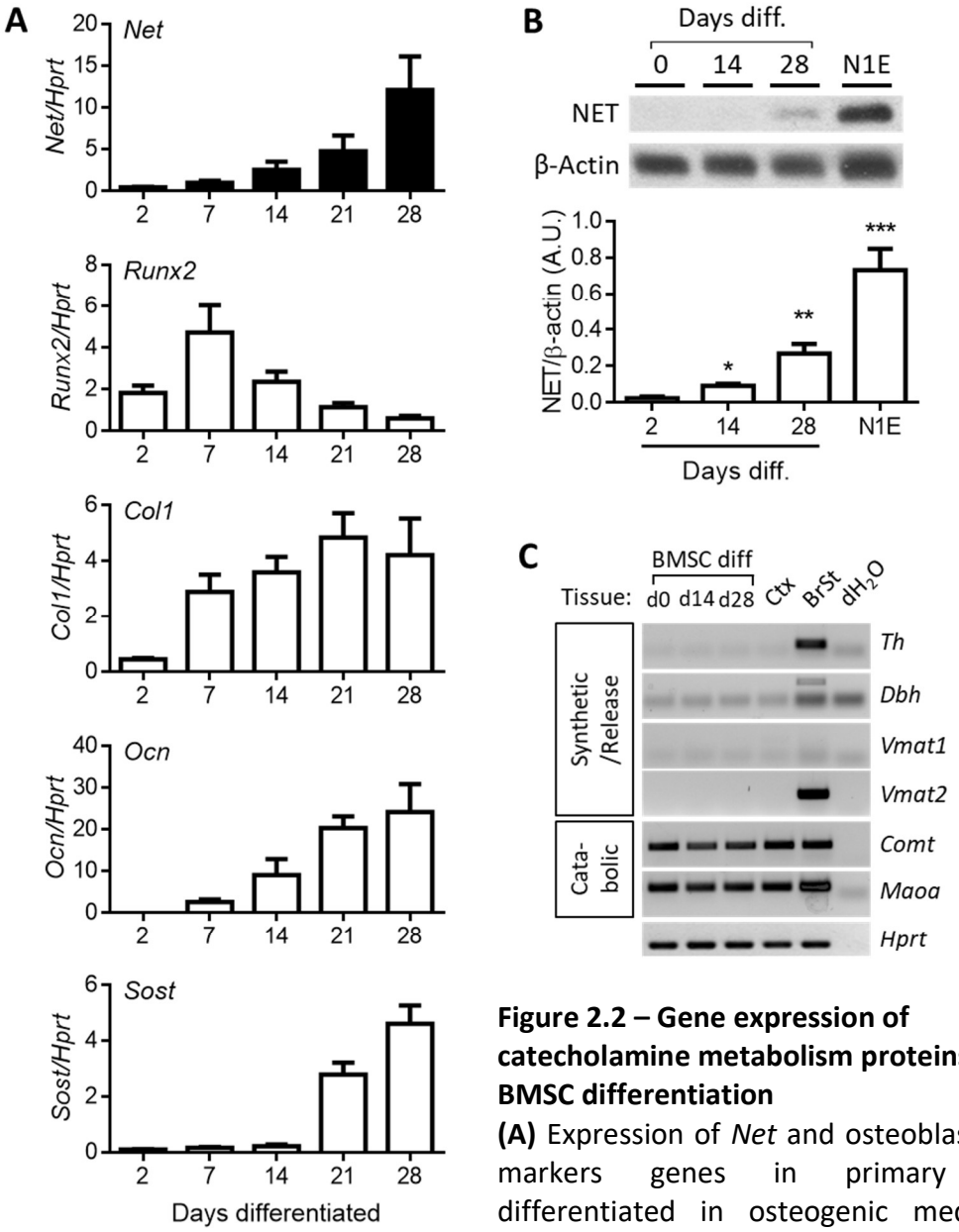

Figure 2.2 – Gene expression of catecholamine metabolism proteins during BMSC differentiation

(A) Expression of *Net* and osteoblast lineage markers genes in primary BMSCs differentiated in osteogenic medium for indicated number of days. Gene expression was normalized to reference gene *Hprt* (n = 4 per time point).

(B) Representative Western blot bands and quantification of NET protein expression in differentiated BMSCs and murine neuroblastoma cell line N1E-115 positive control (N1E), normalized to reference protein β-actin (n=3 per group).

(C) Semi-quantitative qPCR of differentiated bone marrow stromal cells (BMSC), tibial cortical tissues (Ctx), and brainstem (BrSt) for genes encoding enzymes related to catecholamine metabolism and synthesis.

All results are shown as mean +/- SD. Statistical analysis by one-way ANOVA, post-hoc Dunnett's statistical test for significance vs dH2O control; * p<0.05.

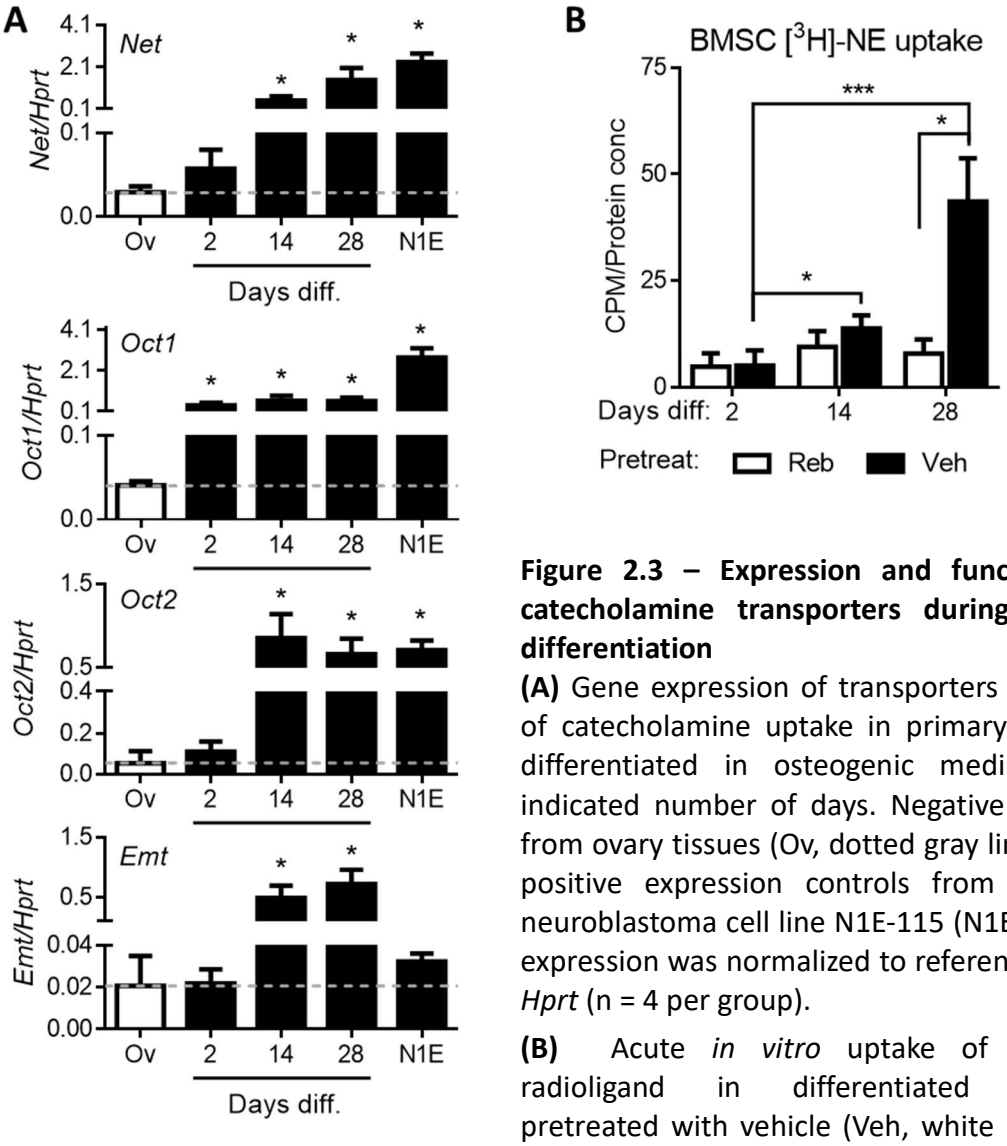

Figure 2.3 – Expression and function of catecholamine transporters during BMSC differentiation

(A) Gene expression of transporters capable of catecholamine uptake in primary BMSCs differentiated in osteogenic medium for indicated number of days. Negative control from ovary tissues (Ov, dotted gray line), and positive expression controls from murine neuroblastoma cell line N1E-115 (N1E). Gene expression was normalized to reference gene *Hprt* (n = 4 per group).

(B) Acute *in vitro* uptake of [^{3}H]-NE radioligand in differentiated BMSCs pretreated with vehicle (Veh, white bars) or the NET blocker reboxetine (Reb, black bars). Radioactivity of cell lysates was measured by scintillation counting (CPM) and normalized to lysate protein concentration (n = 5 per treatment per time point).

All results are shown as mean +/- SD. Statistical analysis by one-way ANOVA, post-hoc Dunnett's statistical test for significance vs control (**A**); or by two-way ANOVA, post-hoc Holm-Sidak statistical test for pair-wise significance (**B**); * p<0.05, ** p<0.01, ***p<0.001.

expression in the bones from these animals. Whole tibia gene expression of *Il6* was significantly higher in both ISO and AIS-treated animals compared to controls, whereas *Rankl* was only higher in ISO-treatment (**Fig. 2.4A**). These results show that acute endogenous NE release can be detected in bone, but this effect is different from pharmacologic βAR agonism.

To further determine the selectivity of the skeletal response to AIS, animals were pretreated with the non-selective βAR antagonist propranolol (Pro) prior to AIS. There was a significant increase in whole tibia *Il6* expression after AIS, confirming our previous result, and this effect was blocked by propranolol pretreatment (**Fig. 2.4B**). Also similar to the previous result, no difference in *Rankl* expression after AIS was detected. These results suggest that AIS causes endogenous SNS release of NE, which acts in bone to increase *Il6* expression, and that this effect is mediated through a βAR. However, neither the target nor source of *Il6* is demonstrated through these experiments. Furthermore, although the AIS-influence is blocked by propranolol, it is still possible that intermediate mechanisms mediate the effect of AIS on *Il6* expression.

Acute *in vivo* [3H]-NE uptake in bone

NET is well known to be expressed in presynaptic sympathetic neurons[78], but was also unexpectedly detected in neonate osteoblasts by immunohistochemistry, and in fully differentiated bone marrow and calvaria osteoblasts *in vitro* at both RNA and protein levels[83]. Most importantly, our data showing this transporter to be active in these cells, as specific uptake of the tritiated NE ([^{3}H]-NE) radioligand was detected in these differentiated osteoblast cultures *in vitro,* in line with the expression pattern of this gene in this lineage (**Fig. 2.3**). These *in vitro* data led us to hypothesize that the bone tissue is capable of specific NE uptake *in vivo*. To address this hypothesis, we adapted *in vitro* uptake methods to measure NET-mediated acute uptake of the radioligand [^{3}H]-NE in bone tissues from 6-week old adult male mice. To ensure specificity of NE uptake by NET in these measurements, mice were pre-treated twice with the

NET blocker reboxetine (Reb, 20mg/kg body weight i.p.) or sterile saline vehicle 60 and 30 minutes prior to administration of [^{3}H]-NE (10 μCi/kg body weight) via tail-vein injection to avoid excess hepatic metabolism. The radioligand was allowed to circulate for 10 minutes, after which the animals were rapidly euthanized, and tibiae and femurs were harvested. Tissues were lysed, [^{3}H]-NE was quantified by scintillation counting (CPM), and normalized by tissue DNA content (as an indirect readout for cell number). Bone cortex tissue (Ctx) had more [^{3}H]-NE uptake than marrow (Marr) per cellularity. This cortical uptake was significantly blocked by reboxetine pre-treatment, whereas marrow uptake did not differ (**Fig. 2.4C**). These results indicate that tibia and femur cortical tissues are capable of significant NET-mediated uptake.

Discussion

There exists some debate on the expression of adrenergic receptors in osteoblasts. Several groups report expression of αAR in osteoblasts, and demonstrate a function of αAR signaling in these cells[130,131]. However, many of these observations were made in osteoblast-like cells lines. In accordance with our findings that β2AR, and not β1-, β3-, or any αARs, was expressed in BMSCs throughout differentiation, several other groups have verified that the *Adr2b* is the only adrenergic receptor expressed in primary murine osteoblasts[12,88,140,141]. However, expression and function of both β2AR and α1bAR have been shown on primary human osteoblast culture[130]. While these contradict our findings in mice, many physiologic differences exist between the two species, and may explain the difference in results. The *Adrb2* is expressed in BMSCs as early as differentiation day 2, which correspond to the osteoprogenitor cell pool *in vivo*, but do not express either *Rankl* in response to adrenergic signaling. This is consistent with the fact that pre-osteoblasts are not considered responsible for osteoclastic induction, and that this is the function of mature osteoblast/osteocytes[13,142]. However, this does not

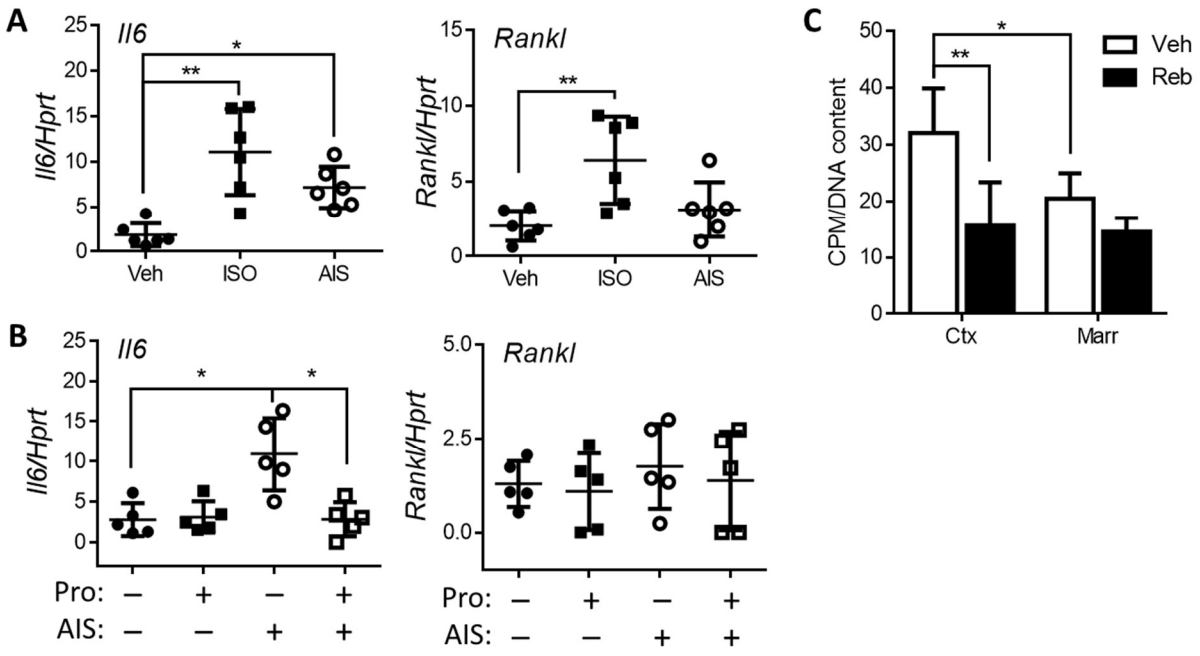

Figure 2.4 – *In vivo* adrenergic signaling and acute [3H]-NE specific uptake *in vivo*

(**A**) Gene expression in response to acute pharmacologic or endogenous adrenergic stimulation. Gene expression of *Il6* and *Rankl* in whole tibia from mice treated with control saline (Veh i.p.), the βAR agonist isoproterenol (ISO, 3mg/kg i.p.), or subject to acute immobilization stress protocol (AIS). Gene expression was normalized to reference gene *Hprt* (n = 6 per treatment).

(**B**) Gene expression of *Il6* and *Rankl* in whole tibia from mice were pretreated with either vehicle or the β-blocker propranolol (Pro, 5mg/kg i.p.), and subject to either acute immobilization stress (AIS) or control protocol. Gene expression was normalized to reference gene *Hprt* (n= 5 per group).

(**C**) *In vivo* uptake of [^{3}H]-NE radioligand in the femoral cortex (Ctx) and marrow (Marr). Mice were pre-treated with either vehicle control (Veh, white bars) or the NET blocker reboxetine (Reb, black bars) (n = 10 animals).

All results are shown as mean +/- SD. Statistical analysis by two-way ANOVA, post-hoc Dunnett's statistical test for significance vs Veh control (**A**); post-hoc Bonferroni statistical test for pair-wise significance (**B**); or two-way ANOVA, post-hoc Holm-Sidak for pair-wise significance (**C**), * $p<0.05$, ** $p<0.01$.

preclude these BMSCs early in differentiation from responding to adrenergic signaling. In other studies, perivascular cells – a population of mesenchymal stem cell defined by their anatomical location and

expression of markers are able to respond to sympathetic signals, and effect hematopoietic stem cell egress from the bone microenvironment[56,57,142]. While these pericyte cells are not necessarily the same as BMSCs (which are defined by their adherence during tissue culture), the expression of β2AR in early BMSCs may serve a role in processes besides bone formation.

While *Adrb2* and non-specific transporters (*Oct1*/2*, Emt*) are expressed throughout BMSC differentiation (**Fig. 2.1A** and **2.3A**), *Net* gene and protein expression increases during differentiation – increasing in parallel with mature osteoblast/osteocyte markers *Ocn* and *Sost* (**Fig. 2.2**). The relevance of NET function in late BMSCs was demonstrated by *in vitro* uptake assays. Both d14 and d28 BMSCs has significant [^{3}H]-NE uptake, which d28 BMSCs having approximately 3-fold higher uptake compared to d14. However, only d28 BMSC uptake was inhibited by reboxetine pre-treatment (**Fig. 2.3**). These results suggest that NET is the major uptake transporter through which mature osteoblasts/osteocytes uptake NET, while d14 osteoblast-like BMSCs are capable of uptake through other mechanisms. Extrapolating these results into *in vivo* physiology, mature osteoblast/osteocytes are the

The amount of endogenous NE released by sympathetic nerves is controlled presynaptically by NET, whose NE uptake function accounts for 80-90% of NE released by central and peripheral neuron[78]. NE reuptake thus constitutes an important negative feedback mechanism to limit the duration of sympathetic signaling and to replenish NE stores in sympathetic nerve fibers[139,143]. The low bone mass phenotype of mice globally deficient for *Net* indicated this transporter is important for bone remodeling [83]. However, how NET modulates bone mass remains unknown, although our previous *in vitro* evidence suggest that differentiated osteoblasts might contribute to NE uptake in bone *in vivo*. There could be two functions of NET in the bone microenvironment: by sympathetic neuron reuptake and repackaging for subsequent release, or by uptake and metabolism by osteoblasts (and possibly neurons). Cortical

bone tissues uptake of [^{3}H-NE] is significantly higher than in marrow, suggesting that cortical tissues is a larger catabolic sink for NE (**Fig 2.4C**). There was also a significant reduction in cortical, but not marrow, uptake with reboxetine pre-treatment, suggesting that bone cortex uptake has a significant NET-mediated component. The non-specific uptake, seen in reboxetine-pretreated tissues, could be either remaining [^{3}H]-NE in circulation or interstitial fluid that was not cleared in the short timeframe of the experiment, non-specific binding of the radioligand to other tissues, or represent uptake by mechanisms other than NET (e.g. OCT1/2, Emt, or other transporters). Furthermore, these studies do not differentiate between the proposed functions of osteoblastic (catabolic) or neuronal (re-packaging) NET.

To address the specific site and role of NET in the bone microenvironment, future experiments with tissue-specific genetic deletions of *Net* are needed. Sympathetic neuronal deletion of a floxed *Net* allele could be mediated by e.g. via *Th-Cre*, or a peripherally inducible pan-neuronal Cre recombinase such as *Thy1-Cre/ERT2*. The latter would allow fine temporal control of genetic sympathectomy to eliminate the confounding factors of development, and possibly allow final anatomical control of *Cre* induction with tamoxifen delivery in a unilateral limb. According to our studies, bone NET is primarily expressed and functional in mature osteoblast/cytes. Thus, a late osteoblastic/osteocytic mouse strain such as *Dmp1-Cre*, the inducible *Dmp1-Cre/ERT2* and *Ocn-Cre/ERT2*, would address whether osteocytic *Net* deletion impacts bone metabolism *in vivo*.

The acute *in vivo* adrenergic stimulation of bones showed that the pharmacologic agonist isoproterenol, but not endogenous stress released during AIS, can elicit increased gene expression (**Fig 2.4A** and **B**). In other studies, this acute effect can be extrapolated to the chronic impact on bone mass by ISO[88,118], but not chronic immobilization stress alone[83,126,144,145]. This may be due to the fact that the norepinephrine transporter can uptake endogenous NE released during stress, but not the synthetic ligand ISO[146]. It is also possible that differences in potency of agonisms, ligand metabolism (which is related to NET uptake, but also renal and hepatic clearance), or preferences in adrenergic receptor

affinity/activity may also account for the differential effects seen in chronic studies or our acute observations. A future study would be to investigate whether NET uptake of endogenous NE release during AIS, but not exogenous ISO, is responsible for the lack of gene expression response. This could be achieved by acute NET blockade by reboxetine pre-treatment, followed by AIS. According to our model, bone tissue from these reboxetine pre-treated AIS animals would express *Il6* and *Rankl* similar to ISO, and this effect is sensitive to propranolol receptor blockade. Results from this experiment would provide a clear interpretation of our previous finding that reboxetine treatment alone is sufficient to cause bone loss in chronic immobilization stressed mice[83].

Figure S2.1

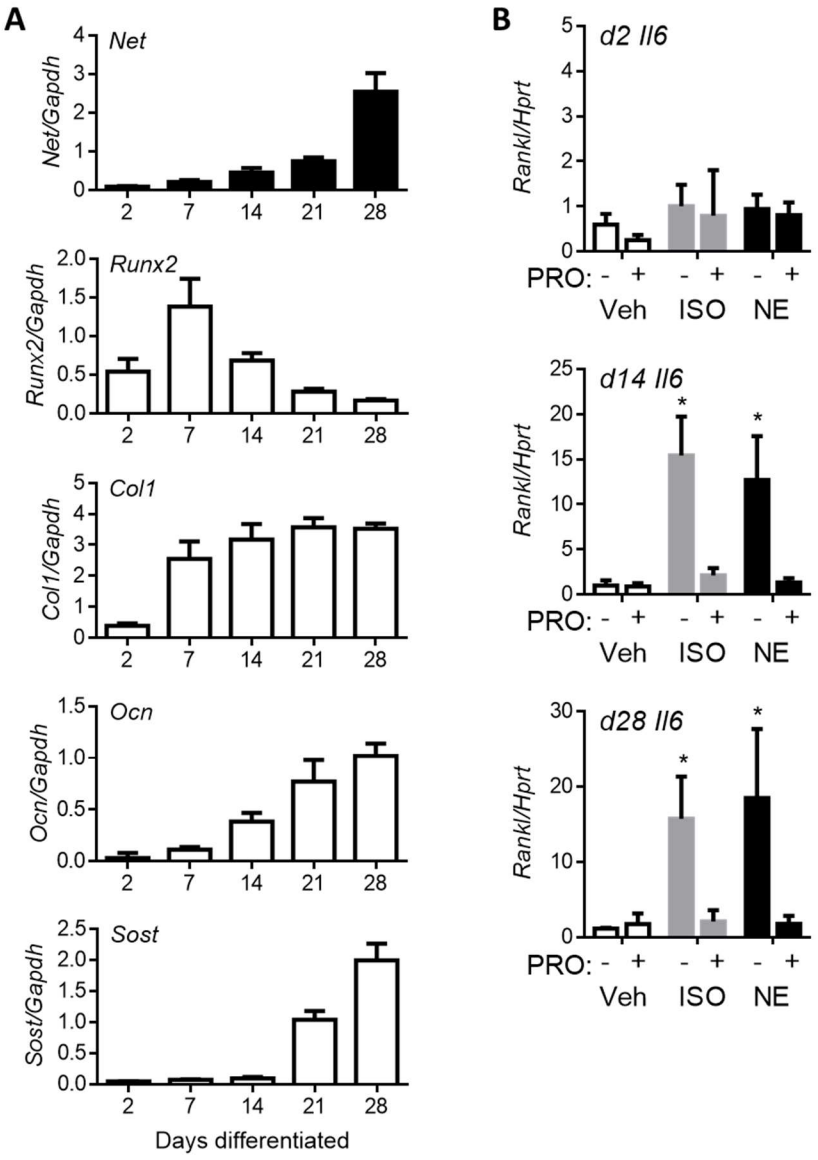

Figure S2.1 – Expression of *Net* during BMSC differetiation

(**A**) Expression of *Net* and osteoblast lineage markers genes in primary BMSCs differentiated in osteogenic medium for indicated number of days. Gene expression was normalized to reference gene *Gapdh* (n = 4 per time point).

(**B**) Differentiated BMSCs gene expression of *Rankl*, pretreated with isoproterenol (ISO, 1 uM), after 2h treatment with vehicle (Veh), isoproterenol (ISO, 1 uM), or norepinephrine (NE, 1 uM) (n = 4 per time point treatment).

All results are shown as mean +/- SD. Statistical analysis by two-way ANOVA, post-hoc Dunnett's statistical test for significance vs ISO Veh control of each differentiation timepoint (**B**); * $p<0.05$.

Chapter 3. Age-Related Changes of SNS in Bone

Introduction

Autonomic dysfunction during aging

A number of observations suggest sympathetic signaling may contribute to the continuous bone loss associated with the pathophysiology of aging. Sympathetic activity in post-menopausal women with osteoporosis was measured to be higher compared to post-menopausal women without osteoporosis[147,148]. In these studies, sympathetic nerve activity was inversely correlated with trabecular bone volume fraction, thickness and compressive bone strength. This association is further supported by indirect observations showing that bone resorption is increased in patients with pheochromocytoma[149]. Additionally, several retrospective studies showed that β-blockers had a beneficial effect on BMD and fracture risk[135,150,151]. In mice, deletion of SNS-related genes *Dbh*[12]*, Foxo1*[152]*,* or *Adrb2*[88] leads to a high bone mass phenotype that is not detectable until 5-9 months of age. These clinical and preclinical observations support a functional relationship between sympathetic tone and bone mass regulation, with highest relevance to age-related bone loss. To determine whether these patient studies translate to rodent animal models, we aimed to determine whether increased sympathetic activity exists in mice during aging.

Our lab has previously reported that the norepinephrine transporter (NET), a pump that uptakes NE from the extracellular environment, plays an important role in the regulation of bone remodeling[83], as global *Net* deletion causes low bone mass in mice. In this previous study and in Chapter 1, we demonstrated that NET is both expressed and function in mature osteoblasts. These observations, in concert with previous clinical data on increased sympathetic tone during aging, led us to ask whether NET expression and function is also perturbed during aging in mice.

Anatomical sympathetic innervation of long bones

The current paradigm of SNS action on bone physiology arose from genetic and pharmacologic studies. While these investigations provided invaluable information on the ligands, receptors, and cell lineages involved in this interaction, they were all systemic in scope. The sympathetic nervous system has both local and global arms, via direct innervation of tissues for NE-releasing SNS fibers or systemic epinephrine (Epi) release from the adrenals, respectively. Several models of global SNS ablation have been used to study SNS and bone: global chemical sympathectomy [153–156], or genetic deletion of catecholaminergic enzymes [152,157] or βAR receptors[12,88,118]. However, these models also ablated adrenal contributions in addition to peripheral SNS nerves innervating organs. Experiments in rodents with radical bilateral adrenalectomy showed that the adrenal contributions are not necessary to lead to SNS-mediated bone loss[88]. However, this surgery also removed the steroidogenic adrenal medulla, and require supplementation of cortisol in these animals to avoid Addisonian-like symptoms. It is well known that the hypothalamic-pituitary-adrenal axis affects bone homeostasis via adrenal cortisol, making the adrenalectomy mouse model difficult to interpret. Furthermore, while this adrenalectomy model demonstrates that adrenal Epi is not necessary for bone loss, it is not known whether over-activation is sufficient to lead to skeletal changes. *In vivo* models of SNS activation increase both NE and Epi release [158], and separating the effect of these two arms proves to be difficult. On the converse, the necessity of only the sympathetic nerves supplying individual bones to elicit SNS-mediated bone loss is not certain.

The anatomical structure mediating the effect of SNS on bone is believed to be sympathetic fibers directly innervating the bone or bone marrow. Nerve fibers immunopositive for the rate-limiting catecholamine synthesis enzyme tyrosine hydroxylase (TH) or the sympathetic neuropeptide VIP are present in bone[92,159–161]. Retrograde nerve tracing experiments with pseudorabies virus injection into the rabbit femur medullary cavity has confirmed sympathetic innervation of bone by pelvic splanchnic ganglia[162]. These early findings, together with the recent findings of SNS function in bone, highlight that

the bone is innervated by the SNS and that these nerves serve a physiologic function. Furthermore, sympathetic nerves surrounding the vessels supplying bone have also been identified[92,93]. Previous studies have used global chemical sympathectomy of animals to demonstrate the impact of acute SNS loss in bone in neonatal[155] and adult rats[153]. These studies focused on mandibular bone remodeling, and differences exist compared to long bone physiology[156,163]. According to Hilton's Law, bones and joints are generally innervated by the same nerve as overlying muscles[164]. The sympathetic nerve innervation of long bone medullary compartment, specifically the marrow space, has been described as co-incident with the circulatory tree, which is consistent with other organ systems such as the kidney, muscle, and liver[161,165,166]. The tibial and femoral circulation, except the femoral head, are supplied by branches of the femoral artery[167]. Thus, we hypothesized that the femoral artery, which supplies blood to the lower limb including the femoral and tibia cortex and marrow (excluding the femoral head), also exclusively carries SNS fibers innervating these organs. To demonstrate this, we aimed to unilaterally denervate the nerves surrounding the femoral artery, borrowing techniques from renal artery sympathetic denervation[168,169]. This approach has three advantages: 1.) it spares the femoral and sciatic nerves, preserving motor and sensory functions to the bone that also independently affect bone metabolism, 2.) the contralateral un-denervated limb can serve as internal controls, and 3.) the femoral artery is easily accessible for surgical manipulation.

Results

Aging leads to increased basal NE content in the skeleton

Aging is associated with an increase in basal SNS signaling in humans, a condition that might be partially responsible for the age-related decline in organ function, including the skeleton[170,171]. Therefore, we first asked whether NE bone content differed between young versus old mice. We also

subjected young mice to acute immobilization stress (AIS) to provide a physiologic baseline of SNS activation versus the non-stressed young animals. Using high performance liquid chromatography, we detected a 29% increase in NE content/mg protein in whole tibia tissue samples from 18-month versus 3-month mice, while acute stress in 3-month animals (AIS) did not lead to increased NE (**Fig. 3.1A**). The amount of the catecholamine precursor L-dihydroxyphenylalanine (L-DOPA) in these tissues was not significantly altered between 3- and 18-month old animals, but was significantly increased after AIS (**Fig. 3.1B**). Finally, the amount of the metabolite dihydrophenylglycine (DPHG), was not increased in 18- vs 3-month old animals but was significantly increased with AIS (**Fig. 3.1C**). As levels of the L-DOPA or DHPG are physiologically dependent on NE, we also analyzed the ratios of the catecholamines to the neurotransmitter in each group. The ratio of the precursor L-DOPA/NE was increased with AIS vs young controls, suggesting increased NE synthesis, but was not significantly changed in older mice. The ratio of the metabolite DPHG/NE was not changed in AIS vs young mice, suggesting a 1:1 matching of NE release to metabolism, while the ratio was decreased in old mice (**Fig. 3.1D**). These results indicate that there is sympathetic dysfunction and increased basal bone NE in older animals.

A progressive increase in cortical bone and marrow NE content in aging mice (1 to 12 months of age) was also detected via high sensitivity NE ELISA (**Fig. 3.1E and S3.1B**). Intrascapular brown adipose tissue (BAT) *Ucp1* expression, commonly used to quantify systemic SNS activity, did not increase with age, and instead peaked between 2 and 3 months of age (**Fig. 3.1F**). These results show that there is a progressive increase of skeletal tissue NE with age, and that the measurement of neurochemistry does not directly correlate with other measurements of systemic SNS activity.

In vivo skeletal NET activity decreases with age

Catecholamine release and regulation *in vivo* is a dynamic process. It can be attributed to either increased release, or decreased metabolism. In Chapter 1, NET was shown to be expressed and

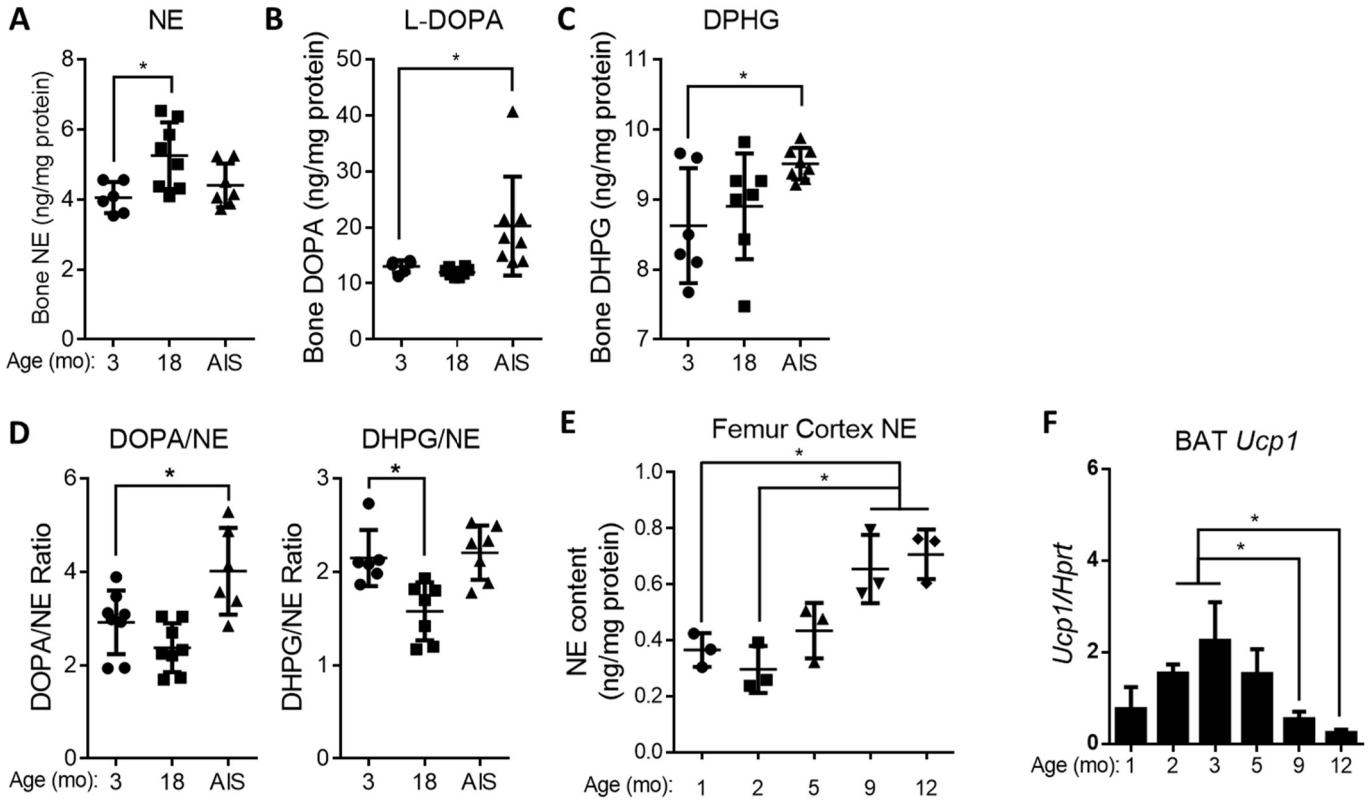

Figure 3.1 – Skeletal baseline NE content increases with age.

(**A – C**) Levels of norepinephrine (NE) (**A**), precursor L-DOPA (**B**), and metabolite DHPG (**C**) in whole tibiae from young (3 mo), old (18 mo), and young male mice subject to acute immobilization stress (AIS), measured by HPLC and normalized to tissue lysate protein content (n=6-8 per group).

(**D**) DOPA/NE and DHPG/NE ratios in whole tibia from young (3 mo), old (18 mo), and young male mice subject to AIS, measured by HPLC (n=6-8 per group).

(**E**) NE levels in femoral cortical tissues from mice of different ages, measured by ELISA and normalized to tissue lysate protein content (n = 3 per time point).

(**F**) Intrascapular brown adipose tissue (BAT) *Ucp1* expression in mice of different ages, normalized to reference gene *Hprt* (n = 4-6 per group).

All results are shown as mean +/- SD. Statistical analysis by one-way ANOVA, post-hoc Dunnett's statistical test for significance vs 3 month (**A – D**); or post-hoc Bonferroni statistical test for pair-wise significance (**F – G**), * $p<0.05$.

functional in both primary differentiated osteoblasts *in vitro*, as well as in skeletal tissues *in vivo.* Furthermore, there is increased levels of the sympathetic neurotransmitter NE in bone tissue of older animals. These data, along with the known catabolic action of β2AR stimulation on bone, led us to hypothesize that reduced NET activity upon aging may contribute to a rise in bone NE content and age-related bone loss. To address this hypothesis, we first aimed to determine whether NE uptake was deficient in skeletal tissue from older animals *in vivo*. Previously, we established a method to measure NET-mediated acute uptake of the radioligand [^{3}H]-NE in adult mice. Briefly, mice were pre-treated with NET blocker reboxetine (i.p. 20mg/kg BW) or sterile saline vehicle to ensure specificity by sufficient NET blockade, followed by administration of [^{3}H]-NE (10 μCi/kg BW) via tail-vein injection to avoid excess hepatic metabolism.

The radioligand was allowed to circulate for 10 minutes, and the animals were rapidly euthanized, and tibiae and femurs were harvested. Specific [^{3}H]-NE uptake via NET (AKA reboxetine-sensitive uptake) in cortical and marrow tissues was calculated as the difference between the vehicle-pretreated (total tissue uptake) and reboxetine-pretreated (non-NET uptake) groups, and normalized by tissue DNA content (as an indirect readout for cell number). Consistent with previous *in vitro* data showing NET expression in differentiated osteoblasts, acute [^{3}H]-NE specific uptake was significantly higher in the cortex (enriched in mature osteoblasts and osteocytes) than in the marrow of 3-month old mice (**Fig. 3.2A**). In addition, a significant reduction in specific [^{3}H]-NE uptake was observed in the bone marrow. These results confirm that older animals have decreased NE uptake in bone, and specifically in the osteocyte-rich cortical envelope.

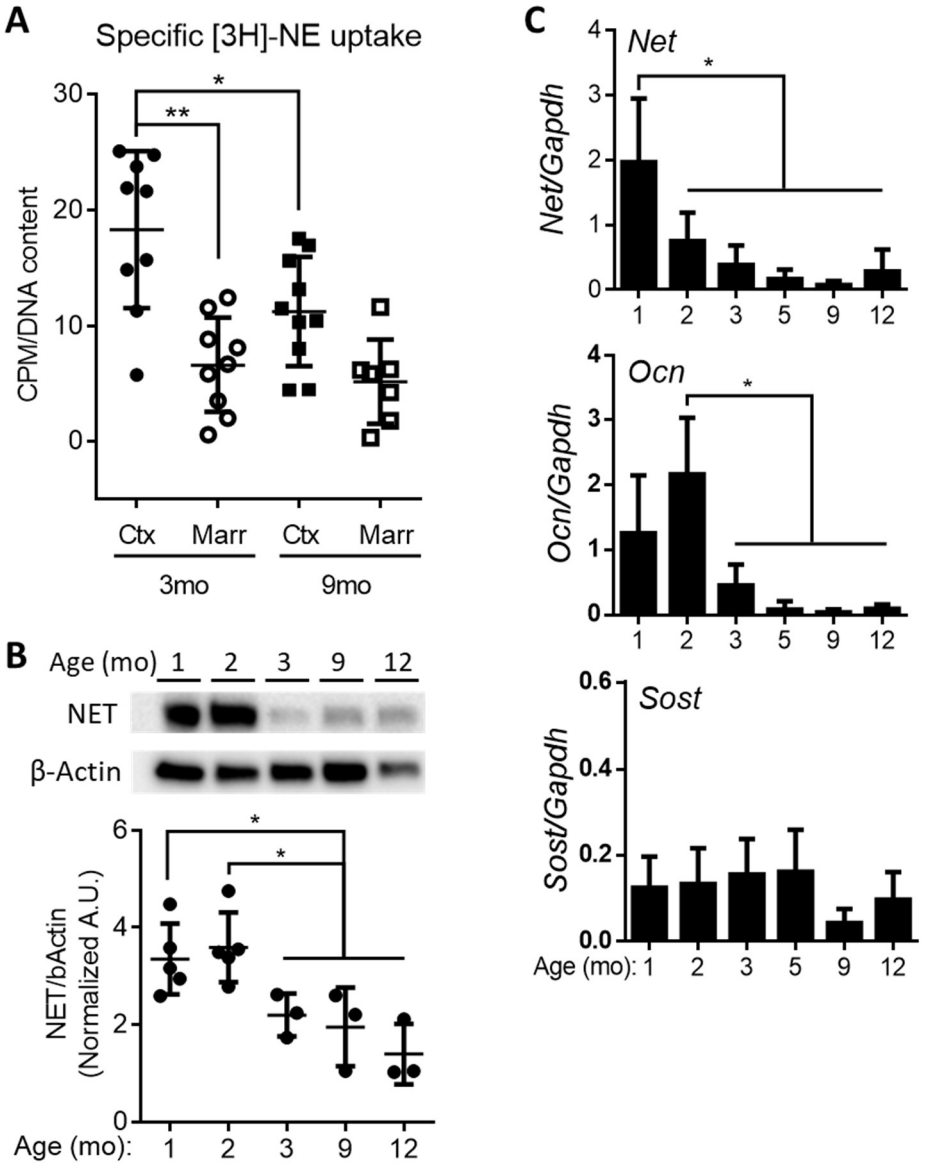

Figure 3.2 – Skeletal NET expression and uptake decreases in aged mice

(**A**) *In vivo* reboxetine-sensitive acute specific uptake of [^{3}H]-NE radioligand in the femoral cortex and marrow of 3- and 9-month old mice, normalized to lysate DNA content (n = 6-8 per group).
(**B**) Representative Western blot and quantification of NET expression in flushed femoral cortical tissues from mice of different ages, normalized to reference gene β-actin (n=3-5 per group).
(**C**) Expression of *Net*, *Ocn*, and *Sost* in flushed femur cortices from mice of different ages, normalized to reference gene *Gapdh* (n = 3-6 per group).
All results are shown as mean +/- SD. Statistical analysis by two-way (**A**) or one-way (**B – C**) ANOVA, post-hoc Bonferroni statistical test for pair-wise significance, * $p<0.05$, ** $p<0.01$.

NET expression in cortical bone decreases with aging

In vivo specific NE uptake by cortical bone tissues, whose cellularity is comprised of >90% osteocytes, and our previous detection of NET expression and uptake activity specifically in differentiated osteoblasts *in vitro* suggested that cortical osteocytes might be the main site of NET uptake *in vivo*. We therefore measured NET expression in flushed femoral cortices of WT C57BL6 mice from one month of age until 12 months of age, a time where bone loss is already significant in mice. NET protein expression peaked at two months of age, followed by a reduction significant by 3 months **(Fig 3.2B)**. A similar pattern of expression across ages was observed at the RNA level (**Fig. 3.2C and S3.1A**), suggesting that age impacts the transcription of *Net*, rather than protein content or stability, in cortical bone osteocytes. The osteocyte function marker *Sost* in these samples was not overtly affected by age, whereas the expression of the osteoblast function *Ocn* peaks at 2 months of age. Taken together, these results indicate that skeletal NET expression and function decreases with age.

Femoral artery sympathectomy (FASx) in rats

Sympathetic activation can lead to bone loss. However, it is unclear whether local SNS fiber NE or systemic adrenal epinephrine plays a major role in this process. To address whether the local sympathetic innervation to a single limb is necessary for SNS-mediated bone loss, we aimed to ablate the SNS in a limb unilaterally, thereby preserving the SNS innervation and function in both the adrenals and the contralateral limb. In order to achieve this, we first needed demonstrate whether femoral artery sympathectomy (FASx) was effective in removing SNS innervation from that limb. Borrowing from rodent renal artery sympathetic denervation protocols[168], we designed and performed FASx in Sprague-Dawley rats (**Fig. 3.3A and S3.2**). To determine ablation of sympathetic innervation of the bones downstream of the femoral artery, we compared tissues from the phenol (Phe) sympathectomized animals and sham controls. We also compared the Phe/Sham surgically treated (Sx) limb the

contralateral (Ctrl) limb of the same animal, as well as limbs from sham controls. Protein levels of the sympathetic marker TH in tissues, measured by Western blot band intensity and normalized to the reference protein β-actin, was not significantly decreased in sympathectomized limbs compared to either the contralateral or sham animals (**Fig. 3.4A**). Quantification of NE content via HPLC in tibial cortex tissue, normalize to tissue protein concentration, showed no significant difference between Phenol Sx limbs versus either the Ctrl limb or sham controls (**Fig. 3.4B**). Furthermore, to determine whether there was intra-animal difference in NE content between Sx and Ctrl limbs, we quantified tissue NE in femur and tibia cortex and marrow tissues by ELISA, and subtracted Ctrl values from Sx. There was no difference between phenol FASx or sham animals in the marrow or cortical tissue NE content in either femur or tibia (**Fig. 3.4C**). Finally, TH-immunopositive fibers were still present in the cortex (**Fig. 3.4D**) and marrow space – including periarterial nerve plexuses (**Fig. 3.4E and F**) – of the proximal femur of sympathectomized limbs. Taken together, these results indicate that the FASx procedure did not ablate SNS in the lower limb bones.

Discussion

High NE extracellular levels can be due to either increased synthesis and release, or decreased metabolism and uptake. During aging, increased cardiovascular NE spillover has been shown to be due to decreased NET capacity[172]. We show in this study a similar age-related change in the skeleton, with resting NE levels higher in bones from older mice. The normal levels of the catecholamine precursor L-DOPA and higher L-DOPA/NE ratio in bone from younger mice suggested the observed increase in bone NE was unlikely from increased synthesis, and the reduction in acute *in vivo* [^{3}H]-NE uptake in the bone of aged animals further supports a deficit in reuptake function. These new *in vivo* results, along with the

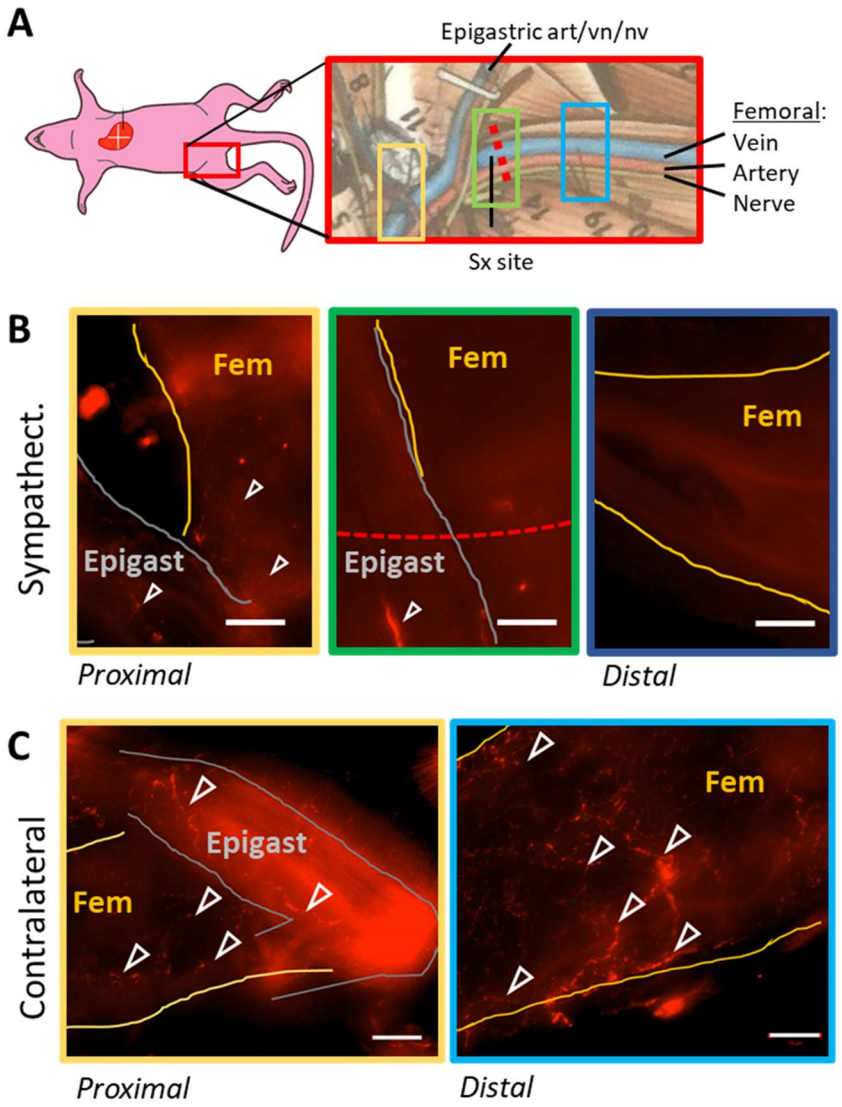

Figure 3.3 – Rat femoral artery sympathectomy (FASx) procedure and TH immunofluorescence confirmation
(**A**) Diagram of sympathectomy with landmarks. Dotted red line represents site of sympathectomy (Sx). Inset diagram adapted from Popesko, Rajotva and Horak. *A Colour Atlas of Anatomy of Small Laboratory Animals*. 2nd ed.
(**B – C**) Representative images of anti-TH immunofluorescence of proximal (yellow box), middle (green box) and distal portions (blue box) whole rat artery from sympathectomized (**B**) and contralateral (**C**) control leg. Outlines of the femoral (yellow line) and epigastric (gray line) arteries, TH-immunopositive fibers (arrowheads), and site of Sx thread (dotted black line) are shown. Scale bars = 100µm.

Figure 3.4 – Rat femoral artery sympathectomy (FASx) does not ablate tibia or femur SNS

(**A**) Representative Western blot and quantification of TH in tibial marrow and cortex from surgically treated (Sx) contralateral (Ctrl) limbs in Sham or Phenol (Phe) FASx rats, normalized to reference gene β-actin (n=4-5 per group).

(**B**) NE levels in tibial cortex from Sx or Ctrl limbs in Sham or Phenol FASx rats, measured by HPLC and normalized to tissue lysate protein concentration (n=4-5 per group).

(**C**) Relative changes in NE levels, measured by ELISA in tibia and femur marrow and cortex of Sham or Phenol FASx rats. Normalized to tissue lysate protein concentration (n=4 per group).

(**D – F**) Representative immunofluorescence images of femur cortex (**D**) and marrow vessel (**E**) from phenol-Sx rats. Tyrosine hydroxylase (TH) immunopositive fibers (red, closed arrowheads) are present close to vascular structures in cortical vascular canals (**D**) and around medullary arterioles (**E**). Negative IgG primary antibody control (**E** and **F**, dotted open arrowheads) represents background immunofluorescence. Images are representative of sections from 3 animals for each treatment.

All results are shown as mean +/- SD. Statistical analysis by two-way ANOVA, with significance taken at $p < 0.05$.

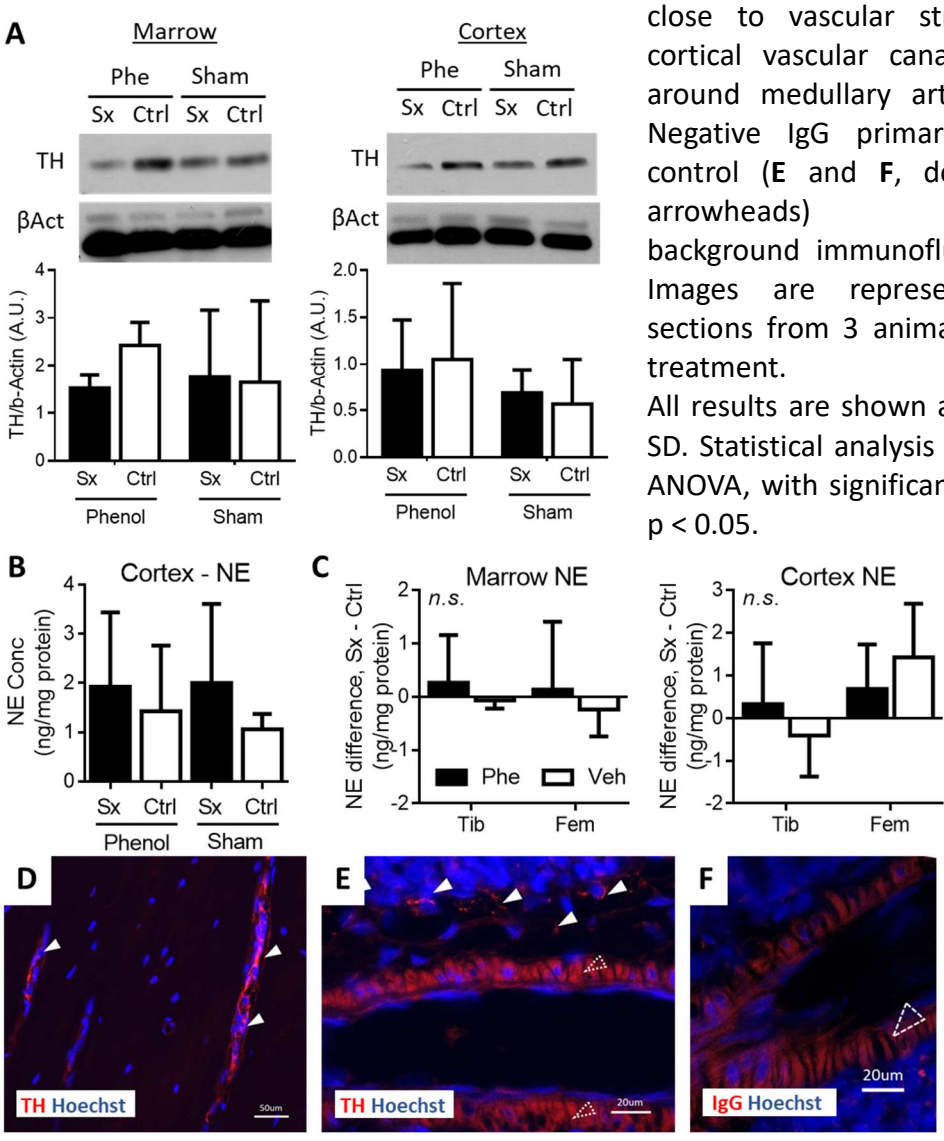

expression of NE catabolic enzymes in osteocyte cultures, support the hypothesis that osteocytes function as a catabolic sink for NE in bone, and that this capacity is diminished with age. However, at this whole-tissue resolution, it was not possible to determine whether the decrease in NET expression and function with age was caused by the natural decrease in osteocyte density with age[125] or by an intrinsic cell-autonomous reduction in *Net* expression in "old" osteocytes.

The decreased [^{3}H]-NE uptake in the cortex of 9- vs 3-month old animals (**Fig. 3.2A**) could be attributed to the competition of NET-binding sites by the high endogenous NE in older animals (**Fig. 3.1**). However, the lower NET protein and RNA in these tissues suggests that the functional decrease stems from decreased expression. Furthermore, the concentrations used in *in vivo* radioligand uptake experiments were selected from experiments in NE uptake in other tissues (e.g. heart)[96,173,174], and represent acute high-affinity uptake that is NET sensitive (as opposed to saturating levels of radioligand). Controlling for these factors may theoretically be possible – either be systemically depleting NE prior to acute [^{3}H]-NE uptake, or by measure uptake of isolated *ex vivo* washed tissues, much like in brain neurotransmitter uptake experiments[82,175]. While these two approaches would be "purer" in modeling tissue neurochemistry, the perturbations to the endogenous SNS regulatory system or tissue integrity may introduce too many variables for reliable interpretation. Additionally, it is possible that osteocytic NET is divided between surface functional and intracellular sequestered NET. It is also possible that osteoblast/osteocyte NET is sequestered away from the cell surface, and that certain physiologic, pathologic, or external pharmacologic stimuli may alter this surface expression without requiring gene expression changes. This surface vs. intracellular distinction is cannot be addressed by whole-tissue gene and protein quantification. However, measurement of binding of radio-labeled small molecule NET antagonist ligands (e.g. [^{3}H]-nisoxetine)[173,176,177] would provide a direct measurement of surface NET.

Decreased NET protein and RNA expression during aging *in vivo* is consistent with the functional data (**Fig. 3.2**). To definitively demonstrate that pathophysiologic NET deficiency during aging leads to

decreased uptake, additional experiments over-activating NET will be necessary. This can be achieved either through pharmacologic upregulation of NET expression, genetic over-expression of NET in osteocytes, or pharmacologic potentiators of NET function (of which none are currently known). There are several reports of pharmacologic agents upregulating NET expression such as by corticosterone[178] or PKC inhibitors in neuronal cell line[146,179], or the HDAC inhibitor Vorinostat in *in vivo* models of pheochromocytoma[149,180]. However, prior to these studies, it is necessary to demonstrate that NET in osteoblasts *in vitro* or in bone tissue *in vivo* is sequestered intracellularly. This could be achieved by either high-resolution microscopy and immunofluorescence for NET in these cells, or by indirect measurements such as cell-surface ELISA of NET on surface vs. permeabilized cells.

Our results show that chemical unilateral femoral artery sympathectomy does not ablate sympathetic innervation from the bones of a limb (**Fig. 3.3** and **3.4**). Hilton's law, which states that the nerve supply to a region of skin or muscle also supplies the underlying bone and joint, arose from surgical observations and knowledge of embryology. In general, dermatomal nerve patterns are shared between muscle, bone, and overlying skin[164]. However, this rule is used in application of afferent sensory nerves, and is not generally applied to autonomic nerves. It is possible there exists alternative routes of SNS innervation of the tibia and femur. It is also possible that the 7 days post FASx was sufficient for re-innervation of the tissue by the SNS. Previous global chemical sympathectomy experiments in rabbits demonstrated regeneration of SNS fibers within the bone after 2 weeks[181] despite complete loss of fiber immunofluorescence staining 3 days post-systemic sympathectomy. It is possible that these rats experienced similar regeneration, and/or auxiliary paths of innervation compensated for the initial FASx-mediated loss. To address these questions, several time points post FASx would be needed, and methods to monitor leg SNS activity *in vivo* – such as recurrent tibial nerve activity[128] or skin temperature changes to local cold challenge – could be employed.

Although post-synaptic pharmacological βAR stimulation induced bone loss in mice[88,182], neither short-term chronic pharmacologic blockade of NET alone (by the antagonist reboxetine), nor increased endogenous NE release (by a chronic immobilization stress protocol) impacted bone mass in young mice. However, chronic stress led to a significant loss of bone mass when combined with NET blockade with reboxetine [83]. These results suggested that NET protects the skeleton from the catabolic action of NE released from activated sympathetic fibers, and that conditions associated with impaired NET function and increased SNS outflow might lead to bone loss. In order to demonstrate that skeletal NET does indeed uptake physiologic NE, *in vivo* experiments measuring bone tissue NE, L-DOPA, or DPHG in resting or AIS-stimulated aged mice are necessary – similar to experiments done in young mice presented in Chapter 1 (**Fig. 2.4**). Results from these studies would verify whether the already elevated basal SNS activity in bone from older animals is capable of further excitation. To further probe beyond the resting steady-state SNS physiology, future studies in aging animals should also include reboxetine pre-treatment, in order to eliminate the influence of NET. Findings from these proposed future experiments would provide evidence as to whether the low skeletal NET expression in aged animals is capable of any endogenous NE metabolism via uptake. These data support the model whereby NE uptake by NET in cortical osteocytes buffers endogenous NE released by sympathetic nerve fibers, and suggest that failure of this homeostatic system might contribute to age-related bone loss, although this latter point will need to be addressed by loss-of-function experiments.

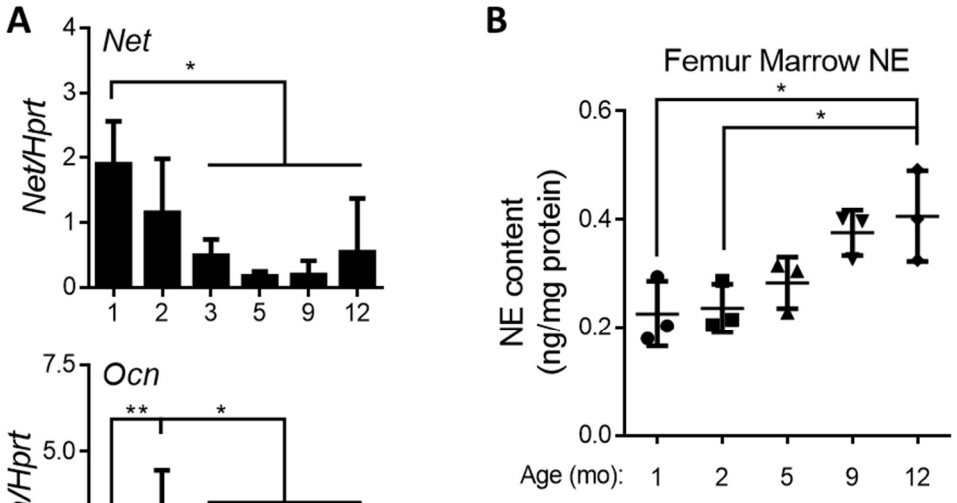

Figure S3.1 – Skeletal *Net* expression decreases with age

(**A**) Expression of *Net*, *Ocn*, and *Sost* in flushed femur cortices from mice of different ages, normalized to reference gene *Hprt* (n = 3-6 per group).

(**B**) NE levels in femoral marrow tissues from mice of different ages, measured by ELISA and normalized to tissue lysate protein content (n = 3 per time point).

All results are shown as mean +/- SD. Statistical analysis by two-way ANOVA, post-hoc Bonferroni statistical test for pair-wise significance, * $p<0.05$.

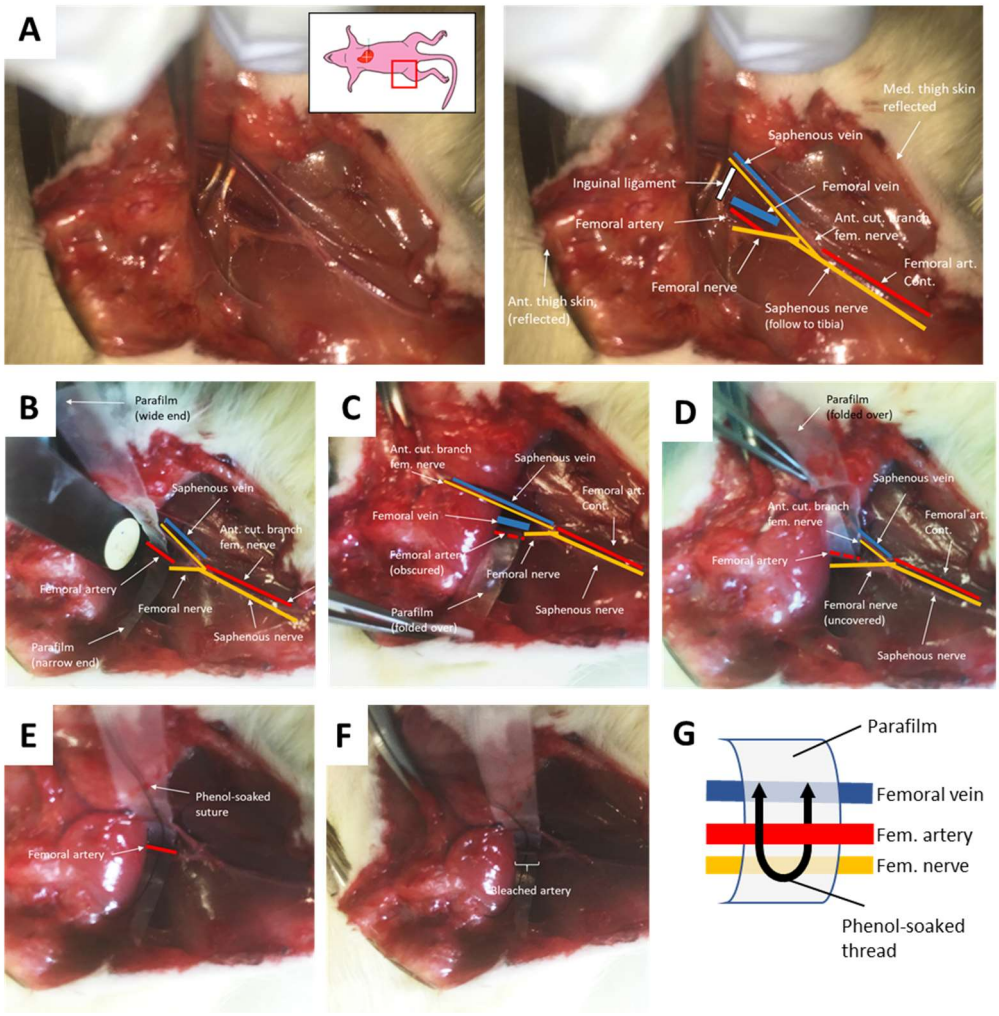

Figure S3.2 – Rat femoral artery sympathectomy surgery procedure images
Legend: red line – artery; blue line – vein; yellow line – nerve; white line – inguinal ligment
(**A**) Right medial thigh inguinal region (inset) with labeled structures (right). Skin and underlying fascia were removed and reflected to expose inguinal triangle. The femoral artery and nerve were separated from their common sheath (not visible).
(**B - F**) Stepwise procedure for femoral artery sympathectomy. A sterilized thin paraffin strip was passed around femoral artery to isolate it from surrounding structures (**B – D**). To chemically ablate peri-arterial nerves, a thread soaked with 50% phenol in ETOH was threaded around the femoral artery, on top of the paraffin strip (**E**), and moved around the artery to ensure sufficient phenol contact. The resulting bleached artery (**F**) indicates successful phenol treatment of the tissue.
(**G**) Schematic diagram of FASx procedure.

Chapter 4. *In situ* NET Expression Bone Innervation

Introduction

As an endocrine organ, the skeleton can be expected to be both the target and the source of endocrine, paracrine, and neuronal signals that integrate its functions with other tissues and organs. Multiple experimental evidence in mice and humans suggest that the sympathetic nervous system (SNS), a branch of the autonomic nervous system responsible for maintaining the homeostasis of many tissues, regulates skeletal homeostasis[6,88,89]. Sympathetic nerve fibers indeed were shown to innervate skeletal tissues[90–93], and osteoblasts express receptors for norepinephrine (NE), the neurotransmitter released by these sympathetic nerves, with the β2-adrenergic receptor (β2AR) being the predominant receptor expressed in this lineage[88]. The current model of how peripheral sympathetic nerves impact bone remodeling includes the release of NE, which acts on osteoblastic β2AR to promote bone loss through RANKL-mediated activation of osteoclasts[88,89] and inhibition of osteoblast proliferation via *Clock* genes[94]. This model is derived from genetic mouse models as well as pharmacological approaches targeting mainly post-synaptic βARs.

From these studies, significant progress has been made in elucidating the receptors, molecules, and cells responsible for this process. However, further understanding of the mechanisms involved are hampered by the limited data describing the neuroanatomy of bone innervation during development, in adults, or in response to skeletal pathologies. An obligate first step to progress further is thus to precisely map, anatomically first, the innervation of the skeleton by autonomic nerves, at both tissue and cell levels. At the tissue level, we need better understanding of the distribution of sympathetic nerve fibers near bone structures. This anatomic data will help infer the function of SNS on bone elements. At the cellular level, we need better understanding of where sympathetic fibers and the NE reuptake machinery NET are located within bone tissues. These data will help provide an anatomical

perspective through which we can more appropriately interpret the pharmacologic and genetic finding of SNS on bone.

Visualizing sympathetic fibers in bone

Previous studies investigating sympathetic fibers in bone show that they are rare in bone tissues[92,163,183]. Traditional methods using fluorescent protein reporters and/or immunofluorescence on thin histological sections yield high cellular resolution, but cannot easily provide a whole-organ survey of innervation of bone. Numerous neurochemical and nerve retrograde tracing studies have confirmed the existence of anatomical sympathetic innervation of bone. However, these methods have also failed in providing high resolution anatomical maps of SNS nerves. In the past decade, a new technique called CLARITY was invented to study innervation in the brain at a high resolution[184,185]. This method has since been adapted to numerous other organ systems such as the heart, kidney, and even bone [186–188]. Furthermore, CLARITY has been used to specifically study sympathetic innervation of adipose tissue. Dye-based delineation of structures (e.g. lineage-specific β-galactosidase expression) are ill-suited for this imaging method, since it is highly dependent on washing the tissue with detergents and solvents. However, mice with endogenously expressed fluorescent proteins are compatible with the CLARITY method[186,189]. Thus, transgenic mice driving Cre activity in sympathetic neurons, crossed with reporter mice expressing a fluorescent reporter upon Cre expression, can be used to delineate sympathetic neuronal structures within bone. These genetic tools can be used with CLARITY method and whole-mount microscopy techniques to provide a high resolution 3-dimensional mapping of autonomic nerves in the skeleton.

Results

NET is expressed in cortical osteocytes

Our current paradigm involves NET expressed on mature osteoblasts/osteocytes involved in NE uptake *in vivo.* In Chapter 2, we presented results where mature *in vitro* differentiated BMSCs and tibial cortex (enriched in osteocytes) express *Net* and have reboxetine-sensitive uptake. We have previously detected NET tissue expression in post-natal day 2 tibiae[83]. However, osteoblast-lineage NET expression in the adult skeleton has yet to be demonstrated. To confirm osteocytic NET expression *in situ* and possible presence of SNS nerves in the osteocytic network, we aimed to use both genetic reporter mice and immunofluorescence and imaging techniques to detect NET on bone matrix-embedded osteocytes. Using immunofluorescence, we detected NET immunofluorescence (NET-IF) in TH-immunopositive (TH-IF) fibers in the tibial trabecular zone of adult mice, close to bone surfaces (**Fig. 4.1A**), indicative of TH^+ SNS fibers that co-stain for both NET and TH at their terminals or along the nerves. Using mice expressing the tdTomato fluorescent protein in sympathetic Th^+ neurons (*ROSA26*-tdTomato; *Th-Cre*), we also detected NET immunofluorescence co-incident with TH-driven tdTomato fluorescence (TH-Tom) (**Fig. 4.1B**). However, there was also background fluorescence signal in vessel erythrocytes (open arrowheads), and bone surface-lining osteoblasts in sections with NET-IF and IgG primary antibody negative control (asterisks, **Fig. 4.1C**).

We also detected NET immunostaining in matrix embedded osteocytes in the tibial cortex of these mice (**Fig. 4.2A**), but not in trabeculae (**Fig. 4.2B**) or in sections incubated with mouse IgG isotype negative control (**Fig. 4.2C**). NET expression was not uniform across all tibial cortical regions. Quantified osteocytic NET expression was the highest in the cortical region adjacent to the secondary spongiosa and the diaphysis, while relatively sparse around the primary spongiosa/perichondrium (**Fig. 4.2D**).

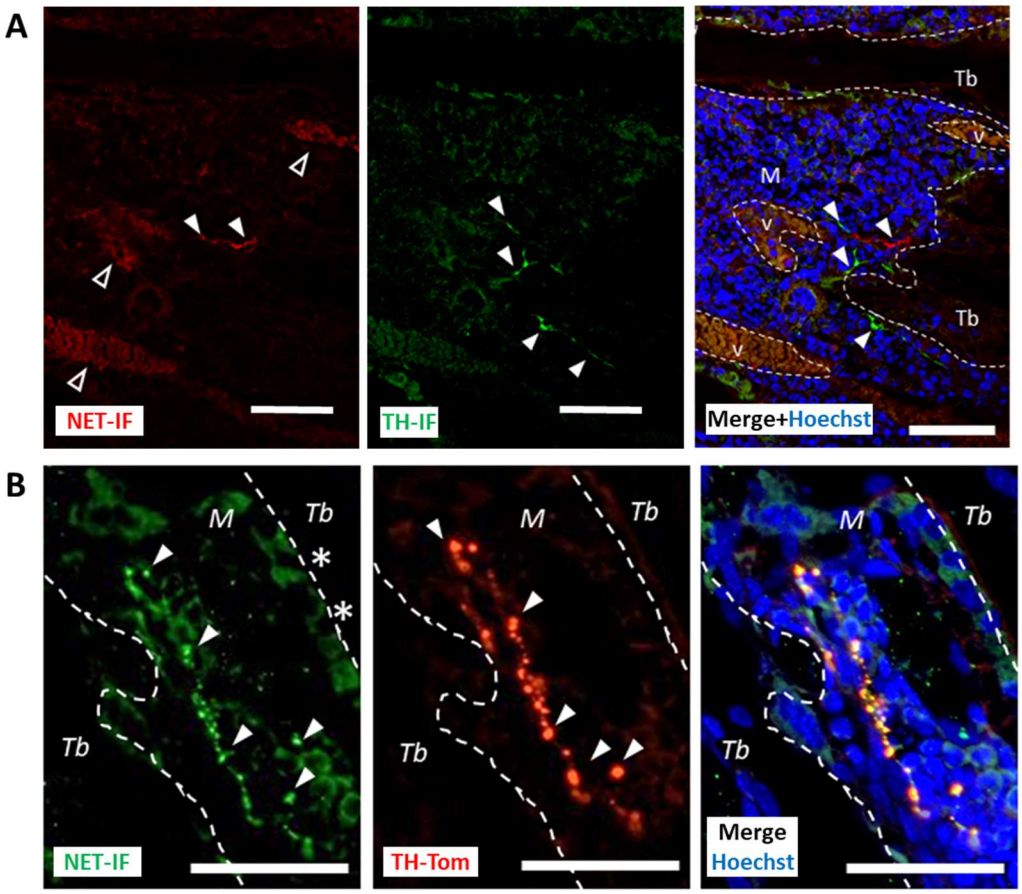

Figure 4.1 – NET immunofluorescence and sympathetic nerves in bone marrow

Legend: vessel (v), trabeculae (*Tb*), cortex (*Ctx*), marrow (*M*), periosteum (*PO*), *IF*: immunofluorescence, *DIC*: Differential interference contrast microscopy.

(**A**) Immunofluorescence images of fibers with NET (red) and TH (green)-immunostaining in tibial trabecular zone (closed arrowheads). Non-specific background fluorescence is visible in blood representative of 2 sections from 3 animals. Scale bar 50um.

(**B**) NET immunofluorescence (green, closed arrowheads) colocalization with TH-Tomato expression (red) in tibial diaphyseal cortex sections. Weaker signal is observed in cuboidal cells apposed to trabeculae (asterisks). Images are representative of 2 sections from 3 animals. Scale bar 50um.

(**C**) IgG primary antibody negative control and TH-Tomato expression (red) in tibal diaphyseal cortex section. Weaker signal is observed in cuboidal cells apposed to trabeculae (asterisks). Images are representative of 2 sections from 3 animals. Scale bar 50um.

Although background fluorescence signal was observed in vessels and bone-lining cells, several observations support the specificity of the NET staining. First, staining was observed in the peri-cellular area of TH-positive adrenal medullary chromaffin cells, which are catecholaminergic neuroendocrine cells known to express NET at their surface (**Fig. S4.1A**, positive control). Second, replacement of the primary antibody against NET by a non-immune IgG did not label any neuronal structure nor osteocytes (**Fig. 4.1C** and **4.2C**), although some signal was observed in blood vessel erythrocytes (**Fig. 4.1A,** open arrow) and in the periosteum (**Fig. 4.2A** and **C**) in both anti-NET and mouse IgG isotype groups. This similar pattern of expression between the anti-NET and mouse IgG isotype groups strongly suggests that this erythrocyte and periosteal staining is indeed background signal. The analysis of mice deficient for *Net* will be necessary to confirm this, however, the observation that NET immunoreactivity disappeared, along with TH immunoreactivity, in bone marrow neurons (but not osteocytes) in tibial sections from animals chemically sympathectomized with 6OHDA (**Fig. S4.1B – E**) further supports specificity of the anti-NET antibody.

TH^+ fibers and osteocytic NET expressed in human bone biopsies

It is assumed that murine animal models of SNS-bone interaction are an accurate model of human physiology. To confirm this, we performed immunofluorescence histology on a human proximal tibia bone biopsy. We were able to detect TH^+ sympathetic fibers in the Haversian canals (**Fig. 4.3A**) and along the endosteal surfaces (**Fig. 4.3B**) in these sections. NET was also detected in cortical osteocytes (**Fig. 4.3C**) although it was not co-localized with in TH^+ fibers. No TH^+ fibers or NET^+ osteocytes were observed in IgG isotype negative controls. These results represent preliminary evidence that the human skeleton is innervated by the SNS, and that human cortical osteocytes express NET, but will need additional samples to verify these findings.

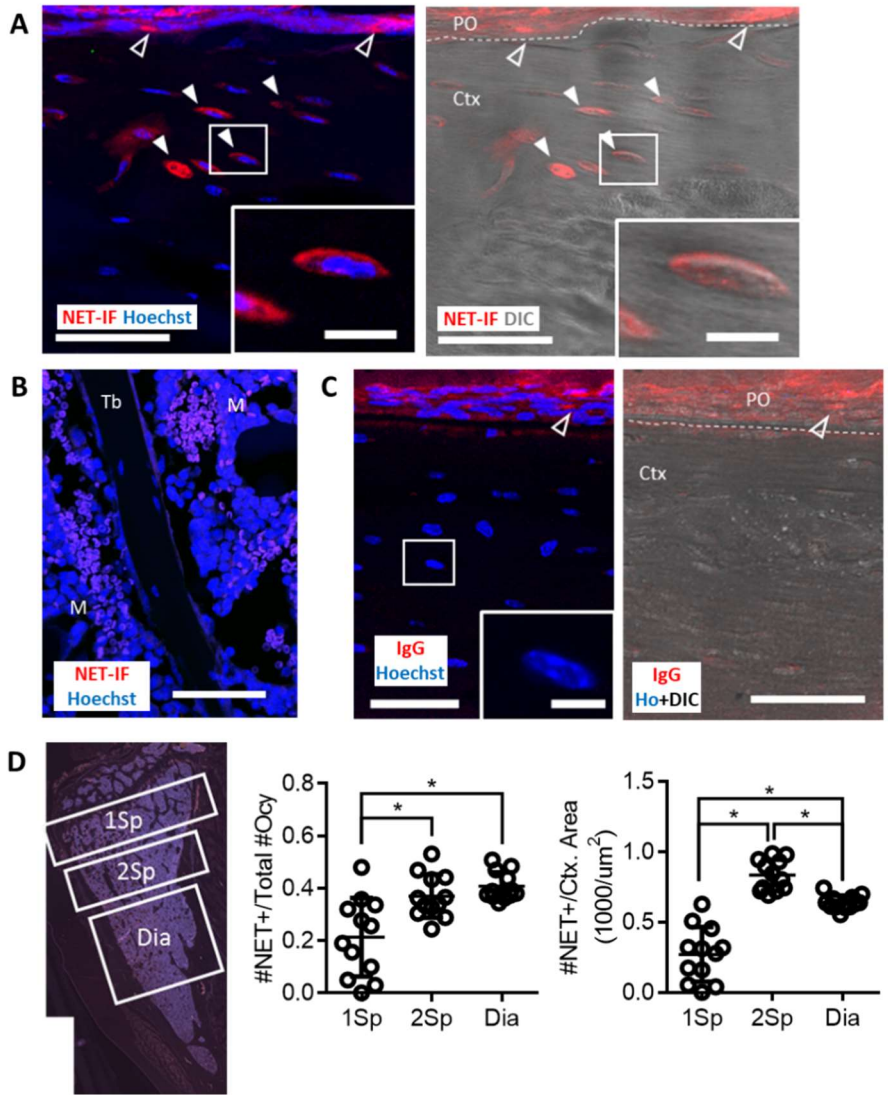

Figure 4.2 – NET immunofluorescence in osteocytes

Legend: vessel (v), trabeculae (*Tb*), cortex (*Ctx*), marrow (*M*), periosteum (*PO*), *IF*: immunofluorescence, *DIC*: Differential interference contrast microscopy.

(**A**) Max. intensity projection of NET-immunofluorescence (red, closed arrowheads, left images) in tibial diaphyseal cortex sections. Non-specific background fluorescence is observable in the periosteum (open arrowheads). Images representative of 2 sections from 3 animals, projections from 9 confocal optical sections through 10um depth. Scale bar 50um. Inset: magnified osteocytes, scale bar 20um.

(**B**) NET-immunofluorescence not found in max. intensity projection of tibial trabecular osteocytes. Images representative of 2 sections from 3 animals, projections from 9 confocal optical sections through 10um depth. Scale bar 50um.

(**C**) Max. intensity projection of IgG primary antibody negative control in tibial diaphyseal cortex sections. Non-specific background fluorescence is observable in the periosteum (open arrowheads). Images representative of 2 sections from 3 animals, projections from 9 confocal optical sections through 10um depth. Scale bar 50um. Inset: magnified matrix-embedded osteocytes, scale bar 20um.

(**D**) Density of NET^{+} osteocytes per total number of osteocytes or total cortex area per region in primary spongiosa (1Sp), secondary spongiosa (2Sp), or diaphysis (Dia). (n= 4 animals, 3 sections per animal).

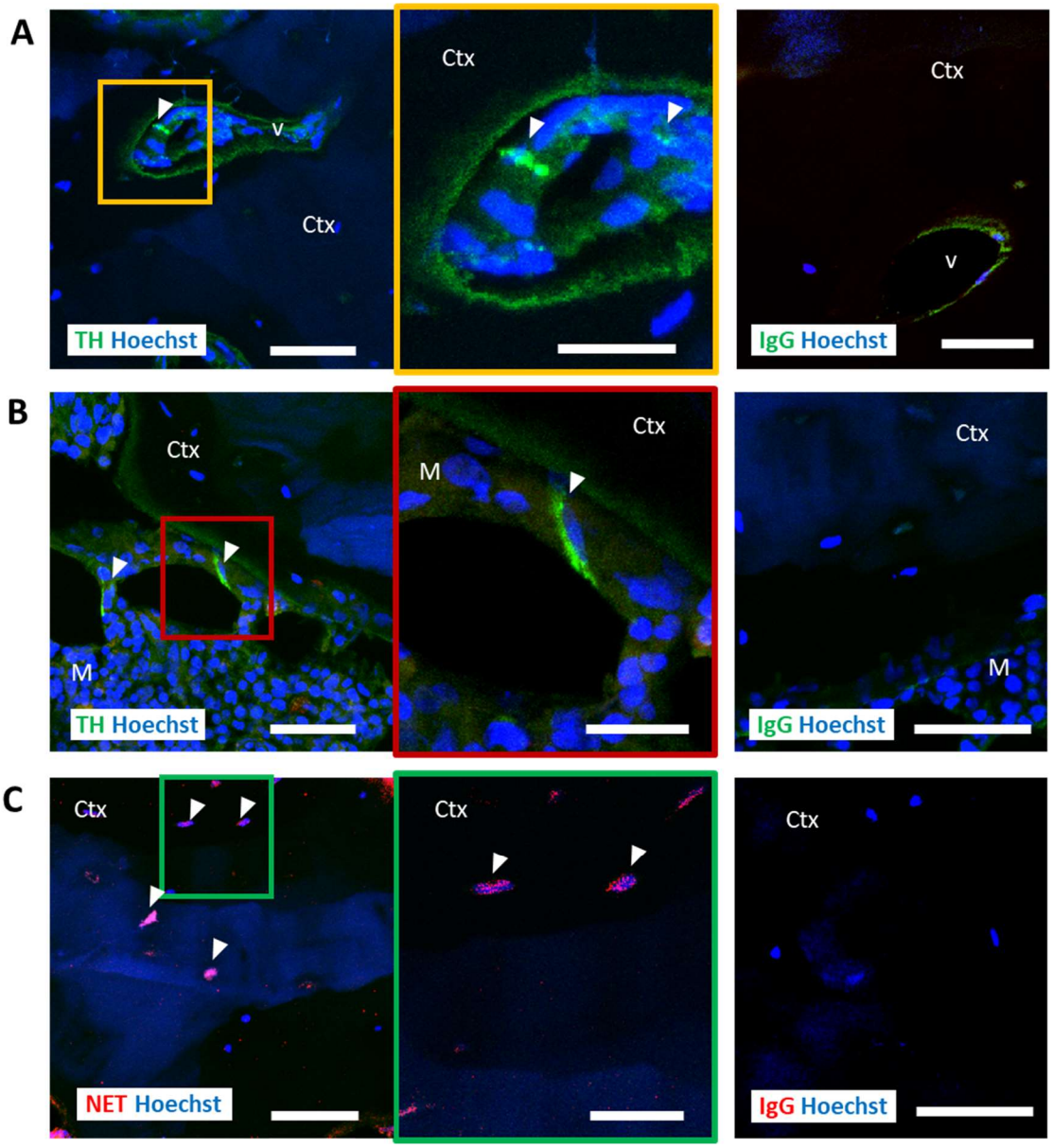

Figure 4.3 – NET and TH immunofluorescence in human bone
Legend: vessel (v), trabeculae (*Tb*), cortex (*Ctx*), marrow (*M*), periosteum (*PO*), *IF*: immunofluorescence
(**A - B**) Immunofluorescence images of fibers TH-immunopositive fibers (green, closed arrowheads) and of IgG primary antibody negative controls (right) in bone biopsy samples from human patients. Images are representative of 3 sections from a patient biopsy. TH-fibers within intracortical Haversian canal (**A**) at endosteal surface of bone (**B**). Scale bar 50um (left); magnified (colored box inset, middle) scale bar 20um.
(**C**)) Immunofluorescence images of NET-immunopositive cells (red, closed arrowheads) and of IgG primary antibody negative controls (right) in bone biopsy samples from human patients. Images are representative of 3 sections from a patient biopsy. Scale bar 50um (left); magnified (colored box inset, middle) scale bar 20um.

Visualizing distribution of sympathetic nerves in long bones

Previous studies have documented the presence of TH^+ fibers in bone[92,159,163,190], but did not provide a precise anatomical map of sympathetic fiber densities in bone. A question raised by the finding of NE uptake activity in cortical bone is whether SNS fibers were located close to osteocytes. To investigate the distribution of sympathetic tyrosine hydroxylase (TH+) nerve fibers in long bones, we generated transgenic reporter mice overexpressing a tdTomato fluorescent reporter protein in TH-Cre+ cells (TH-Tomato)[191]. In order to visualize long TH^+ fibers in and around the cortical envelop volume, we applied the bone CLARITY optical clearing and whole-mount confocal imaging techniques[186,192] to clear whole femurs hemi-sectioned longitudinally (see Materials and Methods and **Fig. S4.2**). In order to differentiate tissues, Hoechst stain (blue) and tissue autofluorescence (false color gray) were used to approximate location of the TH-Tomato signal (red). Using this approach, SNS fibers were grossly observed in the diaphyseal region in 3D reconstruction tissue and top-down maximum intensity projection (MIP) of the tissues (**Fig. 4.4A** – **B**). To determine the tissue-level location of SNS fibers, digital sections of the entire tissue image were generated. TH-$Tomato^+$ signals were observed in the periosteum area, as previously reported[92] , but also within compact cortical bone (**Fig. 4.5A – B**). Digital coronal sections of the diaphysis at all levels of cortex studied confirmed TH-tomato signals within the compact bone cortical envelope (**Fig. 4.5C**).

Quantification of sympathetic nerve fibers in bone compartments

Using the whole-mount bone CLARITY and light sheet imaging technique allows quantification of nerves in discrete bone compartments (e.g. cortex vs. medullary marrow). In order to differentiate bone matrix from marrow and other structures, bone hemisections were optically cleared and counterstained

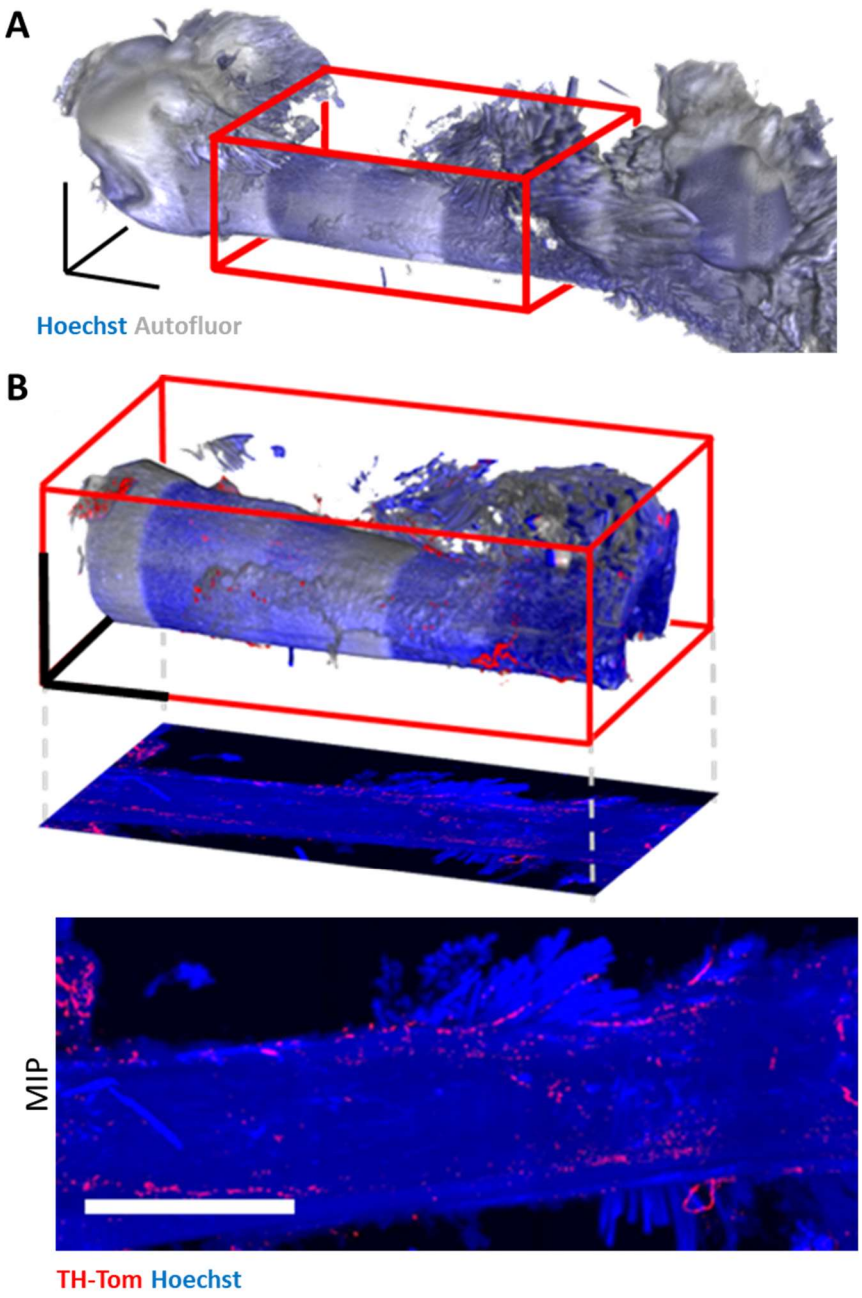

Figure 4.4 – Whole-mount imaging of TH$^+$ sympathetic nerves in bone
(**A**) Representative 3D reconstruction of femur hemisection from light sheet imaging of entire tissue. Diaphysis region is highlighted (red box). Image shows Hoechst fluorescent staining (blue) and FITC-autofluorescence (false color gray). Scale axis bars 500um.
(**B**) Boxed diaphysis region from 3D femur hemisection reconstruction, and top-down maximum intensity projection (MIP) of boxed region. Tissue imaged from Hoechst (blue) and FITC-autofluorescence (false color gray), and sympathetic nerves by TH-tdTomato fibers (TH-Tom, red). Scale axis bars 500um.

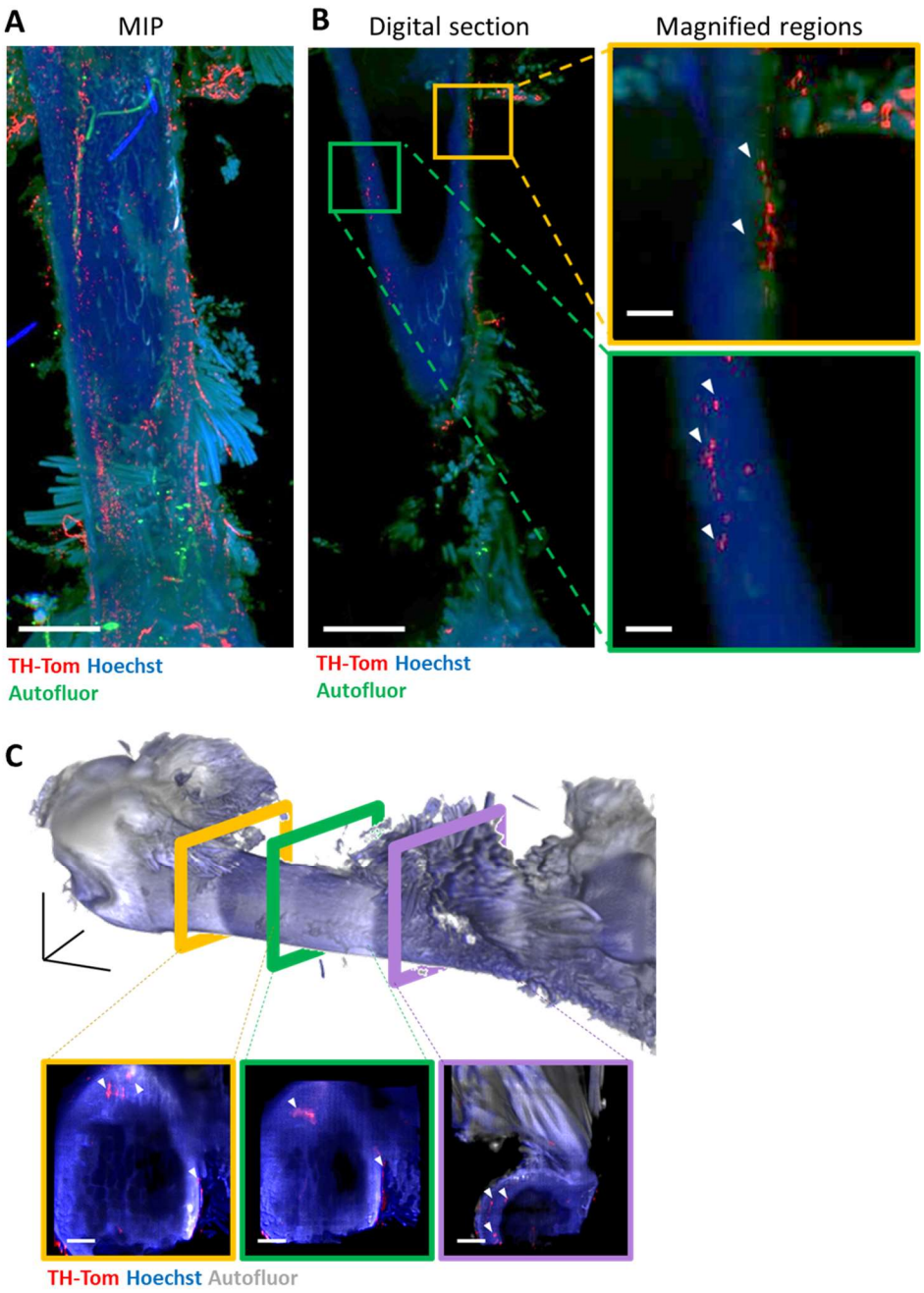

Figure 4.5 – TH$^+$ fibers in cortex sections of 3D reconstructed femurs
(**A**) Top-down maximum intensity projection (MIP) of boxed diaphysis region from Fig. 3.2 showing TH-Tomato signal (red), Hoechst fluorescent staining (blue), and FITC-autofluorescence (green).
(**B**) Top-down MIP digital section of 10 Z-frames (36um) of the tissue in (**A**). Scale bars 400um. Highlighted regions (yellow and green boxes) shown in magnified panels, scale bar 100um.
(**C**) Coronal digital sections, indicated by colored frames (yellow, green, and purple) on 3D reconstructed femur hemisection. Image constructed from Hoechst fluorescent staining (blue) and FITC autofluorescence (false color gray). Scale axis bars 500um. Digital tissue cross-sections 50um thick, show red TH-Tom fluorescent signal located within cortical/periosteal tissues (arrowheads), scale bar 100um. All images are representative of femurs hemisections from 3 animals.

with both the Hoechst nuclear stain (blue), as well as a fluorescently conjugated phalloidin actin stain (false color purple). Bone matrix tissue was identified as regions of Hoescht^{Hi}/phalloidin^{Hi}. Conversely, marrow tissues were identified as Hoescht^{Hi}/phalloidin^{Lo} based on higher marrow cell density[193] (**Fig. 4.6A**).

In order to better visualize and quantify the anatomical position of TH^{+} fibers relative to the compact bone stroma within a 3D environment, a semi-automated method was established to identify and label nerves, bone elements and their respective positions, based on discretization of fluorescent intensities (see Materials and Methods). In brief, we used Imaris software to convert TH fluorescence intensity into fibers, resulting in a discrete filament network that follows the TH^{+} intensity (**Fig. 4.6B**). Compact bone stroma was visualized by converting Phalloidin-staining intensities into a solid surface object with discrete boundary, volume and surface (**Fig. 4.6C**). To identify and analyze nerve fibers that penetrate the cortical bone, TH^{+} filaments were converted into spots (**Fig. 4.6D** shows center spots only), and the overlap with Phalloidin^{+} cortical surface object was used to segregate the TH spots into internal red "cortical" or yellow "external periosteal or medullary" spots (**Fig. 4.6E**). Medullary and periosteal spots were manually differentiated by their location relative to cortex. Finally, the volume of each segregated spot subset and total spots were quantified by the Imaris software, indicating total TH innervation of tissues, and the ratio of each tissue's innervation vs. the total innervation (**Fig. 4.6F**). Using this method, nearly 90% of the density of TH+ fibers was colocalized within the periosteum and cortical bone envelops at the level of the secondary spongiosa and diaphysis of the femur.

Discussion

Expression of NET in bone tissues was previously described only in trabecular osteoblasts of postnatal

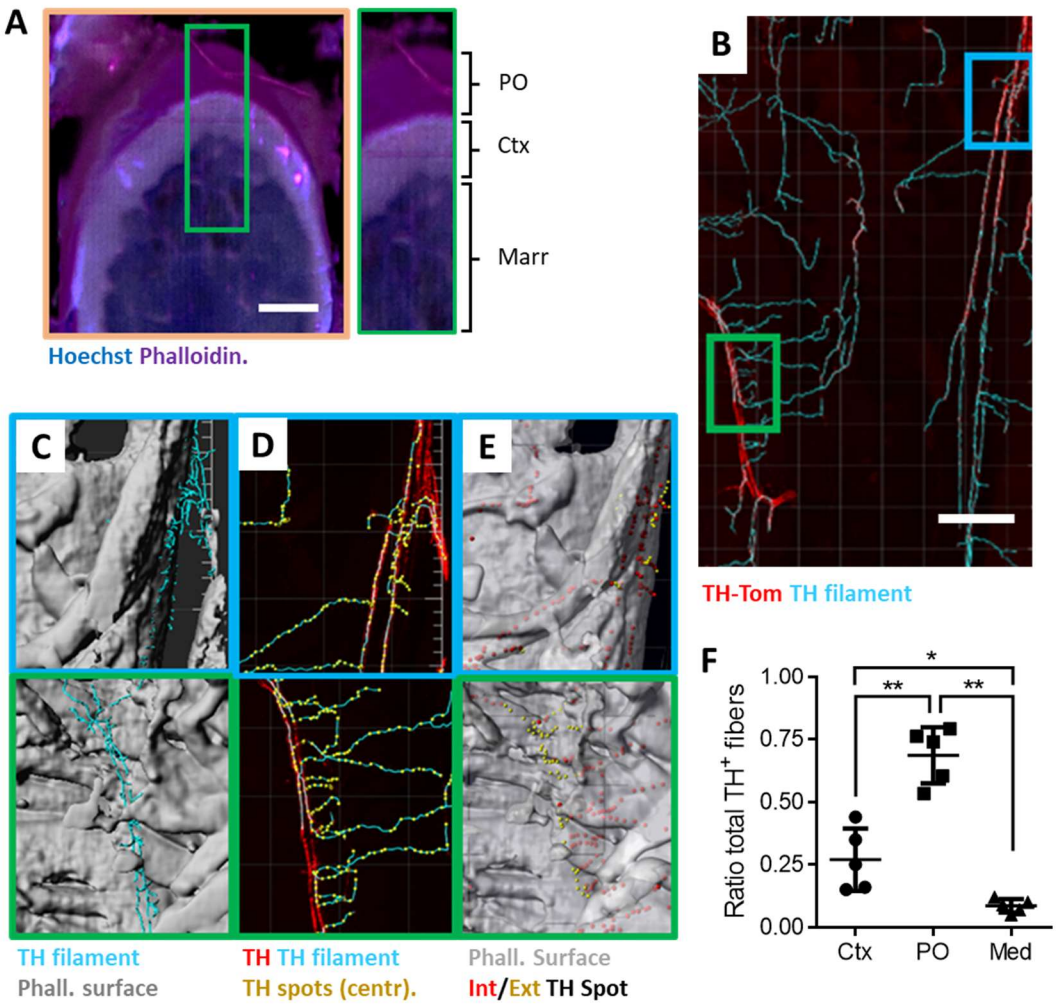

Figure 4.6 – Semi-automated identification and quantification of SNS fibers in cortical bone
(**A**) Cross-sectional view of Hoechst (blue) and Phalloidin (false-colored red) stained cortex around secondary spongiosa, with periosteum (PO), cortex (Ctx) and marrow (Marr) delineated. Scale bar 100um.
(**B**) Representative image of filament approximation (cyan) of TH+ fibers (red), with highlighted regions (blue and green boxes) magnified. Scale bar 300um.
(**C**) Phalloidin+ surface reconstruction (grey), along with TH filaments (cyan).
(**D**) TH filaments (cyan) and converted spots (yellow spheres). Only centroid spot of each straight filament unit is shown.
(**E**) Segregation of TH spots by overlap with Phalloidin surface (grey) into internal "cortical" spots (red spheres) and external "periosteal" spots (yellow spheres).
(**F**) Quantification of TH^+ fibers in cortex (Ctx), periosteum (PO), and medullary space (Med). Data are represented as mean +/- SD. Statistical analysis by one-way ANOVA, post-hoc Bonferroni statistical test for pair-wise significance; * $p<0.05$, ** $p<0.01$. (n = 5 bone hemisections)

day 3 mice, which do not yet have a significant density of osteocytes[83]. In the context of data suggesting a deleterious impact of sympathetic nerve signaling on bone during aging, it was necessary to assess NET expression and function in adult tissues. Through immunofluorescence methods, we were able to identify NET expression in adult bone-embedded cortical osteocytes, a result consistent with higher NET uptake activity in flushed femurs versus marrow. A majority of NET^+ osteocytes were observed in the periosteal cortical envelope, consistent with the observed location of SNS fibers and the lower turnover of cortical versus trabecular bone. These results thus suggest that osteocytes control, via uptake of NE, the communication between sympathetic nerves and $\beta2AR^+$ bone cells, although it remains unclear which effector cell in the osteoblast lineage, osteoblasts, osteocytes, or both, is the target of sympathetic nerves. Isoproterenol (ISO) stimulation of the β2AR affects bone through both arms of the bone remodeling process, inhibiting osteoblast proliferation via cell-autonomous circadian genes *Per* and *Cry*[95], and stimulating RANKL production to promote osteoclast differentiation[88]. These two actions cannot occur within the same cell, as the anti-proliferative action of NE relates to pre-osteoblasts, whereas osteocyte-derived RANKL plays a predominant role in bone remodeling[13]. Furthermore, these two cell types inhabit different locations in bone: pre-osteoblasts are located near the endosteal bone surface and migratory[194], whereas osteocytes are embedded and stationary in the calcified bone matrix. Localization of SNS fibers near perivascular hematopoietic[57] and mesenchymal stem cell niches[55,195] were previously reported. However, only a few reports [190,196] suggest close vicinity with osteoblast-lineage cells. Whether the primary target of endogenous NE among bone-forming cells is the skeletal stem cell, osteoblast, or the osteocyte is thus still unclear.

Compared to previous reports using histological methods against sympathetic nerve markers [92,93,159,163,197–199], our study provides an independent analysis of sympathetic innervation of the skeleton, using an alternative method based on TH-Cre-mediated fluorescent signals and 3D bone CLARITY imaging. Bone CLARITY has been previously applied with success to imaging rare cell populations in

whole mouse bones[192]. Here, we applied this technology for visualizing long sympathetic nerves in adult femurs, with a focus on intracortical distribution. We were able to confirm innervation of the periosteum and to detect innervation of the femoral cortices, but were not able to detect fine nerve terminals reaching osteocytes. Limitation associated with the cytoplasmic expression of the tdTomato reporter used in this study may account for the lack of detection of fine fibers within cortical bone, as the thin diameter of sympathetic nerve terminals may be insufficient for significant cytoplasmic fluorescent protein diffusion and detection. As a potential future study, a membrane-bound fluorescent protein reporter (i.e. the *ROSA26-mTmG* mice strain) in sympathetic nerves could be used in attempts to increase the fluorescent signal of fine nerve fibers in bone. It is also possible that other mechanisms aside from direct osteocyte-neuronal interactions are involved in the effect of NE on bone remodeling. Studies focused on the adipose tissue indicated that only approximately 4-12% of inguinal fat pad adipocytes are in direct contact with SNS fibers[200], with inter-adipocyte gap junctions shown to propagate secondary messenger molecules like cAMP between adjacent cells. The inter-osteocyte connectivity and the connections between osteocytes and osteoblasts makes this putative signaling mechanism possible in bone, as inter-osteocyte communication has already been demonstrated to translate mechanical strain signaling to adjacent cells[201]. In addition, the gap junction protein Connexin43, encoded by *Gja1*, can form gap junctions between adjacent cells, and expression of a dominant-negative *Gja1* mutant resulted in increased cortical bone[69,71]. It is thus plausible that inter-osteocyte communication via gap junctions following β2AR stimulation in osteocytes could mediate secondary messenger diffusion, and contribute to propagating signals from single stimulated cells across the larger osteocyte network to eventually impact bone remodeling. In any case, the data presented herein provide a strong incentive to assess the *in vivo* functional relevance of NET-mediated NE uptake by osteocytes and its impact on bone remodeling during bone acquisition and aging.

Bone CLARITY has multiple future application for studying interaction between SNS and bone. One question is the anatomical pathway of SNS innervation of bones, which was approached in Chapter 2. The femoral artery sympathetic nerve loss-of-function studies demonstrated that the periarterial sympathetic plexus around the femoral artery may not solely be responsible for innervation of the femur and tibia. It is possible that other sources, such as the obturator artery supplying the femoral head is another SNS innervation source. However, this candidate approach of ablating other sympathetic pathways may present issues, since the procedure is reliant on both the technical success of the chemical sympathectomy protocol, as well as the accurate biological target. A less risk non-candidate approach would be visualization of labeled nerves in an intact limb. Whole-mount staining of genetic tracing of β-galactosidase-expressing tissues has long been available for studying structures during embryologic development. This method is relatively simple, as the tissues are smaller and easier for both reagent penetration, and has been applied to studying the sensory innervation of the skeleton during development[202]. However, the resolution of β-gal staining methods is limited to macroscopic structures due to the diffusion of the chromogenic chemical product. Also, effective staining in whole-mount adult tissues is prevented by the size and impermeability of the adult tissues. The bone CLARITY technique with light sheet imaging, coupled with the use of fluorescent protein reporters, provide the potential for resolving smaller structures in higher resolution.

There are multiple limitations to bone CLARITY methods, primarily arising from technical aspects of bone clearing. In the field, multiple tissue-clearing protocols, and refractive index matching solutions, and imaging techniques exist to improve speed of processing, tissue morphology, and tissue clarity[188,189,192,203–206]. However, the age and the size of the tissue are considered the greatest limiting factors – due to limiting volume and depth of solution penetration, the increased integrity of connective tissues and membrane, and the increased deposition of heme metabolic products responsible for autofluorescence. Many of these issues are compounded in bone, where calcified tissues are less

permeable, and insufficient decalcification presents addition barriers to light penetration. Thus, while it is easily feasibly to apply bone CLARITY to whole embryonic limbs or animals or bones from young (<3 months old) animals, applying this to larger/older structures requires additional advances.

Whole-mount imaging allows easy identification of rare cells and structures otherwise difficult in traditional thin-section histology. This is especially relevant to distances between objects at different depths of the object. It also allows semi-automated analysis of structures, similar to analytical software such as Bioquant or ImageJ for 2D images, thereby eliminating the need for manual quantification in 3-dimensional space. In this chapter, we have demonstrated application of this technology to stratifying TH^+ fiber innervation of bone cortex, periosteum, and medullary marrow. The Imaris program can also be used to measure the distance between fluorescently-labeled cells and TH^+ fibers. Future studies could involve additional transgenic fluorescent protein reporters such as the osteocytic *Ocn-GFP*, or the vascular *Tie2-GFP* markers. A mouse with transgenic fluorescent reporters for both osteocytes and sympathetic nerves (*Ocn-GFP*; *Th-Cre*; *ROSA26-tdTomato*) would be used to study the distance of osteocytes from SNS nerves, providing quantification of a "watershed" of NET-expression osteocytes relative to TH^+ SNS fibers.

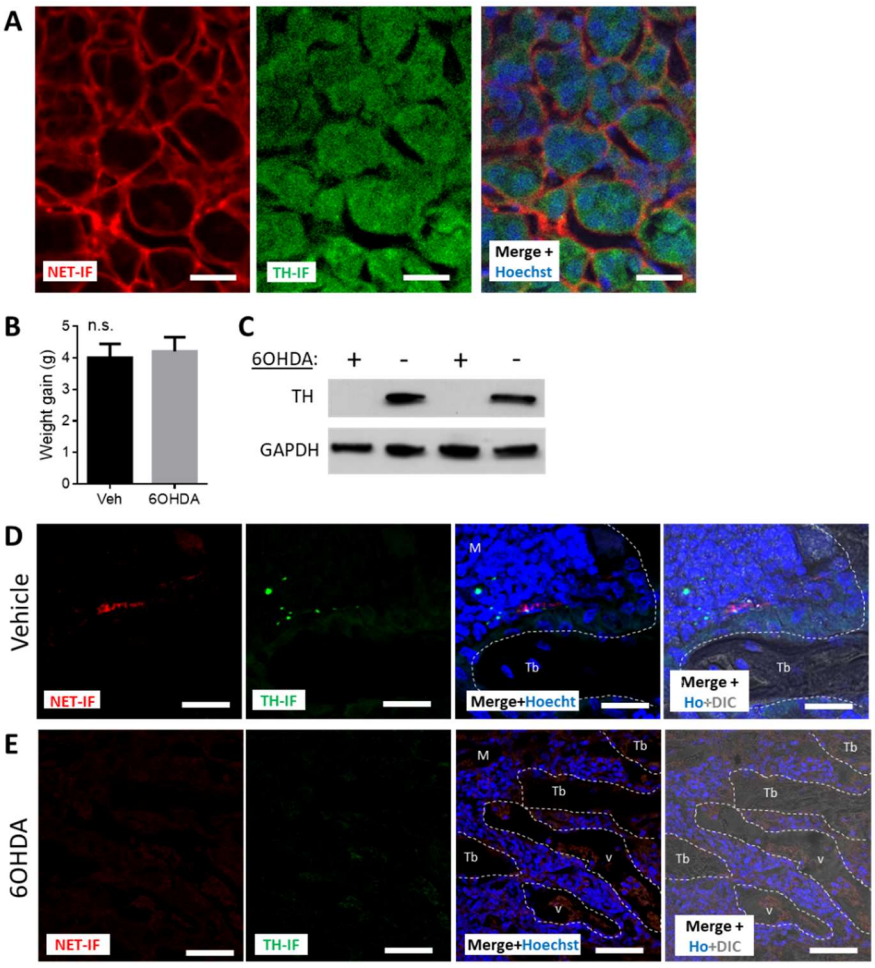

Figure S4.1 – NET immunofluorescence controls

Legend: vessel (v), trabeculae (Tb), cortex (Ctx), marrow (M), periosteum (PO).

(**A**) Confocal microscope images of adrenal medullary catecholaminergic cells, used as positive control for NET expression. Cells are immunopositive for cytosolic TH (green), and for peri-cellular NET (red). Images are representative of sections from 3 animals, scale bar 20um.

(**B**) Weight difference in mice after 5-day treatment protocol with 6OHDA or saline vehicle controls (n = 7 per group).

(**C**) Representative Western blot for TH and reference protein GAPDH of whole femur tissues from mice chemically sympathectomized with 6OHDA or saline vehicle controls (n=5 per group).

(**D**) Confocal microscope images of proximal tibia from saline-vehicle treated mice. TH-immunopositive fibers (green) are found in the marrow near NET-immunopositive fibers (red). Scale bar 50um.

Images are representative of sections from 3 animals.

(**E**) Confocal microscope images of proximal tibia from mice chemically sympathectomized with 6OHDA. TH- and NET-immunofluorescence was not observable in the tissues. Images are representative of sections from 3 animals, scale bar 50um.

All results are shown as mean +/- SD. Statistical analysis by two-tailed Student t-test, statistical significance taken at $p < 0.05$.

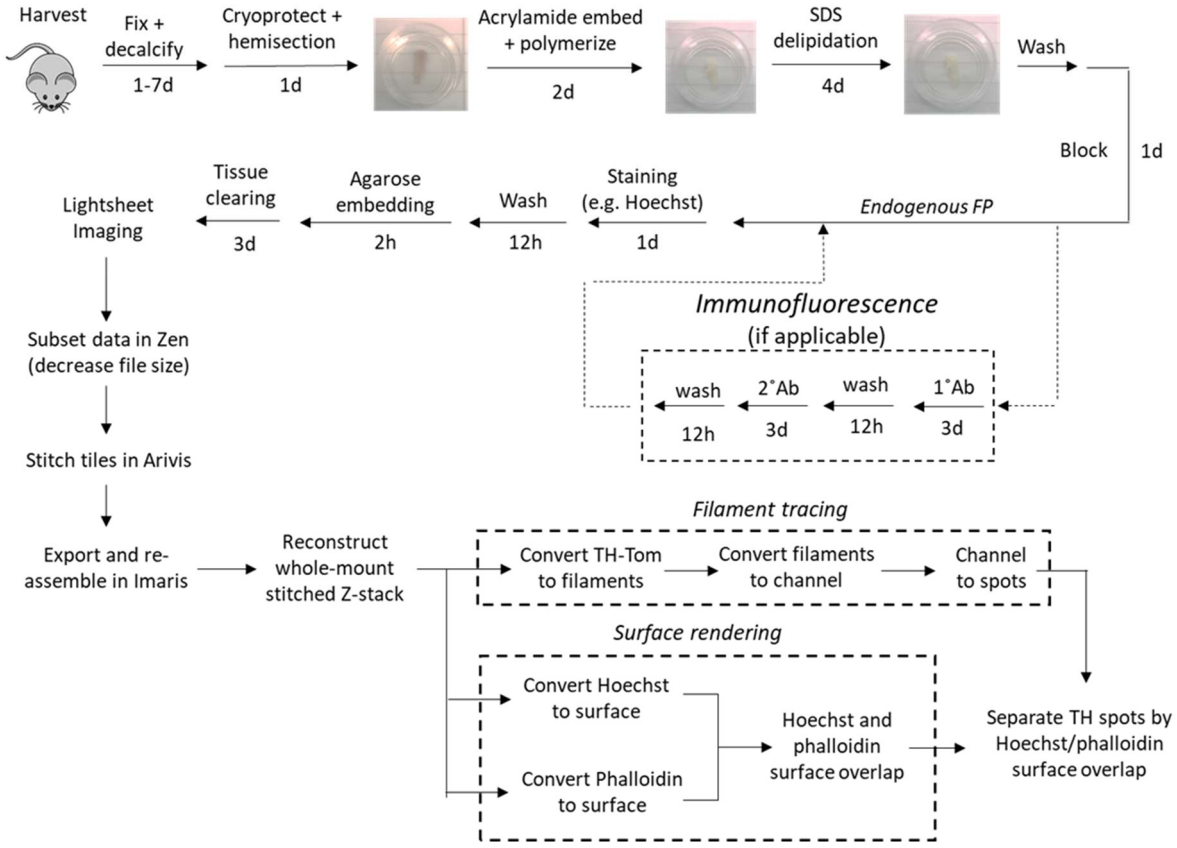

Figure S4.2 – Bone CLARITY clearing and imaging workflow

Schematic representation of tissue preparation for clearing, imaging, and data analysis of bone tissue innervation

Conclusions

From the studies presented in this thesis, the model of bone-sympathetic interaction has been further refined (**Fig. 5.1**). In brief, sympathetic neurons richly innervated the periosteum and cortical bone, and release NE, which acts on only the β2AR expressed on mature osteoblast/osteocytes. These cells then respond by expression the osteoclastogenic gene *Rankl*, which can act on osteoclasts to increase bone resorption. Finally, matrix-embedded mature osteocytes can terminate NE signaling via uptake through NET. While these findings also raise more questions, it also allows the use of more precise tools such as tissue-specific gene deletions to probe individual components. This new paradigm offers a higher resolution model of the cells and tissues involved in NE signaling and metabolism in bone, both visually and mechanistically.

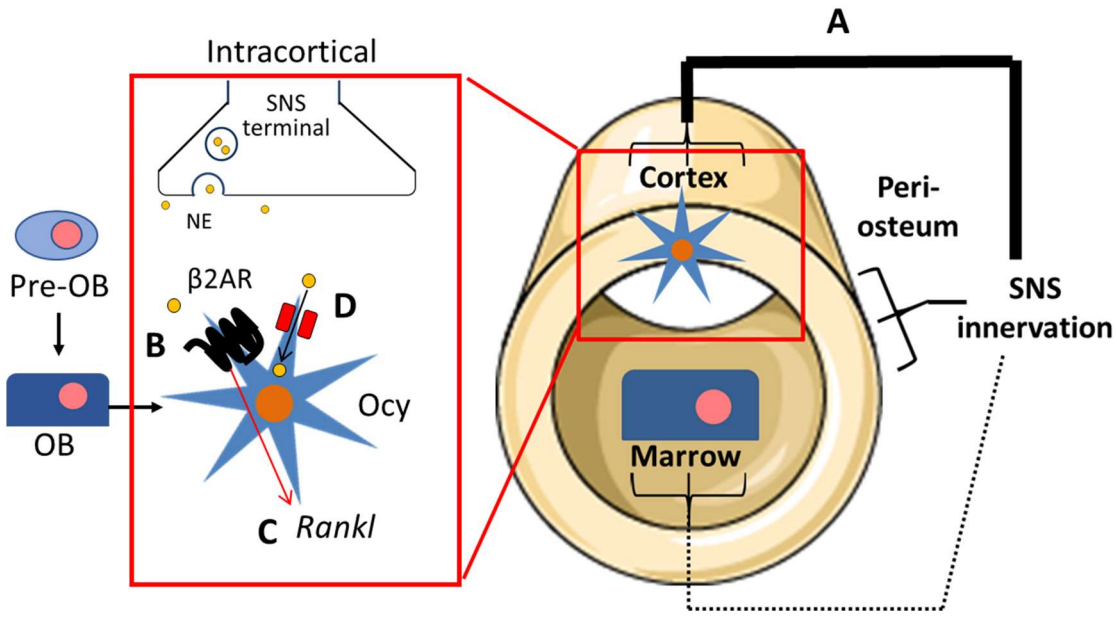

Figure 5.1 – Updated paradigm of sympathetic nervous system action on bone
Sympathetic nervous system (SNS), which densely innervates the bone cortex (**A**), releases the norepinephrine (NE), which acts on β2 adrenergic receptors (β2AR) on mature osteoblast/osteocytes (Ocy), and not immature osteoblasts (OB) or osteoblast precursors (pre-OB) (**B**). This stimulation triggers expression of the pro-osteoclastogenic *Rankl* that is capable of inhibiting osteoblast proliferation (**C**). These cortical osteocytes also are also capable of NE uptake via NET (**D**).

The categorical study of adrenergic receptor expression and signaling throughout *in vitro* osteogenically differentiation in BMSCs revealed that the β2AR is the major receptor expressed in the osteoblastic lineage (**Fig. 5.2A**), and that expression persists throughout differentiation. However, only mature osteoblasts/osteocytes express the osteoclastogenic *Rankl* in response to adrenergic stimulation, though it is possible that the β2AR on cells earlier in the osteoblast lineage act to inhibit osteoblast proliferation.

Acute studies in mice *in vivo* revealed that mice stimulated with either pharmacologic ISO or endogenous NE release via AIS express *Il6* in the skeleton. However, only the pharmacologic treatment of ISO leads to increased *Rankl* expression, suggesting critical mechanistic differences exist between exogenous ligands and endogenous NE release (**Fig. 5.2B**). Furthermore, bone cortical tissue is capable of significant reboxetine-sensitive [^{3}H]-NE uptake via NET (**Fig. 5.2C**). Since bone cortex is enriched for matrix-embedded osteocytes, these results suggest that osteocytes *in vivo* are a major catabolic sink in bone *in vivo*.

Investigation of aged animals reveal their bone tissues have increase NE content, and decreased catecholamine metabolism. Further investigation confirmed that basal skeletal NE levels gradually increase with age, and that the aged skeleton has decreased NET expression and function (**Fig. 5.3**). This confirms that sympathetic dysfunction exists in aged bone, and sets the stage for interventions targeting the skeletal adrenergic system during age-related bone loss.

Finally, using both traditional histological methods and newly adapted whole-mount bone clearing and imaging technology, the bone adrenergic system is able to be directly observed. Osteocytes express NET (**Fig. 5.4A**), supporting the neurochemical data. Additionally, the sympathetic innervation of

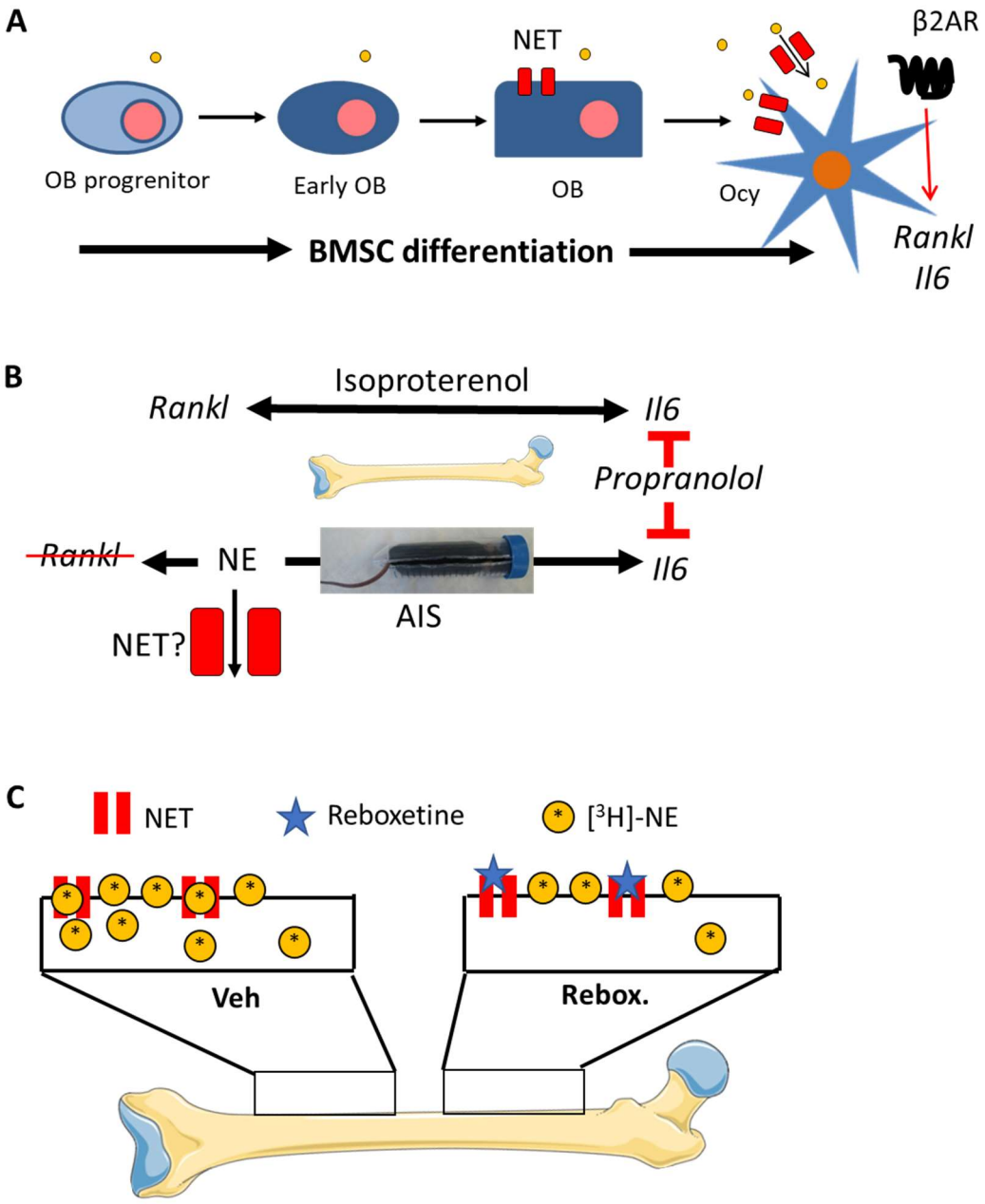

Figure 5.2 – Acute adrenergic pharmacology in differentiated osteoblasts and in bones
(**A**) The β2AR is expressed and functional in mature osteoblasts/osteocytes. *Net* expression and uptake increases with BMSC differentiation.
(**B**) Stimulation of animals with ISO or AIS increase Il6, but not *Rankl* expression in bone
(**C**) Bone is capable of specific reboxetine-sensitive [3H]-NE uptake via NET.

bone was able to be visualized using tissue clearing and whole-mount light sheet imaging methods. Furthermore, the extent of innervation was able to be quantified with image analysis methods (**Fig. 5.4B**)

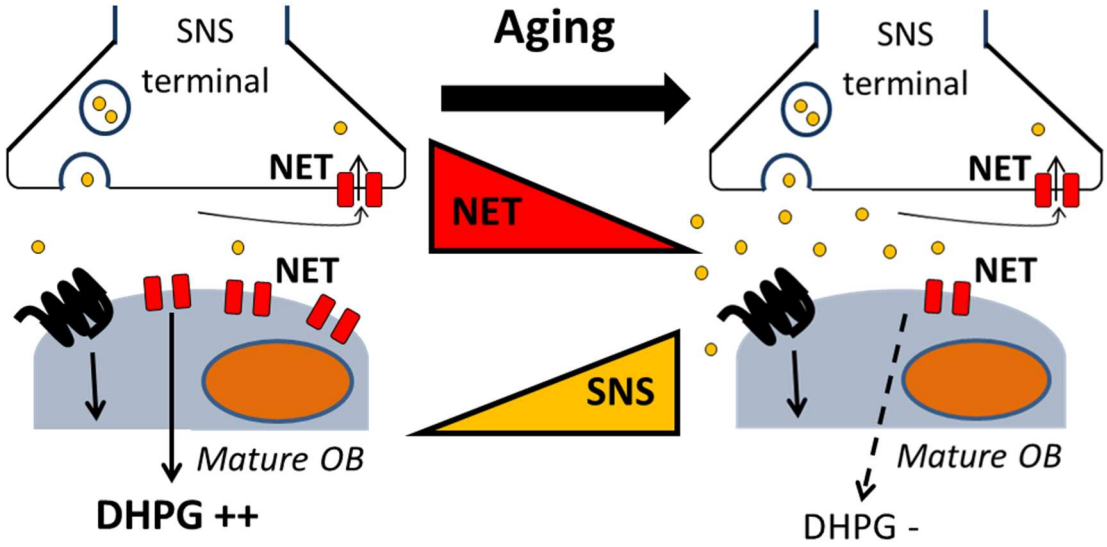

Figure 5.3 – Skeletal sympathetic nervous activity changes with age
Decreased bone NET activity and expression with age coincides with increased basal tissue NE Does.

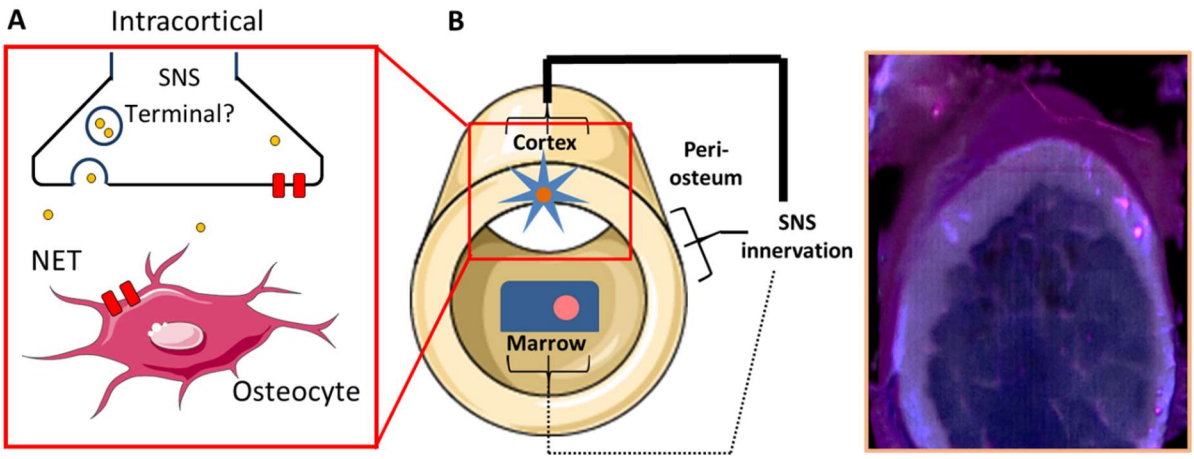

Figure 5.4 – SNS fibers innervate the bone cortex where NET^{+} osteocytes reside
(**A**) Osteocytes express NET protein *in situ*
(**B**) Bone CLARITY allows visualization of bone periosteal and cortical SNS fibers

Chapter 5. Methods

Animals

Wild-type male C57BL6/J mice (JAX #000664) and *Th-Cre* mice (JAX #008601) on a C57BL/6J background were purchased from the Jackson Laboratory, and allowed to acclimate to the environment for at least 1 week prior to experimentation. ROSA-LSL-tdTomato reporter mice (Ai9, JAX#007905) on a C57BL/6J background were a generous gift from Dr. Dongsu Park. *Th-Cre*; *ROSA-LSL-tdTomato* (*Th-Tom*) mice were generated by our laboratory, and genotype was confirmed by PCR (primers **Table S1**.). Male Sprague-Dawley rats (Charles River #SD) 6-weeks of age (~250g) were purchased from Charles River Laboratories, and allowed to acclimate to the environment for at least 1 week prior to surgery.

Animals were housed 2-5 per cage, kept on a 12 hour light-dark cycle in a temperature-controlled environment (22˚C), and had *ad libitum* access to water and standard chow. This study used male mice since previous studies[83] in $Net^{-/-}$ mice showed a bone phenotype only in males. All animal procedures were performed according to protocols approved by the Institutional Animal Care and Use Committee at Baylor College of Medicine.

Unilateral femoral artery sympathectomy surgery

Sprague Dawley rats were administered both extended release buprenorphine SR (1mg/kg), and meloxicam SR (4mg/kg), prior to surgery, induced under anesthesia with 3% inhaled isoflurane, and maintained with 2.5% isoflurane. The femoral artery sympathectomy (FASx) surgery was performed according to the images taken (**Fig. S2.2**). The final goal to isolate the femoral artery in a parafilm strip, and to apply a phenol-soaked thread around the artery (**Fig. S2.2G**). In brief, the surgical site was shaved, cleaned, and sterilized. A ~1.5 cm incision was made along the inguinal fold. Superficial fascia

(superficial to muscles) was dissected to access nerve, artery, and vein sheath. The femoral triad (nerve, artery, and vein), insert probe/forceps from internal/inferior direction pointing towards iliac tubercle ("waist"), deep to the sheath. The nerve (lateral) and the artery/vein bundle were separated. The vein (medial, fat, blue, and thin-walled) was then separated from the artery (pale and thick walled, will drain of color of pinched proximally). A 0.5cm wide sterile parafilm strip was threaded to isolate the artery to isolate it from surrounding tissues. A 4-0 suture thread soaked in 10% phenol in ethanol was then passed around the artery for 10 seconds, until the tissue bleached. The thread and parafilm strip was removed, and the surgical site closed with sutures. Animals administered Meloxicam SR (4mg/kg bodyweight subcutaneously) every 24h.

Animals were sacrificed, and tissues were harvested 7 days post-surgery. Femoral nerve, tibia, and femur were dissected and cleaned of connective tissues. Femur were cut at the mid-diaphysis – proximal femur was fixed in 4% PFA and decalcified for histology. Distal femur and tibia epiphyses were clipped, and centrifuged to separate marrow and cortex, and tissues were snap frozen in $LiqN_2$. Cortical tissues were crushed with mortar and pestle, and tissues were separated for analysis. Femoral nerve and proximal femur immunofluorescence for tyrosine hydroxylase (TH, a marker for sympathetic nerves), and tissue WB for TH were used to verify extent of sympathectomy.

In vivo catecholamine measurements

Male mice aged 3 and 18 months were sacrificed for high pressure liquid chromatography (HPLC) measurements. Tibia were cleaned of connective tissues and clipped at the epiphyses. Marrow was separated from cortical bone via centrifugation at 5000g for 2 min, and snap frozen in liquid nitrogen. Frozen tissues were crushed in a mortar and pestle, resuspended in 100ul of 0.1% reduced L-glutathione (G4251, Sigma-Aldrich) in 0.1M Tris pH 8.0 to protect from oxidation. Norepinephrine and L-dihydroxyphenylalanine (L-DOPA) quantification was determined by HPLC at the Neurochemistry Core

Lab, Vanderbilt University Center for Molecular Neuroscience Research (Nashville, TN), using methods previously described[207]. Sample protein content were measured by BCA assay (Cat#23225, Thermofisher) and used to normalize catecholamine levels.

Mice aged 1, 2, 5, 9, and 12 months were sacrificed for NE ELISA measurements. Tissues were prepared similarly to those for HPLC measurements. Frozen bone powder was resuspended in glutathione tissue extraction buffer (0.01N HCl, 0.15mM EDTA, 0.1% reduced glutathione), and neutralized with 10% volume of 1.0M Tris pH 8.0 prior to NE ELISA. NE levels were measured by high sensitivity NE ELISA kit (Cat #NOU39-K01, Eagle Biosciences) according to manufacturer's protocol. An aliquot of tissue suspended in extraction buffer was used to quantify protein concentration, and used to normalize NE measurements.

Acute in vivo adrenergic stimulation

Male mice aged 8 weeks were randomized to pre-treatment with either saline vehicle or propranolol HCl (5mg/kg body weight) (Cat#P0884, Sigma) via intraperitoneal injection 30 minutes prior to treatment. Animals were the either treated with either saline vehicle or isoproterenol (3 mg/kg bodyweight) (I6504, Sigma) via i.p. injection, or with i.p. saline vehicle and subject an acute immobilization stress protocol[208] or returned to cages. Animals were euthanized following 2.5h of treatment. Tibia and femur were harvested, cleaned of connective tissues, and snap frozen. Whole bones were then crushed with mortar and pestle, and RNA extracted with Trizol according to manufacturer's protocol.

Specific [^{3}H]-NE in vivo uptake

In vivo uptake assays were conducted in 6-week old C57BL6/J male mice. Animals were pretreated twice at t = -1h and -0.5h with either sterile saline vehicle or Reboxetine mesylate (Cat#1982, Tocris) at 20mg/kg intraperitoneally. This concentration was chosen based on previous studies with reboxetine tissue binding[139,209] and reported anti-mobility effects of the drug[210,211]. Then, 0.2 µCi L-[7-^{3}H]-NE (Cat#NET377250UC, Perkin Elmer), approximately 10nmol in 200ul warmed saline, was administered via tail vein injection. After 10 minutes of radioligand circulation, animals were euthanized by cervical dislocation, and tibia and femur were harvested. Bones were cleaned of connective tissues and clipped at the epiphyses. Marrow was separated from cortical bone via centrifugation at 5000g for 2 min, and snap frozen in liquid nitrogen. Frozen cortices were crushed with a mortar and pestle. Marrow and powdered cortical tissues were incubated in lysis buffer (0.15mM EDTA, 20mM Tris pH7.5, 0.05% Triton-X100), and radioligand was quantified by scintillation counting. An aliquot of tissue lysate resuspended in buffer was used to measure tissue DNA content by Picogreen dsDNA assay kit (Cat#P7589, Thermofisher), used to normalize radioligand tissue quantities to cell density. Specific uptake was calculated using the following formula: $specific\ uptake = \frac{CPM_{Veh}}{dsDNA_{Veh}} - \frac{CPM_{Rebox}}{dsDNA_{Rebox}}$.

Cell culture

Bone marrow was extracted from long bones of 2-4 month-old C57BL6/J mice by centrifugation, as previously described[208], and was plated on 6-well tissue culture treated plates in α-MEM (+glutamate, +nucleosides), supplemented with 10% fetal bovine serum and 100 U/ml penicillin/streptomycin at seeding density of 2x10^5 cells/well for three days. At that time, non-adherent cells were washed, and adherent bone marrow stromal cells (BMSCs) were differentiated in osteogenic medium (α-MEM, 10%

FBS, pen/strep with 50ug/ml L-ascorbic acid and 5mM β-glycerophosphate), changed every 2 days, until harvested for assays at indicated time points.

Specific [^{3}H]-NE in vitro uptake

The first passage of BMSCs were plated into 6-well plates at a density of 1x10^6 cell/well, allowed to adhere for 24h, and differentiated in osteogenic media until the experiment. Osteogenic medium was removed from differentiated BMSCs, cells were washed with warm 1xPBS, and replaced with serum-free α-MEM. Cells were pre-treated with 1 mM reboxetine mesylate (Cat#1982, Tocris) or vehicle 30 minutes prior to experimentation. Then, 1x10^{-7} M L-[7-^{3}H]-NE (Cat#NET377250UC, Perkin Elmer) in α-MEM was added onto the cells for 30 minutes. The supernatant was then aspirated via pipette, and cells rinsed with ice cold PBS, into a sealed container for radioactive disposal. Cells were then incubated in 200ul lysis buffer (0.15mM EDTA, 20mM Tris pH7.5, 0.05% Triton-X100), and collected into an Eppendorf tube. Radioligand content was quantified by scintillation counting. An aliquot of tissue lysate suspended in lysis buffer was used to measure tissue protein concentration via BCA assay, and used to normalize radioligand content.

Gene expression assays and RT-PCR

Tibia and brainstem were harvested, cleaned of connective tissues, and flash frozen in liquid nitrogen. Marrow and cortex tissue were separated (where applicable) via centrifugation at 5000g for 2 min, and snap frozen in liquid nitrogen. Frozen tissues were crushed via mortar and pestle. Total RNA was extracted from tissue powder and differentiated BMSCs using TRIzol (Cat# 15596026, Thermofisher). Contaminating genomic DNA was digested with DNAse I (Cat#18068015, Thermofisher). cDNAs were synthesized from 1ug RNA using high capacity cDNA reverse transcription kit (Cat#4368814,

Thermofisher) according to the manufacturer's instructions. Estimating 80% reverse transcription efficiency, 25ng cDNA was used in each reaction. Gene expression was quantified by qRT-PCR using iTaq Universal Probes Supermix (Cat#1725131, Bio-rad) or iQ SYBR Green Supermix (Cat#1708882, Bio-rad) according to manufacturer's instruction for Taqman and SYBR probes, respectively. Target gene expression ratios were quantified using a standard curve of cDNA from similar tissues and normalized with references genes *Gapdh* and *Hprt*. RT-PCR of catecholaminergic genes were performed with primers designed for SYBR qRT-PCR, then separated and visualized on a 1% agarose gel. All SYBR and RT-PCR primer sequences and thermocycler protocols are provided in the Supplementary Data (**Table S1**). SYBR primer specificity for target gene amplification was confirmed by the presence of a single peak on the melt curves.

Western blot analysis

Femur were dissected and cleaned of connective tissues and clipped at the epiphyses. Marrow was separated from cortical bone via centrifugation at 5000g for 2 min, and snap frozen in liquid nitrogen. Frozen femur cortices were crushed in a mortar and pestle. Protein was extracted from marrow and crushed cortex tissue by RIPA buffer extraction with protease inhibitor cocktail (Cat#P8340, Sigma-Aldrich), and concentrations quantified by BCA assay. Total of 15ug protein was denatured with 2.5% β-mercaptoethanol, separated by SDS-PAGE on a 4-15% gel, and transferred onto a PVDF membrane. Membranes were blocked with 5% nonfat milk powder in TBS 0.05% Tween-20 (TBS-T) at RT for 30 minutes. For age-dependent NET expression experiments, Mouse anti-NET (Cat#NET05-2, Mab Technologies) and mouse anti-β-actin (Cat#A2228, Sigma-Aldrich) primary antibodies were incubated at 4˚C overnight diluted 1:500 and 1:2000 in blocking buffer, respectively. For confirmation of 6OHDA chemical sympathectomy, Rabbit anti-TH (Cat#AB152, Millipore) and Rabbit anti-GAPDH (Cat#2118, Cell

Signaling Technology) primary antibodies were incubated at 4˚C overnight diluted 1:100 and 1:2000 in blocking buffer, respectively. Membranes were washed with TBS-T and incubated for 1h at RT with HRP-conjugated secondary goat anti-mouse antibody (Cat#sc-2005, Santa Crus) or HRP-conjugated goat anti-rabbit antibody (Cat#12-348, Millipore) diluted 1:10,000 in blocking buffer. Membranes were then washed and developed using ECL reagent (Cat#68835, Cell Signaling Technologies) on autoradiography film. Band intensities were quantified using ImageJ, normalized with respective β-actin loading control, and standardized with an identical internal positive control present on both gels.

Bone tissue immunofluorescence

Femur and tibia were dissected from 6-week old males, fixed in 4% paraformaldehyde overnight at 4˚C, and decalcified with daily changes of 0.5M EDTA pH 8.0 at 4˚C for 72h. Tissues were then dehydrated in graded series of ethanol, cleared in xylenes, embedded in paraffin, and sectioned. Tissue sections were deparaffinized with xylenes, and rehydrated through graded ethanol baths. Antigen retrieval was performed on sections by incubating slides in retrieval buffer (10mM Tris, 1mM EDTA, 0.05% Tween-20, pH 9.0) for 30 minutes at 90˚C, and allowed to cool in buffer for 30 minutes, and proceeded to immunostaining.

Kidney and adrenal glands were dissected from 6-week old males, removed of excess perirenal fat, and fixed in 4% paraformaldehyde overnight at 4˚C. Tissues were cryoprotected through 48h incubation in 30% sucrose, and embedded in OCT for cryosectioning. Tissue sections were dried at RT for 1h, and rehydrated in PBS to remove excess OCT, and proceeded to immunostaining.

All tissue sections to be immunostained were permeabilized with 0.1% Triton, blocked with 5% normal goat serum 0.05% Tween in PBS, and incubated with primary antibodies: mouse anti-NET (Cat#NET05-2, Mab Technologies) or rabbit anti-TH (Cat#AB152, Millipore), or mouse IgG1 isotype

control (Cat#MAB002, R&D Biosystems) at 1:500 dilution in blocking solution at 4˚C overnight. Slides were washed and incubated with secondary antibody goat anti-mouse IgG Alexafluor594 conjugate (Cat#115-587-003, Jackson Immuno) or anti-rabbit IgG Alexafluor488 conjugate (Cat#111-547-003, Jackson Immuno) at 1:1000 dilution in blocking solution at RT for 3h. Sections were washed, stained with nuclear stain Hoechst (Cat#H3569, Themofisher), and mounted. Fluorescent and bright-field Differential Interference Contrast (DIC) images were acquired using a Nikon A1R-s confocal microscope with a 40x Plan Fluor/0.75 NA objective. Images were acquired with identical laser intensity and camera exposures, and processed identically with NIS Elements Viewer 4.20 (Nikon Instruments Inc., Melville NY). A total of n = 4 animals, 4 tibial sections per animal, 2 frames per each were analyzed in ImageJ. The observer was blinded to the identity of images to eliminate bias.

Human bone immunofluorescence

Fresh human tissue samples were rinsed in sterile PBS, cut into ~0.5cm-long pieces, and fixed in 4% paraformaldehyde overnight at 4˚C. Tissues were decalcified in 5% formic acid at RT for 48h. Samples were washed in PBS at RT for 12h, cryoprotected overnight in 30% sucrose solution at 4˚C, and embedded in OCT for cryosectioning. Tissues sections were hydrated, and antigen retrieval was performed by incubating slides in buffer (10mM Tris, 1mM EDTA, 0.05% Tween-20, pH 9.0) for 30 minutes at 70˚C, and allowed to cool in buffer for 30 minutes. Sections were permeabilized with 0.1% Triton, blocked with 5% normal goat serum 0.05% Tween in PBS, and incubated with primary antibody mouse anti-hNET (Cat#NET17-1, Mab Technologies) or rabbit anti-TH (Cat#AB152, Millipore), or IgG isotype controls of respective species, at 1:500 dilution at RT for 6h. Slides were washed and incubated with secondary antibody goat anti-mouse IgG Alexafluor594 conjugate (Cat#115-587-003, Jackson Immuno) or goat-anti rabbit IgG Alexafluor488 conjugate (Cat#111-547-003, Jackson Immuno) at 1:1000

dilution in blocking solution at RT for 3h. Sections were washed, stained with nuclear stain Hoechst (Cat#H3569, Themofisher), and mounted. Images were acquired using a Nikon A1R-s confocal microscope with a 40x Plan Fluor/0.75 NA objective. Representative images were from at least 4 different sections.

6-OHDA Chemical sympathectomy

The chemical sympathectomy protocol was adapted from[57]. A total of 18 4-week old male mice, 9 treatment, 9 vehicle controls, were randomized and weighed. Animals were administered two doses of L-6-hydroxy-DOPA HCl (6OHDA, Cat#H4381, Sigma-Aldrich) in sterile saline vehicle via intraperitoneal injection at the following concentrations: day 0 at 100mg/kg bodyweight, and day 2 at 250mg/kg bodyweight. Animals were weighed and sacrificed on day 5.

Bone CLARITY protocol

The protocol for processing and clearing bone tissues for whole-mount imaging was adapted from [40], and summarized in **Fig S3**. Femur were harvested from 6-week old male mice, bluntly stripped of overlying muscles and connective tissues, and fixed in 4% paraformaldehyde overnight at 4˚C. Bones were decalcified in daily changes of 0.5M EDTA pH 8.0 at 4˚C for 72h to increase light and reagent penetration. Tissues were then washed with 2h RT incubation in PBS, cryoprotected in 30% sucrose at 4˚C overnight, and cryoembedded in OCT mounting medium for hemisectioning to improve access of reagents and stains to the bone medulla. Hemisectioned tissues were thawed and washed of OCT in PBS, and incubated in A4P0 acrylamide solution containing 4% acrylamide (Cat# A4058, Sigma-Aldrich), 0.25% VA-044 photoinitiator (Cat# 27776-21-2, Wako Chemicals) in PBS at 4˚C overnight. Tissues were degassed via gas exchange by bubbling N_2 through the solution under a vacuum. The acrylamide

hydrogel was polymerized by incubation for 6h in a 37˚C water bath. The hydrogel supports the protein structures through the subsequent delipidation and washing steps.

Tissue lipids, a major source of light scattering, were washed away by shaking samples in 8% SDS in 1x PBS at 37˚C for 3d, with daily changes of SDS solution. Heme and its porphyrin metabolites, a major source of tissue autofluorescence[40], were removed by incubating tissues in 25% amino alcohol Quadrol (N,N,N',N'-tetrakis(2-hydroxypropyl) ethylenediamine) (Cat#122262, Sigma-Aldrich) in PBS at 37˚C for 2d. Finally, tissues were washed in PBS for 24h then stained with Hoechst (Cat#H3569, Themofisher). Tissues were then embedded into 1% agarose-PBS, and cleared by immersion in Refractive Index Matching Solution (RIMS), comprising of Histodenz (Cat#D2158, Sigma-Aldrich) solution in PBS, through daily stepwise incubation of RIMS with index refraction RI=1.38, 1.43, and finally 1.48 as recommended for bone[186].

Light sheet imaging

Tissues were imaged using a Zeiss LightSheet Z.1 side plane illumination microscope with an N-Achroplan 5x/0.13 objective. Before imaging, samples were placed in the LightSheet chamber filled with RIMS 1.48 for at least 1 hour, allowing equilibration between the RIMS solution and sample. To image the entire bone, we acquired multiple Z-stack tiles with 15% overlap. Samples were imaged with a frame rate of 22 frames/sec at a depth of 16 bits, with continuous motor drive through the Z-plane of the tissue. Tissues were excited by alternating left and right light sheets, and acquired images were merged using Gaussian merge function in the Zen software (Zeiss, Germany). All tissue samples were imaged using the same laser power and duration.

Image reconstruction and analysis

The sampled voxel size for a 5x objective was 0.92 x 0.92 x 9 um^3, and generated approximately 300 GB per sample. After acquisition, the data sets were subset to voxel sizes 3.6 x 3.6 x 9 um^3 for faster processing. Tile Z-scans of the images were stitched using the Arivis Vision4D software (arivis AG, Washington DC), exported into Z-stack .tiff images for each color channel. The data was reconstructed by TIFF import in the Imaris v8.0 software (Bitplane, Concord MA), and image dimensions were corrected based on the original data set.

Statistical Analysis

All statistical analyses were performed using Prism version 6 (GraphPad, La Jolla CA). Results are shown as mean +/- standard deviation. Unless indicated otherwise, statistical comparisons using unpaired two-tailed Student's *t*-test for two-group comparisons, or one-way ANOVA followed by Bonferroni post hoc correction. For all analyses, $p < 0.05$ was considered statistically significant.

Table S1 – Genotyping, SYBR qPCR, and RT-PCR primer sequences

Genotyping Primer	**Sequence**	**Thermocycler protocol**	**Comment**
TH-Cre fwd	5’-GCGGTCTGGCAGTAAAAACTATC-3’	95˚C 2m; (95˚C 30s; 62˚C 30s; 72˚C 1m) x30; 72˚C 5m;	
TH-Cre rev	5’-GTGAAACAGCATTGCTGTCACTT-3’		
ROSA-WT fwd	5’-AAGGGAGCTGCAGTGGAGTA-3’	95˚C 2m; (95˚C 30s; 61˚C 30s; 72˚C 30s) x30; 72˚C 5m;	Primer pair for WT ROSA locus (196bp) Identifies heterozygotes
ROSA WT rev	5’-CCGAAAATCTGTGGGAAGTC-3’		
ROSA-tdTomato fwd	5’-CTGTTCCTGTACGGCATGG-3’		Primer pair for tdTomato ROSA locus (297bp)
ROSA-tdTomato rev	5’-GGCATTAAAGCAGCGTATCC-3’		
SYBR Primer	**Sequence**	**Thermocycler protocol**	**Comment**
Mm Hprt	*Mm03024075_m1*	-	*Taqman
Mm Slc6a2	*Mm00436661_m1*	-	*Taqman, AKA *Net*
mGapdh F	5’-TGT GTC CGT CGT GGA TCT GA-3’	95˚C 3m; (95˚C 15s; 60˚C 30s; read) x40	
mGapdh R	5’-TTG CTG TTG AAG TCG CAG GAG -3’		
mDmp1 F	5’-AGT GAG GAG GAC AGC CTG AA-3’	95˚C 3m; (95˚C 15s; 60˚C 30s; read) x40	
mDmp1 R	5’-GAG GCT CTC GTT GGA CTC AC-3’		
mSost F	5’-AGC CTT CAG GAA TGA TGC CAC-3’	95˚C 3m; (95˚C 15s; 59˚C 30s; read) x40	
mSost R	5’-CTT TGG CGT CAT AGG GAT GGT-3’		
mOcn F	5’-ACC CTG GCT GCG CTC TGT CTC T-3’	95˚C 3m; (95˚C 15s; 59˚C 30s; read) x40	
mOcn R	5’-TAG ATG CGT TTG TAG GCG GTC -3’		
mCol1a1 F	5’-GTCCTCCTGGCCCTGCTGGT-3’	95˚C 3m; (95˚C 15s; 59˚C 30s; read) x40	
mCol1a1 R	5’-GATGCGTTTGTAGGCGGTCTTCA-3’		
mRunx2 F	5’-CGG CCC TCC CTG AAC TCT-3’	95˚C 3m; (95˚C 15s; 60˚C 30s; read) x40	
mRunx2 R	5’-TGC CTG CCT GGG ATC TGT A-3’		
mAdrb1 F	5’-GGGAACGACAGCGACTTCTT-3’	95˚C 3m; (95˚C 15s; 61˚C 30s; read) x40	
mAdrb1 R	5’-ACACACAGCACATCTACCGAA-3’		
mAdrb2 F	5’-GGGAACGACAGCGACTTCTT-3’	95˚C 3m; (95˚C 15s; 61˚C 30s; read) x40	
mAdrb2 R	5’-GCCAGGACGATAACCGACAT-3’		
mAdrb3 F	5’-GGCCCTCTCTAGTTCCCAG-3’	95˚C 3m; (95˚C 15s; 60˚C 30s; read) x40	
mAdrb3 R	5’-TAGCCATCAAACCTGTTGAGC-3’		
mAdra1a F	5’-CAGATGGAGTCTGTGAATGGAA-3’	95˚C 3m; (95˚C 15s; 60˚C 30s; read) x40	
mAdra1a R	5’-AATGGTTGGAACTTGGTGATTT-3’		
mAdra1b F	5’-ATACCTGGGTCGTGGAACG-3’	95˚C 3m; (95˚C 15s; 60˚C 30s; read) x40	
mAdra1b R	5’-GGAGCTTGAAAGTGAAGAGTGG-3’		
mAdra1d F	5’-AGCACTACGCGCAGCCTC-3’	95˚C 3m; (95˚C 15s; 60˚C 30s; read) x40	
mAdra1d R	5’-TGCTACTCTGTGTCCCTGGATT-3’		
SYBR Primer	**Sequence**	**Thermocycler protocol**	**Comment**
mAdra2b F	5’-ACCTTCCCTTGCTGACTGTACT-3’	95˚C 3m; (95˚C 15s; 60˚C 30s; read) x40	
mAdra2b R	5’-TGGGAGGGAGGTATTCTAATCA-3’		
mAdra2c F	5’-GGCTGTGAACTTAGGGCTTTAG-3’	95˚C 3m; (95˚C 15s; 60˚C 30s; read) x40	
mAdra2c R	5’-ATAGGAAGTCAGCCCTTGCTC-3’		

mAdra2a F	5’-TTCTTTTTCACCTACACGCTCA-3’	95˚C 3m; (95˚C 15s; 60˚C 30s; read) x40	
mAdra2a R	5’-TGTAGATAACAGGGTTCAGCGA-3’		
RT-PCR Primer	**Sequence**	**Thermocycler protocol**	**Comment**
mTh F	5’-GTCTCAGAGCAGGATACCAAGC-3’	95˚C 3m; (95˚C 15s; 60˚C 45s) x30	
mTh R	5’-CTCTCCTCGAATACCACAGCC-3’		
mDbh F	5’-GACTCAACTACTGCCGGCACGT-3’	95˚C 3m; (95˚C 15s; 60˚C 45s) x30	
mDbh R	5’-CTGGGTGCACTTGTCTGTGCAGT-3’		
mVmat1 F	5’-TCTCTGGCACCTATGCCCT-3’	95˚C 3m; (95˚C 15s; 60˚C 45s) x30	
mVmat1 R	5’-TGCCCACAAATTCATACATCACA-3’		
mVmat2 F	5’-ATGCTGCTCACCGTCGTAG-3’	95˚C 3m; (95˚C 15s; 60˚C 45s) x30	
mVmat2 R	5’-GGACAGTCGTGTTGGTCACAG-3’		
mComt F	5’-CTGGGGGTTGGTGGCTATTG-3’	95˚C 3m; (95˚C 15s; 61˚C 45s) x30	
mComt R	5’-CCCACTCCTTCTCTGAGCAG-3’		
mMaoa F	5’-GGAGAAGCCCAGTATCACAGG-3’	95˚C 3m; (95˚C 15s; 61˚C 45s) x30	
mMaoa R	5’-GAACCAAGACATTAATTTTGTATTCTGAC-3’		

*Taqman primers were used for qRT-PCR of *Hprt* (Mm03024075_m1, Thermofisher), *Slc6a2* (*Net*, Mm00436661_m1, Thermofisher), and *Ucp1* (Mm01244861_m1) according to manufacturer’s protocol.

Bibliography

1. Rosen CJ. Skeletal integration of energy homeostasis: Translational implications. *Bone*. 2016;82:35-41. doi:10.1016/j.bone.2015.07.026
2. Wei J, Shimazu J, Makinistoglu MP, et al. Glucose Uptake and Runx2 Synergize to Orchestrate Osteoblast Differentiation and Bone Formation. *Cell*. 2015;161(7):1576-1591. doi:10.1016/j.cell.2015.05.029
3. Sato M, Asada N, Kawano Y, et al. Osteocytes regulate primary lymphoid organs and fat metabolism. *Cell Metab*. 2013;18(5):749-758. doi:10.1016/j.cmet.2013.09.014
4. Baldock PA, Lin S, Zhang L, et al. Neuropeptide y attenuates stress-induced bone loss through suppression of noradrenaline circuits. *J Bone Miner Res*. 2014;29(10):2238-2249. doi:10.1002/jbmr.2205
5. Fernandes BS, Hodge JM, Pasco JA, Berk M, Williams LJ. Effects of Depression and Serotonergic Antidepressants on Bone: Mechanisms and Implications for the Treatment of Depression. *Drugs Aging*. November 2015. doi:10.1007/s40266-015-0323-4
6. Yirmiya R, Goshen I, Bajayo A, et al. Depression induces bone loss through stimulation of the sympathetic nervous system. *Proc Natl Acad Sci U S A*. 2006;103(45):16876-16881. doi:10.1073/pnas.0604234103
7. Khrimian L, Obri A, Ramos-Brossier M, et al. Gpr158 mediates osteocalcin's regulation of cognition. *J Exp Med*. 2017;214(10):2859-2873. doi:10.1084/jem.20171320
8. Oury F, Ferron M, Huizhen W, et al. Osteocalcin regulates murine and human fertility through a pancreas-bone-testis axis. *J Clin Invest*. 2013;123(6):2421-2433. doi:10.1172/JCI65952
9. Karsenty G, Oury F. Regulation of male fertility by the bone-derived hormone osteocalcin. *Mol Cell Endocrinol*. 2014;382(1):521-526. doi:10.1016/j.mce.2013.10.008
10. Fukumoto S, Martin TJ. Bone as an endocrine organ. *Trends Endocrinol Metab*. 2009;20(5):230-

236. doi:10.1016/J.TEM.2009.02.001

11. DiGirolamo DJ, Clemens TL, Kousteni S. The skeleton as an endocrine organ. *Nat Rev Rheumatol*. 2012;8(11):674-683. doi:10.1038/nrrheum.2012.157

12. Takeda S, Elefteriou F, Levasseur R, et al. Leptin regulates bone formation via the sympathetic nervous system. *Cell*. 2002;111(3):305-317. http://www.ncbi.nlm.nih.gov/pubmed/12419242. Accessed May 7, 2018.

13. Xiong J, Onal M, Jilka RL, Weinstein RS, Manolagas SC, O'Brien CA. Matrix-embedded cells control osteoclast formation. *Nat Med*. 2011;17(10):1235-1241. doi:10.1038/nm.2448

14. Manolagas SC, Parfitt AM. What old means to bone. *Trends Endocrinol Metab*. 2010;21(6):369-374. doi:10.1016/j.tem.2010.01.010

15. Harvey N, Dennison E, Cooper C. Osteoporosis: impact on health and economics. *Nat Rev Rheumatol*. 2010;6(2):99-105. doi:10.1038/nrrheum.2009.260

16. Paschalis EP, Fratzl P, Gamsjaeger S, et al. Aging vs Postmenopausal Osteoporosis: Bone Composition and Maturation Kinetics at Actively Forming Trabecular Surfaces of Female Subjects Aged 1 to 84 Years Old. *J Bone Miner Res*. August 2015. doi:10.1002/jbmr.2696

17. Eastell R, O'Neill TW, Hofbauer LC, et al. Postmenopausal osteoporosis. *Nat Rev Dis Prim*. 2016;2:16069. doi:10.1038/nrdp.2016.69

18. Johnell O, Kanis J. Epidemiology of osteoporotic fractures. *Osteoporos Int*. 2005;16 Suppl 2:S3-7. doi:10.1007/s00198-004-1702-6

19. Clarke BL, Khosla S. Female reproductive system and bone. *Arch Biochem Biophys*. 2010;503(1):118-128. doi:10.1016/J.ABB.2010.07.006

20. Reid IR. Decade in review-bone: Great strides made but still further to go. *Nat Rev Endocrinol*. 2015;11(11):633-634. doi:10.1038/nrendo.2015.143

21. Lescale C, Schenten V, Djeghloul D, et al. Hind limb unloading, a model of spaceflight conditions,

leads to decreased B lymphopoiesis similar to aging. *FASEB J*. 2015;29(2):455-463. doi:10.1096/fj.14-259770

22. Compston∗ J. Diagnosis of osteoporosis: Diagnostic work-up and secondary causes of osteoporosis. *Bone*. 2012;50. doi:10.1016/j.bone.2012.02.023

23. Gennari L, Merlotti D, Nuti R. Selective estrogen receptor modulator (SERM) for the treatment of osteoporosis in postmenopausal women: focus on lasofoxifene. *Clin Interv Aging*. 2010;5:19-29. http://www.ncbi.nlm.nih.gov/pubmed/20169039. Accessed September 24, 2018.

24. Narayanan P. Denosumab: A comprehensive review. *South Asian J cancer*. 2013;2(4):272-277. doi:10.4103/2278-330X.119895

25. Chapurlat RD. Odanacatib: a review of its potential in the management of osteoporosis in postmenopausal women. *Ther Adv Musculoskelet Dis*. 2015;7(3):103-109. doi:10.1177/1759720X15580903

26. Krege JH, Burge RT, Marin F. Teriparatide fracture effectiveness in the real world. *Osteoporos Int*. April 2015. doi:10.1007/s00198-015-3140-z

27. Saag KG, Petersen J, Brandi ML, et al. Romosozumab or Alendronate for Fracture Prevention in Women with Osteoporosis. *N Engl J Med*. 2017;377(15):1417-1427. doi:10.1056/NEJMoa1708322

28. Ferrari SL. Osteoporosis: Romosozumab to rebuild the foundations of bone strength. *Nat Rev Rheumatol*. 2018;14(3):128-128. doi:10.1038/nrrheum.2018.5

29. Jilka RL. The Relevance of Mouse Models for Investigating Age-Related Bone Loss in Humans. *Journals Gerontol Ser A Biol Sci Med Sci*. 2013;68(10):1209-1217. doi:10.1093/gerona/glt046

30. Aerssens J, Boonen S, Lowet G, Dequeker J. Interspecies Differences in Bone Composition, Density, and Quality: Potential Implications for *in Vivo* Bone Research [1]. *Endocrinology*. 1998;139(2):663-670. doi:10.1210/endo.139.2.5751

31. Kim J-N, Lee J-Y, Shin K-J, Gil Y-C, Koh K-S, Song W-C. Haversian system of compact bone and comparison between endosteal and periosteal sides using three-dimensional reconstruction in rat. *Anat Cell Biol*. 2015;48(4):258-261. doi:10.5115/acb.2015.48.4.258

32. Indo Y, Takeshita S, Ishii K-A, et al. Metabolic regulation of osteoclast differentiation and function. *J Bone Miner Res*. 2013;28(11):2392-2399. doi:10.1002/jbmr.1976

33. Rowe GC, Vialou V, Sato K, et al. Energy expenditure and bone formation share a common sensitivity to AP-1 transcription in the hypothalamus. *J Bone Miner Res*. 2012;27(8):1649-1658. doi:10.1002/jbmr.1618

34. Simon MM, Greenaway S, White JK, et al. A comparative phenotypic and genomic analysis of C57BL/6J and C57BL/6N mouse strains. *Genome Biol*. 2013;14(7):R82. doi:10.1186/gb-2013-14-7-r82

35. Sabsovich I, Clark JD, Liao G, et al. Bone microstructure and its associated genetic variability in 12 inbred mouse strains: microCT study and in silico genome scan. *Bone*. 2008;42(2):439-451. doi:10.1016/j.bone.2007.09.041

36. Clark D, Nakamura M, Miclau T, Marcucio R. Effects of Aging on Fracture Healing. *Curr Osteoporos Rep*. 2017;15(6):601-608. doi:10.1007/s11914-017-0413-9

37. Einhorn TA, Gerstenfeld LC. Fracture healing: mechanisms and interventions. *Nat Rev Rheumatol*. 2015;11(1):45-54. doi:10.1038/nrrheum.2014.164

38. Langdahl B, Ferrari S, Dempster DW. Bone modeling and remodeling: potential as therapeutic targets for the treatment of osteoporosis. *Ther Adv Musculoskelet Dis*. 2016;8(6):225-235. doi:10.1177/1759720X16670154

39. Kobayashi T, Kronenberg HM. Overview of skeletal development. *Methods Mol Biol*. 2014;1130:3-12. doi:10.1007/978-1-62703-989-5_1

40. Chen G, Chen L, Wen J, et al. Association between sleep duration, daytime nap duration and

osteoporosis varies by sex, menopause and sleep quality. *J Clin Endocrinol Metab*. May 2014:jc20133629. doi:10.1210/jc.2013-3629

41. Sims NA, Martin TJ. Coupling Signals between the Osteoclast and Osteoblast: How are Messages Transmitted between These Temporary Visitors to the Bone Surface? *Front Endocrinol (Lausanne)*. 2015;6:41. doi:10.3389/fendo.2015.00041

42. Feng J, Mantesso A, Sharpe PT. Perivascular cells as mesenchymal stem cells. *Expert Opin Biol Ther*. 2010;10(10):1441-1451. doi:10.1517/14712598.2010.517191

43. Schroeder TM, Jensen ED, Westendorf JJ. Runx2: A Master Organizer of Gene Transcription in Developing and Maturing Osteoblasts. 2005. doi:10.1002/bdrc.20043

44. Tang W, Li Y, Osimiri L, Zhang C. Osteoblast-specific Transcription Factor Osterix (Osx) Is an Upstream Regulator of Satb2 during Bone Formation. *J Biol Chem*. 2011;286(38):32995-33002. doi:10.1074/jbc.M111.244236

45. Cao Y, Zhou Z, de Crombrugghe B, et al. Osterix, a Transcription Factor for Osteoblast Differentiation, Mediates Antitumor Activity in Murine Osteosarcoma. *Cancer Res*. 2005;65(4):1124-1128. doi:10.1158/0008-5472.CAN-04-2128

46. Ducy P, Desbois C, Boyce B, et al. Increased bone formation in osteocalcin-deficient mice. *Nature*. 1996;382(6590):448-452. doi:10.1038/382448a0

47. ten Dijke P, Krause C, de Gorter DJ, Löwik CW, van Bezooijen RL. Osteocyte-Derived Sclerostin Inhibits Bone Formation: Its Role in Bone Morphogenetic Protein and Wnt Signaling. *J Bone Jt Surgery-American Vol*. 2008;90(Suppl 1):31-35. doi:10.2106/JBJS.G.01183

48. Collette NM, Genetos DC, Economides AN, et al. Targeted deletion of Sost distal enhancer increases bone formation and bone mass. *Proc Natl Acad Sci U S A*. 2012;109(35):14092-14097. doi:10.1073/pnas.1207188109

49. Díaz-Flores L, Gutiérrez R, Madrid JF, et al. Pericytes. Morphofunction, interactions and pathology

in a quiescent and activated mesenchymal cell niche. *Histol Histopathol*. 2009;24(7):909-969. doi:10.14670/HH-24.909

50. Duchamp de Lageneste O, Julien A, Abou-Khalil R, et al. Periosteum contains skeletal stem cells with high bone regenerative potential controlled by Periostin. *Nat Commun*. 2018;9(1):773. doi:10.1038/s41467-018-03124-z

51. Jankowski RJ, Deasy BM, Huard J. Muscle-derived stem cells. *Gene Ther*. 2002;9(10):642-647. doi:10.1038/sj.gt.3301719

52. Usas A, Huard J. Muscle-derived stem cells for tissue engineering and regenerative therapy. *Biomaterials*. 2007;28(36):5401-5406. doi:10.1016/j.biomaterials.2007.09.008

53. Tsuji W, Rubin JP, Marra KG. Adipose-derived stem cells: Implications in tissue regeneration. *World J Stem Cells*. 2014;6(3):312-321. doi:10.4252/wjsc.v6.i3.312

54. Armulik A, Abramsson A, Betsholtz C. Endothelial/Pericyte Interactions. *Circ Res*. 2005;97(6):512-523. doi:10.1161/01.RES.0000182903.16652.d7

55. Méndez-Ferrer S, Michurina T V, Ferraro F, et al. Mesenchymal and haematopoietic stem cells form a unique bone marrow niche. *Nature*. 2010;466(7308):829-834. doi:10.1038/nature09262

56. Nakai A, Hayano Y, Furuta F, Noda M, Suzuki K. Control of lymphocyte egress from lymph nodes through β_2-adrenergic receptors. *J Exp Med*. 2014;211(13):2583-2598. doi:10.1084/jem.20141132

57. Katayama Y, Battista M, Kao W-M, et al. Signals from the Sympathetic Nervous System Regulate Hematopoietic Stem Cell Egress from Bone Marrow. *Cell*. 2006;124(2):407-421. doi:10.1016/j.cell.2005.10.041

58. Stocks BT, Thomas AB, Elizer SK, et al. Hematopoietic Stem Cell Mobilization Is Necessary but Not Sufficient for Tolerance in Islet Transplantation. *Diabetes*. 2017;66(1):127-133. doi:10.2337/db16-0444

59. Knothe Tate ML, Yu NYC, Jalilian I, Pereira AF, Knothe UR. Periosteum mechanobiology and mechanistic insights for regenerative medicine. *Bonekey Rep*. 2016;5. doi:10.1038/bonekey.2016.70

60. Sims NA, Vrahnas C. Regulation of cortical and trabecular bone mass by communication between osteoblasts, osteocytes and osteoclasts. *Arch Biochem Biophys*. 2014;561:22-28. doi:10.1016/j.abb.2014.05.015

61. Bonewald LF. The amazing osteocyte. *J Bone Miner Res*. 2011;26(2):229-238. doi:10.1002/jbmr.320

62. Xiao Z, Huang J, Cao L, Liang Y, Han X, Quarles LD. Osteocyte-specific deletion of Fgfr1 suppresses FGF23. *PLoS One*. 2014;9(8):e104154. doi:10.1371/journal.pone.0104154

63. Shimada T, Kakitani M, Yamazaki Y, et al. Targeted ablation of Fgf23 demonstrates an essential physiological role of FGF23 in phosphate and vitamin D metabolism. *J Clin Invest*. 2004;113(4):561-568. doi:10.1172/JCI19081

64. Wein MN, Kronenberg HM. Regulation of Bone Remodeling by Parathyroid Hormone. *Cold Spring Harb Perspect Med*. January 2018:a031237. doi:10.1101/cshperspect.a031237

65. McCauley LK, Martin TJ. Twenty-five years of PTHrP progress: from cancer hormone to multifunctional cytokine. *J Bone Miner Res*. 2012;27(6):1231-1239. doi:10.1002/jbmr.1617

66. Wysolmerski JJ. Osteocytes remove and replace perilacunar mineral during reproductive cycles. *Bone*. 2013;54(2):230-236. doi:10.1016/j.bone.2013.01.025

67. Doty SB. Morphological evidence of gap junctions between bone cells. *Calcif Tissue Int*. 1981;33(5):509-512. http://www.ncbi.nlm.nih.gov/pubmed/6797704. Accessed September 23, 2018.

68. Alford A., Jacobs C., Donahue H. Oscillating fluid flow regulates gap junction communication in osteocytic MLO-Y4 cells by an ERK1/2 MAP kinase-dependent mechanism☆. *Bone*.

2003;33(1):64-70. doi:10.1016/S8756-3282(03)00167-4

69. Xu H, Gu S, Riquelme MA, et al. Connexin 43 Channels Are Essential for Normal Bone Structure and Osteocyte Viability. *J Bone Miner Res*. 2015;30(3):436-448. doi:10.1002/jbmr.2374

70. Civitelli R. Cell-cell communication in the osteoblast/osteocyte lineage. *Arch Biochem Biophys*. 2008;473(2):188-192. doi:10.1016/j.abb.2008.04.005

71. Shen H, Grimston S, Civitelli R, Thomopoulos S. Deletion of Connexin43 in Osteoblasts/Osteocytes Leads to Impaired Muscle Formation in Mice. *J Bone Miner Res*. 2015;30(4):596-605. doi:10.1002/jbmr.2389

72. Pi M, Chen L, Huang M-Z, et al. GPRC6A null mice exhibit osteopenia, feminization and metabolic syndrome. *PLoS One*. 2008;3(12):e3858. doi:10.1371/journal.pone.0003858

73. Shi Y, Shu Z-J, Wang H, et al. Altered Expression of Hepatic β-Adrenergic Receptors in Aging Rats: Implications for Age-Related Metabolic Dysfunction in Liver. *Am J Physiol Integr Comp Physiol*. December 2017:ajpregu.00372.2017. doi:10.1152/ajpregu.00372.2017

74. Hamrick MW. A role for myokines in muscle-bone interactions. *Exerc Sport Sci Rev*. 2011;39(1):43-47. doi:10.1097/JES.0b013e318201f601

75. Robertson D, Biaggioni I (Italo). *Primer on the Autonomic Nervous System*. Elsevier; 2012.

76. Brunton LL, Knollmann BC, Hilal-Dandan R. *Goodman & Gilman's the Pharmacological Basis of Therapeutics*. https://www.ncbi.nlm.nih.gov/nlmcatalog/101708739. Accessed September 24, 2018.

77. NAGATSU T, LEVITT M, UDENFRIEND S. TYROSINE HYDROXYLASE. THE INITIAL STEP IN NOREPINEPHRINE BIOSYNTHESIS. *J Biol Chem*. 1964;239:2910-2917. http://www.ncbi.nlm.nih.gov/pubmed/14216443. Accessed September 23, 2018.

78. Gether U, Andersen PH, Larsson OM, Schousboe A. Neurotransmitter transporters: molecular function of important drug targets. *Trends Pharmacol Sci*. 2006;27(7):375-383.

doi:10.1016/j.tips.2006.05.003

79. Roth M, Obaidat A, Hagenbuch B. OATPs, OATs and OCTs: the organic anion and cation transporters of the SLCO and SLC22A gene superfamilies. *Br J Pharmacol*. 2012;165(5):1260-1287. doi:10.1111/j.1476-5381.2011.01724.x

80. Koepsell H. Polyspecific organic cation transporters: their functions and interactions with drugs. *Trends Pharmacol Sci*. 2004;25(7):375-381. doi:10.1016/j.tips.2004.05.005

81. Torres GE, Gainetdinov RR, Caron MG. Plasma membrane monoamine transporters: structure, regulation and function. *Nat Rev Neurosci*. 2003;4(1):13-25. doi:10.1038/nrn1008

82. Bauman AL, Apparsundaram S, Ramamoorthy S, Wadzinski BE, Vaughan RA, Blakely RD. Cocaine and Antidepressant-Sensitive Biogenic Amine Transporters Exist in Regulated Complexes with Protein Phosphatase 2A. *J Neurosci*. 2000;20(20):7571-7578. http://www.jneurosci.org/content/20/20/7571.short. Accessed May 28, 2015.

83. Ma Y, Krueger JJ, Redmon SN, et al. Extracellular norepinephrine clearance by the norepinephrine transporter is required for skeletal homeostasis. *J Biol Chem*. 2013;288:30105-30113. doi:10.1074/jbc.M113.481309

84. Männistö PT, Kaakkola S. Catechol-O-methyltransferase (COMT): biochemistry, molecular biology, pharmacology, and clinical efficacy of the new selective COMT inhibitors. *Pharmacol Rev*. 1999;51(4):593-628. http://www.ncbi.nlm.nih.gov/pubmed/10581325. Accessed September 23, 2018.

85. Watkins P. COMT inhibitors and liver toxicity. *Neurology*. 2000;55(11 Suppl 4):S51-2; discussion S53-6. http://www.ncbi.nlm.nih.gov/pubmed/11147510. Accessed September 23, 2018.

86. Shih JC, Chen K, Ridd MJ. MONOAMINE OXIDASE: From Genes to Behavior. *Annu Rev Neurosci*. 1999;22(1):197-217. doi:10.1146/annurev.neuro.22.1.197

87. Al-Nuaimi SK, MacKenzie EM, Baker GB. Monoamine Oxidase Inhibitors and Neuroprotection. *Am*

J Ther. 2012;19(6):436-448. doi:10.1097/MJT.0b013e31825b9eb5

88. Elefteriou F, Ahn JD, Takeda S, et al. Leptin regulation of bone resorption by the sympathetic nervous system and CART. *Nature*. 2005;434(7032):514-520. doi:10.1038/nature03398

89. Kajimura D, Hinoi E, Ferron M, et al. Genetic determination of the cellular basis of the sympathetic regulation of bone mass accrual. *J Exp Med*. 2011;208(4):841-851. doi:10.1084/jem.20102608

90. Yamazaki K, Allen TD. Ultrastructural morphometric study of efferent nerve terminals on murine bone marrow stromal cells, and the recognition of a novel anatomical unit: The ?neuro-reticular complex? *Am J Anat*. 1990;187(3):261-276. doi:10.1002/aja.1001870306

91. Dénes Á, Boldogkoi Z, Uhereczky G, et al. Central autonomic control of the bone marrow: Multisynaptic tract tracing by recombinant pseudorabies virus. *Neuroscience*. 2005;134(3):947-963. doi:10.1016/j.neuroscience.2005.03.060

92. Chartier SR, Mitchell SAT, Majuta LA, Mantyh PW. The Changing Sensory and Sympathetic Innervation of the Young, Adult and Aging Mouse Femur. *Neuroscience*. February 2018. doi:10.1016/J.NEUROSCIENCE.2018.01.047

93. Chartier SR, Thompson ML, Longo G, Fealk MN, Majuta LA, Mantyh PW. Exuberant sprouting of sensory and sympathetic nerve fibers in nonhealed bone fractures and the generation and maintenance of chronic skeletal pain. *Pain*. 2014;155(11):2323-2336. doi:10.1016/j.pain.2014.08.026

94. Rosen CJ. Bone remodeling, energy metabolism, and the molecular clock. *Cell Metab*. 2008;7(1):7-10. doi:10.1016/j.cmet.2007.12.004

95. Fu L, Patel MS, Bradley A, Wagner EF, Karsenty G. The Molecular Clock Mediates Leptin-Regulated Bone Formation. *Cell*. 2005;122(5):803-815. doi:10.1016/j.cell.2005.06.028

96. Saxton SN, Ryding KE, Aldous RG, Withers SB, Ohanian J, Heagerty AM. Role of Sympathetic

Nerves and Adipocyte Catecholamine Uptake in the Vasorelaxant Function of Perivascular Adipose Tissue. *Arterioscler Thromb Vasc Biol*. 2018;38(4):880-891. doi:10.1161/ATVBAHA.118.310777

97. Fu L, Patel MS, Karsenty G. The circadian modulation of leptin-controlled bone formation. In: *Progress in Brain Research*. Vol 153. ; 2006:177-188. doi:10.1016/S0079-6123(06)53010-9

98. Maronde E, Schilling AF, Seitz S, et al. The Clock Genes Period 2 and Cryptochrome 2 Differentially Balance Bone Formation. Jin D-Y, ed. *PLoS One*. 2010;5(7):e11527. doi:10.1371/journal.pone.0011527

99. Kajimura D, Paone R, Mann JJ, Karsenty G. Foxo1 regulates Dbh expression and the activity of the sympathetic nervous system in vivo. *Mol Metab*. 2014;3(7):770-777. doi:10.1016/j.molmet.2014.07.006

100. Kelesidis T, Kelesidis I, Chou S, Mantzoros CS. Narrative review: the role of leptin in human physiology: emerging clinical applications. *Ann Intern Med*. 2010;152(2):93-100. doi:10.7326/0003-4819-152-2-201001190-00008

101. Ducy P, Amling M, Takeda S, et al. Leptin Inhibits Bone Formation through a Hypothalamic Relay: A Central Control of Bone Mass. *Cell*. 2000;100(2):197-207. doi:10.1016/S0092-8674(00)81558-5

102. Luan B, Goodarzi MO, Phillips NG, et al. Leptin-Mediated Increases in Catecholamine Signaling Reduce Adipose Tissue Inflammation via Activation of Macrophage HDAC4. *Cell Metab*. 2014;19(6):1058-1065. doi:10.1016/j.cmet.2014.03.024

103. Oury F, Yadav VK, Wang Y, et al. CREB mediates brain serotonin regulation of bone mass through its expression in ventromedial hypothalamic neurons. *Genes Dev*. 2010;24(20):2330-2342. doi:10.1101/gad.1977210

104. Ortuño MJ, Robinson ST, Subramanyam P, et al. Serotonin-reuptake inhibitors act centrally to cause bone loss in mice by counteracting a local anti-resorptive effect. *Nat Med*. September

2016. doi:10.1038/nm.4166

105. Hamrick M., Pennington C, Newton D, Xie D, Isales C. Leptin deficiency produces contrasting phenotypes in bones of the limb and spine. *Bone*. 2004;34(3):376-383. doi:10.1016/j.bone.2003.11.020

106. Motyl KJ, Rosen CJ. Understanding leptin-dependent regulation of skeletal homeostasis. *Biochimie*. 2012;94(10):2089-2096. doi:10.1016/j.biochi.2012.04.015

107. Seriwatanachai D, Thongchote K, Charoenphandhu N, et al. Prolactin directly enhances bone turnover by raising osteoblast-expressed receptor activator of nuclear factor κB ligand/osteoprotegerin ratio. *Bone*. 2008;42(3):535-546. doi:10.1016/j.bone.2007.11.008

108. Tamma R, Colaianni G, Zhu L, et al. Oxytocin is an anabolic bone hormone. *Proc Natl Acad Sci U S A*. 2009;106(17):7149-7154. doi:10.1073/pnas.0901890106

109. Elabd C, Basillais A, Beaupied H, et al. Oxytocin Controls Differentiation of Human Mesenchymal Stem Cells and Reverses Osteoporosis. *Stem Cells*. 2008;26(9):2399-2407. doi:10.1634/stemcells.2008-0127

110. Wei W, Motoike T, Krzeszinski JY, et al. Orexin Regulates Bone Remodeling via a Dominant Positive Central Action and a Subordinate Negative Peripheral Action. *Cell Metab*. 2014;19(6):927-940. doi:10.1016/j.cmet.2014.03.016

111. Bonnet N, Benhamou CL, Brunet-Imbault B, et al. Severe bone alterations under β2 agonist treatments: Bone mass, microarchitecture and strength analyses in female rats. *Bone*. 2005;37(5):622-633. doi:10.1016/j.bone.2005.07.012

112. Lipski S. Effects of beta-adrenergic stimulation on bone-marrow function in normal and sublethally irradiated mice. I. The effect of isoproterenol on cAMP content in bone-marrow cells in vivo and in vitro. *Int J Radiat Biol Relat Stud Phys Chem Med*. 1976;29(4):359-366. http://www.ncbi.nlm.nih.gov/pubmed/7535. Accessed September 24, 2018.

113. Bonnet N, Beaupied H, Vico L, et al. Combined Effects of Exercise and Propranolol on Bone Tissue in Ovariectomized Rats. *J Bone Miner Res*. 2007;22(4):578-588. doi:10.1359/jbmr.070117

114. Pierroz DD, Bouxsein ML, Rizzoli R, Ferrari SL. Combined treatment with a β-blocker and intermittent PTH improves bone mass and microarchitecture in ovariectomized mice. *Bone*. 2006;39(2):260-267. doi:10.1016/j.bone.2006.01.145

115. Swift JM, Swift SN, Allen MR, Bloomfield SA. Beta-1 Adrenergic Agonist Treatment Mitigates Negative Changes in Cancellous Bone Microarchitecture and Inhibits Osteocyte Apoptosis during Disuse. Marie PJ, ed. *PLoS One*. 2014;9(9):e106904. doi:10.1371/journal.pone.0106904

116. SWIFT JM, HOGAN HA, BLOOMFIELD SA. β-1 Adrenergic Agonist Mitigates Unloading-Induced Bone Loss by Maintaining Formation. *Med Sci Sport Exerc*. 2013;45(9):1665-1673. doi:10.1249/MSS.0b013e31828d39bc

117. Bouxsein ML, Devlin MJ, Glatt V, Dhillon H, Pierroz DD, Ferrari SL. Mice Lacking β-Adrenergic Receptors Have Increased Bone Mass but Are Not Protected from Deleterious Skeletal Effects of Ovariectomy. *Endocrinology*. 2009;150(1):144-152. doi:10.1210/en.2008-0843

118. Pierroz DD, Bonnet N, Bianchi EN, et al. Deletion of β-adrenergic receptor 1, 2, or both leads to different bone phenotypes and response to mechanical stimulation. *J Bone Miner Res*. 2012;27(6):1252-1262. doi:10.1002/jbmr.1594

119. Locatelli V, Bianchi VE. Effect of GH/IGF-1 on Bone Metabolism and Osteoporsosis. *Int J Endocrinol*. 2014;2014:1-25. doi:10.1155/2014/235060

120. Morey-Holton ER, Globus RK. Hindlimb unloading of growing rats: a model for predicting skeletal changes during space flight. *Bone*. 1998;22(5 Suppl):83S-88S. http://www.ncbi.nlm.nih.gov/pubmed/9600759. Accessed September 24, 2018.

121. Fonseca TL, Jorgetti V, Costa CC, et al. Double disruption of α2A- and α2C -adrenoceptors results in sympathetic hyperactivity and high-bone-mass phenotype. *J Bone Miner Res*. 2011;26(3):591-

603. doi:10.1002/jbmr.243

122. Cruz Grecco Teixeira MB, Martins GM, Miranda-Rodrigues M, et al. Lack of α2C-Adrenoceptor Results in Contrasting Phenotypes of Long Bones and Vertebra and Prevents the Thyrotoxicosis-Induced Osteopenia. *PLoS One*. 2016;11(1):e0146795. doi:10.1371/journal.pone.0146795

123. Almeida M, O'Brien CA. Basic Biology of Skeletal Aging: Role of Stress Response Pathways. *Journals Gerontol Ser A Biol Sci Med Sci*. 2013;68(10):1197-1208. doi:10.1093/gerona/glt079

124. Nojiri H, Saita Y, Morikawa D, et al. Cytoplasmic superoxide causes bone fragility owing to low-turnover osteoporosis and impaired collagen cross-linking. *J Bone Miner Res*. 2011;26(11):2682-2694. doi:10.1002/jbmr.489

125. Tiede-Lewis LM, Xie Y, Hulbert MA, et al. Degeneration of the osteocyte network in the C57BL/6 mouse model of aging. *Aging (Albany NY)*. 2017;9(10):2190-2208. doi:10.18632/aging.101308

126. Mulcrone PL, Campbell JP, Clément-Demange L, et al. Skeletal Colonization by Breast Cancer Cells Is Stimulated by an Osteoblast and β2AR-Dependent Neo-Angiogenic Switch. *J Bone Miner Res*. 2017;32(7):1442-1454. doi:10.1002/jbmr.3133

127. Werner RA, Chen X, Maya Y, et al. The Impact of Ageing on 11C-Hydroxyephedrine Uptake in the Rat Heart. *Sci Rep*. 2018;8(1):11120. doi:10.1038/s41598-018-29509-0

128. Iwase S, Mano T, Watanabe T, Saito M, Kobayashi F. Age-related changes of sympathetic outflow to muscles in humans. *J Gerontol*. 1991;46(1):M1-5. http://www.ncbi.nlm.nih.gov/pubmed/1986035. Accessed August 8, 2014.

129. Huang HH, Brennan TC, Muir MM, Mason RS. Functional a1-and b2-Adrenergic Receptors in Human Osteoblasts. *J Cell Physiol*. 2009;220:267-275. doi:10.1002/jcp.21761

130. Huang HH, Brennan TC, Muir MM, Mason RS. Functional alpha1- and beta2-adrenergic receptors in human osteoblasts. *J Cell Physiol*. 2009;220(1):267-275. doi:10.1002/jcp.21761

131. Tanaka K, Hirai T, Kodama D, Kondo H, Hamamura K, Togari A. α1B -adrenergic receptor signaling

regulates bone formation through the up-regulation of CCAAT/enhancer-binding protein delta expression in osteoblasts. *Br J Pharmacol*. January 2016. doi:10.1111/bph.13418

132. Deis S, Srivastava RK, Ruiz de Azua I, et al. Age-related regulation of bone formation by the sympathetic cannabinoid CB1 receptor. *Bone*. 2018;108:34-42. doi:10.1016/j.bone.2017.12.018

133. Toulis KA, Hemming K, Stergianos S, Nirantharakumar K, Bilezikian JP. β-adrenergic receptor antagonists and fracture risk: a meta-analysis of selectivity, gender, and site-specific effects. *Osteoporos Int*. 2014;25(1):121-129. doi:10.1007/s00198-013-2498-z

134. Zhang W, Kanehara M, Zhang Y, Wang X, Ishida T. Beta-blocker and other analogous treatments that affect bone mass and sympathetic nerve activity in ovariectomized rats. *Am J Chin Med*. 2007;35(1):89-101. doi:10.1142/S0192415X07004655

135. Graham S, Hammond-Jones D, Gamie Z, Polyzois I, Tsiridis E, Tsiridis E. The effect of β-blockers on bone metabolism as potential drugs under investigation for osteoporosis and fracture healing. *Expert Opin Investig Drugs*. 2008;17(9):1281-1299. doi:10.1517/13543784.17.9.1281

136. Baker JG. The selectivity of beta-adrenoceptor antagonists at the human beta1, beta2 and beta3 adrenoceptors. *Br J Pharmacol*. 2005;144(3):317-322. doi:10.1038/sj.bjp.0706048

137. Bonnet N, Benhamou CL, Malaval L, et al. Low dose beta-blocker prevents ovariectomy-induced bone loss in rats without affecting heart functions. *J Cell Physiol*. 2008;217(3):819-827. doi:10.1002/jcp.21564

138. Motohashi H, Inui K. Organic cation transporter OCTs (SLC22) and MATEs (SLC47) in the human kidney. *AAPS J*. 2013;15(2):581-588. doi:10.1208/s12248-013-9465-7

139. Haenisch B, Bilkei-Gorzo A, Caron MG, Bönisch H. Knockout of the norepinephrine transporter and pharmacologically diverse antidepressants prevent behavioral and brain neurotrophin alterations in two chronic stress models of depression. *J Neurochem*. 2009;111(2):403-416. doi:10.1111/j.1471-4159.2009.06345.x

140. Kellenberger S, Muller K, Richener H, Bilbe G. Formoterol and isoproterenol induce c-fos gene expression in osteoblast-like cells by activating beta2-adrenergic receptors. *Bone*. 1998;22(5):471-478. http://www.ncbi.nlm.nih.gov/pubmed/9600780. Accessed September 24, 2018.

141. Moore RE, Smith CK, Bailey CS, Voelkel EF, Tashjian AH. Characterization of beta-adrenergic receptors on rat and human osteoblast-like cells and demonstration that beta-receptor agonists can stimulate bone resorption in organ culture. *Bone Miner*. 1993;23(3):301-315. http://www.ncbi.nlm.nih.gov/pubmed/7908582. Accessed September 24, 2018.

142. Asada N, Katayama Y, Sato M, et al. Matrix-Embedded Osteocytes Regulate Mobilization of Hematopoietic Stem/Progenitor Cells. *Cell Stem Cell*. 2013;12(6):737-747. doi:10.1016/j.stem.2013.05.001

143. Elenkov IJ, Wilder RL, Chrousos GP, Vizi ES. The Sympathetic Nerve--An Integrative Interface between Two Supersystems: The Brain and the Immune System. *Pharmacol Rev*. 2000;52(4):595-638. http://pharmrev.aspetjournals.org/content/52/4/595.long. Accessed June 3, 2014.

144. Heidt T, Sager HB, Courties G, et al. Chronic variable stress activates hematopoietic stem cells. *Nat Med*. 2014;advance on. doi:10.1038/nm.3589

145. Ataka K, Asakawa A, Nagaishi K, et al. Bone marrow-derived microglia infiltrate into the paraventricular nucleus of chronic psychological stress-loaded mice. *PLoS One*. 2013;8(11):e81744. doi:10.1371/journal.pone.0081744

146. Mandela P, Ordway GA. The norepinephrine transporter and its regulation. *J Neurochem*. 2006;97(2):310-333. doi:10.1111/j.1471-4159.2006.03717.x

147. Farr JN, Charkoudian N, Barnes JN, et al. Relationship of Sympathetic Activity to Bone Microstructure, Turnover, and Plasma Osteopontin Levels in Women. *J Clin Endocrinol Metab*. 2012;97(11):4219-4227. doi:10.1210/jc.2012-2381

148. Tezini GCS V, Becari C, Zanotto CZ, Salgado MCO, Passaglia R de CAT, Souza HCD. Ageing is the main determinant of haemodynamics and autonomic cardiac changes observed in post-menopausal female rats. *Auton Neurosci*. 2013;174(1-2):36-41. doi:10.1016/j.autneu.2012.12.003

149. Veldhuis-Vlug a G, El Mahdiui M, Endert E, Heijboer a C, Fliers E, Bisschop PH. Bone Resorption Is Increased in Pheochromocytoma Patients and Normalizes following Adrenalectomy. *J Clin Endocrinol Metab*. 2012;97:E2093-7. doi:10.1210/jc.2012-2823

150. Yang S, Nguyen ND, Eisman JA, Nguyen T V. Association between beta-blockers and fracture risk: a Bayesian meta-analysis. *Bone*. 2012;51(5):969-974. doi:10.1016/j.bone.2012.07.013

151. Turker S, Karatosun V, Gunal I. Beta-blockers increase bone mineral density. *Clin Orthop Relat Res*. 2006;443:73-74. doi:10.1097/01.blo.0000200242.52802.6d

152. Rached M-T, Kode A, Xu L, et al. FoxO1 Is a Positive Regulator of Bone Formation by Favoring Protein Synthesis and Resistance to Oxidative Stress in Osteoblasts. *Cell Metab*. 2010;11(2):147-160. doi:10.1016/J.CMET.2010.01.001

153. Cherruau M, Facchinetti P, Baroukh B, Saffar JL. Chemical sympathectomy impairs bone resorption in rats: a role for the sympathetic system on bone metabolism. *Bone*. 1999;25(5):545-551. doi:10.1016/S8756-3282(99)00211-2

154. Holmberg K, Shi T-JS, Albers KM, Davis BM, Hökfelt T. Effect of Peripheral Nerve Lesion and Lumbar Sympathectomy on Peptide Regulation in Dorsal Root Ganglia in the NGF-Overexpressing Mouse. *Exp Neurol*. 2001;167(2):290-303. doi:10.1006/exnr.2000.7552

155. Hill EL, Turner R, Elde R. Effects of neonatal sympathectomy and capsaicin treatment on bone remodeling in rats. *Neuroscience*. 1991;44(3):747-755. doi:10.1016/0306-4522(91)90094-5

156. Sherman BE, Chole RA. Sympathectomy, Which Induces Membranous Bone Remodeling, Has No Effect on Endochondral Long Bone Remodeling In Vivo. *J Bone Miner Res*. 2000;15(7):1354-1360.

doi:10.1359/jbmr.2000.15.7.1354

157. Kajimura D, Lee HW, Riley KJ, et al. Adiponectin regulates bone mass via opposite central and peripheral mechanisms through FoxO1. *Cell Metab*. 2013;17(6):901-915. doi:10.1016/j.cmet.2013.04.009

158. Black PH. Stress and the inflammatory response: A review of neurogenic inflammation. *Brain Behav Immun*. 2002;16(6):622-653. doi:10.1016/S0889-1591(02)00021-1

159. Bjurholm A, Kreicbergs A, Terenius L, Goldstein M, Schultzberg M. Neuropeptide Y-, tyrosine hydroxylase- and vasoactive intestinal polypeptide-immunoreactive nerves in bone and surrounding tissues. *J Auton Nerv Syst*. 1988;25(2-3):119-125. http://www.ncbi.nlm.nih.gov/pubmed/2906951. Accessed November 25, 2014.

160. Niedermair T, Kuhn V, Doranehgard F, et al. Absence of substance P and the sympathetic nervous system impact on bone structure and chondrocyte differentiation in an adult model of endochondral ossification. *Matrix Biol*. 2014;38:22-35. doi:10.1016/j.matbio.2014.06.007

161. Baron R, Jänig W, Kollmann W. Sympathetic and afferent somata projecting in hindlimb nerves and the anatomical organization of the lumbar sympathetic nervous system of the rat. *J Comp Neurol*. 1988;275(3):460-468. doi:10.1002/cne.902750310

162. Mok S-A, Lund K, Campenot RB. A retrograde apoptotic signal originating in NGF-deprived distal axons of rat sympathetic neurons in compartmented cultures. *Cell Res*. 2009;19(5):546-560. doi:10.1038/cr.2009.11

163. Bataille C, Mauprivez C, Haÿ E, et al. Different sympathetic pathways control the metabolism of distinct bone envelopes. *Bone*. 2012;50(5):1162-1172. doi:10.1016/J.BONE.2012.01.023

164. HÉbert-Blouin M-N, Shane Tubbs R, Carmichael SW, Spinner RJ. Hilton's law revisited. *Clin Anat*. 2014;27(4):548-555. doi:10.1002/ca.22348

165. Kochi T, Imai Y, Takeda A, et al. Characterization of the arterial anatomy of the murine hindlimb:

functional role in the design and understanding of ischemia models. *PLoS One*. 2013;8(12):e84047. doi:10.1371/journal.pone.0084047

166. McCorry LK. Physiology of the autonomic nervous system. *Am J Pharm Educ*. 2007;71(4):78. http://www.ncbi.nlm.nih.gov/pubmed/17786266. Accessed September 24, 2018.

167. McCarthy I. The Physiology of Bone Blood Flow: A Review. *J Bone Jt Surg*. 2006;88(suppl_2):4. doi:10.2106/JBJS.F.00890

168. Xiao L, Kirabo A, Wu J, et al. Renal Denervation Prevents Immune Cell Activation and Renal Inflammation in Angiotensin II–Induced HypertensionNovelty and Significance. *Circ Res*. 2015;117(6):547-557. doi:10.1161/CIRCRESAHA.115.306010

169. Sakakura K, Ladich E, Cheng Q, et al. Anatomic Assessment of Sympathetic Peri-Arterial Renal Nerves in Man. *J Am Coll Cardiol*. 2014;64(7):635-643. doi:10.1016/j.jacc.2014.03.059

170. Maranon RO, Lima R, Mathbout M, et al. Postmenopausal hypertension: role of the sympathetic nervous system in an animal model. *Am J Physiol Regul Integr Comp Physiol*. 2014;306(4):R248-56. doi:10.1152/ajpregu.00490.2013

171. Hart ECJ, Charkoudian N. Sympathetic neural regulation of blood pressure: influences of sex and aging. *Physiology (Bethesda)*. 2014;29(1):8-15. doi:10.1152/physiol.00031.2013

172. Esler MD, Thompson JM, Kaye DM, et al. Effects of Aging on the Responsiveness of the Human Cardiac Sympathetic Nerves to Stressors. *Circulation*. 1995;91(2):351-358. doi:10.1161/01.CIR.91.2.351

173. HERTTING G, AXELROD J, PATRICK RW. Actions of cocaine and tyramine on the uptake and release of H3-norepinephrine in the heart. *Biochem Pharmacol*. 1961;8:246-248. http://www.ncbi.nlm.nih.gov/pubmed/13906918. Accessed August 8, 2014.

174. Schömig E, Fischer P, Schönfeld CL, Trendelenburg U. The extent of neuronal re-uptake of 3H-noradrenaline in isolated vasa deferentia and atria of the rat. *Naunyn Schmiedebergs Arch*

Pharmacol. 1989;340(5):502-508. http://www.ncbi.nlm.nih.gov/pubmed/2559332. Accessed May 3, 2018.

175. Galli A, DeFelice LJ, Duke BJ, Moore KR, Blakely RD. Sodium-dependent norepinephrine-induced currents in norepinephrine-transporter-transfected HEK-293 cells blocked by cocaine and antidepressants. *J Exp Biol*. 1995;198(Pt 10):2197-2212. http://www.ncbi.nlm.nih.gov/pubmed/7500004. Accessed May 3, 2018.

176. Wersinger C, Jeannotte A, Sidhu A. Attenuation of the norepinephrine transporter activity and trafficking via interactions with alpha-synuclein. *Eur J Neurosci*. 2006;24(11):3141-3152. doi:10.1111/j.1460-9568.2006.05181.x

177. AXELROD J, HERTTING G, POTTER L. Effect of Drugs on the Uptake and Release of 3H-Norepinephrine in the Rat Heart. *Nature*. 1962;194(4825):297-297. doi:10.1038/194297a0

178. Fan Y, Chen P, Li Y, et al. Corticosterone administration up-regulated expression of norepinephrine transporter and dopamine β-hydroxylase in rat locus coeruleus and its terminal regions. *J Neurochem*. 2014;128(3):445-458. doi:10.1111/jnc.12459

179. Mortensen O V., Larsen MB, Amara SG. MAP Kinase Phosphatase 3 (MKP3) Preserves Norepinephrine Transporter Activity by Modulating ERK1/2 Kinase-Mediated Gene Expression. *Front Cell Neurosci*. 2017;11:253. doi:10.3389/fncel.2017.00253

180. Khan AW, Ziemann M, Corcoran SJ, et al. NET silencing by let-7i in postural tachycardia syndrome. *JCI insight*. 2017;2(6):e90183. doi:10.1172/jci.insight.90183

181. Jin Y, Fan J, Li F, Bi L, Pei G. Local sympathetic denervation of femoral artery in a rabbit model by using 6-hydroxydopamine in situ. *Biomed Res Int*. 2014;2014:874947. doi:10.1155/2014/874947

182. Ma Y, Nyman JS, Tao H, Moss HH, Yang X, Elefteriou F. β2-Adrenergic receptor signaling in osteoblasts contributes to the catabolic effect of glucocorticoids on bone. *Endocrinology*. 2011;152(4):1412-1422. doi:10.1210/en.2010-0881

183. Grässel SG. The role of peripheral nerve fibers and their neurotransmitters in cartilage and bone physiology and pathophysiology. *Arthritis Res Ther*. 2014;16(6):485. doi:10.1186/s13075-014-0485-1

184. Epp JR, Niibori Y, Liz Hsiang H-L, et al. Optimization of CLARITY for Clearing Whole-Brain and Other Intact Organs. *eNeuro*. 2015;2(3). doi:10.1523/ENEURO.0022-15.2015

185. Chung K, Deisseroth K. CLARITY for mapping the nervous system. *Nat Methods*. 2013;10(6):508-513. doi:10.1038/nmeth.2481

186. Yang B, Treweek JB, Kulkarni RP, et al. Single-Cell Phenotyping within Transparent Intact Tissue through Whole-Body Clearing. *Cell*. 2014;158(4):945-958. doi:10.1016/j.cell.2014.07.017

187. Chung K, Wallace J, Kim S-Y, et al. Structural and molecular interrogation of intact biological systems. *Nature*. 2013;497(7449):332-337. doi:10.1038/nature12107

188. Ke M-T, Fujimoto S, Imai T. SeeDB: a simple and morphology-preserving optical clearing agent for neuronal circuit reconstruction. *Nat Neurosci*. 2013;16(8):1154-1161. doi:10.1038/nn.3447

189. Ertürk A, Becker K, Jährling N, et al. Three-dimensional imaging of solvent-cleared organs using 3DISCO. *Nat Protoc*. 2012;7(11):1983-1995. doi:10.1038/nprot.2012.119

190. Mach D., Rogers S., Sabino M., et al. Origins of skeletal pain: sensory and sympathetic innervation of the mouse femur. *Neuroscience*. 2002;113(1):155-166. doi:10.1016/S0306-4522(02)00165-3

191. Madisen L, Zwingman TA, Sunkin SM, et al. A robust and high-throughput Cre reporting and characterization system for the whole mouse brain. *Nat Neurosci*. 2010;13(1):133-140. doi:10.1038/nn.2467

192. Greenbaum A, Chan KY, Dobreva T, et al. Bone CLARITY: Clearing, imaging, and computational analysis of osteoprogenitors within intact bone marrow. *Sci Transl Med*. 2017;9(387). http://stm.sciencemag.org/content/9/387/eaah6518?utm_campaign=toc_stm_2017-04-26&et_rid=33807910&et_cid=1295134. Accessed April 26, 2017.

193. Piemontese M, Onal M, Xiong J, et al. Low bone mass and changes in the osteocyte network in mice lacking autophagy in the osteoblast lineage. *Sci Rep*. 2016;6(1):24262. doi:10.1038/srep24262

194. Yamashita A, Nishikawa S, Rancourt DE. Microenvironment Modulates Osteogenic Cell Lineage Commitment in Differentiated Embryonic Stem Cells. Aziz SA, ed. *PLoS One*. 2010;5(3):e9663. doi:10.1371/journal.pone.0009663

195. Cole SW, Nagaraja AS, Lutgendorf SK, Green PA, Sood AK. Sympathetic nervous system regulation of the tumour microenvironment. *Nat Rev Cancer*. 2015;15(9):563-572. doi:10.1038/nrc3978

196. Calvo W. The innervation of the bone marrow in laboratory animals. *Am J Anat*. 1968;123(2):315-328. doi:10.1002/aja.1001230206

197. García-Castellano JM, Díaz-Herrera P, Morcuende JA. Is bone a target-tissue for the nervous system? New advances on the understanding of their interactions. *Iowa Orthop J*. 2000;20:49-58. http://www.pubmedcentral.nih.gov/articlerender.fcgi?artid=1888751&tool=pmcentrez&rendertype=abstract. Accessed October 22, 2015.

198. Li J, Ahmad T, Spetea M, Ahmed M, Kreicbergs A. Bone reinnervation after fracture: a study in the rat. *J Bone Miner Res*. 2001;16(8):1505-1510. doi:10.1359/jbmr.2001.16.8.1505

199. Burt-Pichat B, Lafage-Proust MH, Duboeuf F, et al. Dramatic decrease of innervation density in bone after ovariectomy. *Endocrinology*. 2005;146(1):503-510. doi:10.1210/en.2004-0884

200. Zeng W, Pirzgalska RM, Pereira MMA, et al. Sympathetic neuro-adipose connections mediate leptin-driven lipolysis. *Cell*. 2015;163(1):84-94. doi:10.1016/j.cell.2015.08.055

201. Robling AG, Niziolek PJ, Baldridge LA, et al. Mechanical stimulation of bone in vivo reduces osteocyte expression of Sost/sclerostin. *J Biol Chem*. 2008;283(9):5866-5875. doi:10.1074/jbc.M705092200

202. Tomlinson RE, Li Z, Zhang Q, et al. NGF-TrkA Signaling by Sensory Nerves Coordinates the

Vascularization and Ossification of Developing Endochondral Bone. *Cell Rep*. 2016. doi:10.1016/j.celrep.2016.08.002

203. Hama H, Hioki H, Namiki K, et al. ScaleS: an optical clearing palette for biological imaging. *Nat Neurosci*. 2015;18(10):1518-1529. doi:10.1038/nn.4107

204. Lee E, Choi J, Jo Y, et al. ACT-PRESTO: Rapid and consistent tissue clearing and labeling method for 3-dimensional (3D) imaging. *Sci Rep*. 2016;6(1):18631. doi:10.1038/srep18631

205. Calve S, Ready A, Huppenbauer C, Main R, Neu CP. Optical clearing in dense connective tissues to visualize cellular connectivity in situ. *PLoS One*. 2015;10(1):e0116662. doi:10.1371/journal.pone.0116662

206. Optical Clearing and deep-tissue fluorescence imaging using fructose. http://repository.kulib.kyoto-u.ac.jp/dspace/bitstream/2433/188839/1/dseik00306.pdf. Accessed November 20, 2015.

207. Mai TH, Wu J, Diedrich A, Garland EM, Robertson D. Calcitonin gene-related peptide (CGRP) in autonomic cardiovascular regulation and vascular structure. *J Am Soc Hypertens*. 2014;8(5):286-296. doi:10.1016/j.jash.2014.03.001

208. Campbell JP, Karolak MR, Ma Y, et al. Stimulation of host bone marrow stromal cells by sympathetic nerves promotes breast cancer bone metastasis in mice. *PLoS Biol*. 2012;10(7):e1001363. doi:10.1371/journal.pbio.1001363

209. Rasmussen LE, Nedergaard OA. Effects of reboxetine on sympathetic neuroeffector transmission in rabbit carotid artery. *J Pharmacol Exp Ther*. 2003;306(3):995-1002. doi:10.1124/jpet.103.052233

210. Wong EHF, Sonders MS, Amara SG, et al. Reboxetine: a pharmacologically potent, selective, and specific norepinephrine reuptake inhibitor. *Biol Psychiatry*. 2000;47(9):818-829. doi:10.1016/S0006-3223(99)00291-7

211. Dostert P, Benedetti MS, Poggesi I. Review of the pharmacokinetics and metabolism of reboxetine, a selective noradrenaline reuptake inhibitor. *Eur Neuropsychopharmacol*. 1997;7 Suppl 1(1):S23-35; discussion S71-3. doi:10.1016/S0924-977X(97)00417-3